AFRL-PR-WP-TR-2000-2036

COMBUSTION STUDIES OF COAL DERIVED FUELS

DELIVERY ORDER 4

R.J. SANTORO

ENERGY INSTITUTE AND DEPARTMENT OF MECHANICAL AND NUCLEAR ENGINEERING
THE PENNSYLVANIA STATE UNIVERSITY
UNIVERSITY PARK, PA 16802-2320

FEBRUARY 2000

FINAL REPORT FOR 05-01-1998 – 03-31-2000

PROPULSION DIRECTORATE
AIR FORCE RESEARCH LABORATORY
AIR FORCE MATERIEL COMMAND
WRIGHT-PATTERSON AIR FORCE BASE OH 45433-7251

Form SF298 Citation Data

Report Date *("DD MON YYYY")* 01-02-2000	**Report Type** N/A	**Dates Covered (from... to)** *("DD MON YYYY")* 01-05-1998 31-03-2000

Title and Subtitle Combustion Studies of Coal Derived Fuels-Delivery Order 4	**Contract or Grant Number**
	Program Element Number
Authors Santoro, R. J.	**Project Number**
	Task Number
	Work Unit Number
Performing Organization Name(s) and Address(es) Energy Institute and Department of Mechanical and Nuclear Engineering The Pennsylvania State University University Park, PA 16802-2320	**Performing Organization Number(s)**
Sponsoring/Monitoring Agency Name(s) and Address(es) Propulsion Directorate Air Force Research Laboratory Air Force Materiel Command Wright-Patterson AFB, OH 45433-7251	**Monitoring Agency Acronym** AFRL/PRSF
	Monitoring Agency Report Number(s)

Distribution/Availability Statement
Approved for public release, distribution unlimited

Supplementary Notes

Abstract
Combustion studies were conducted to evaluate the suitability of using a coal-derived aviation fuel as a candidate JP-900 (i.e. a aviation fuel having maximum temperature capability of 482C (900F). Specific progress made for the four tasks constituting Delivery Order 4 is described here. These tasks are 1) combustion Studies of Coal-Based JP-900 at High Temperature and High Pressure Conditions, 2) Combustion Instability Studies Applicable to Coal-Based JP-900, 3) Pulse Detonation Engine Studies Using Coal-Based JP-900, and 4) Coal Derived Fuel Combustion Studies of an Advanced Gas Turbine Engine Fuel System.

Subject Terms
Fuel; Coal Derived Fuel; Thermal Stability; High Temperature Fuels; Combustion; Pulse Detontation Engine; Combustion Instability

Document Classification unclassified	**Classification of SF298** unclassified

Classification of Abstract unclassified	**Limitation of Abstract** unlimited
Number of Pages 94	

NOTICE

USING GOVERNMENT DRAWINGS, SPECIFICATIONS, OR OTHER DATE INCLUDED IN THIS DOCUMENT FOR ANY OTHER PURPOSE OTHER THAN GOVERNMENT PROCUREMENT DOES NOT IN ANY WAY OBLIGATE THE US GOVERNMENT. THE FACT THAT THE GOVERNMENT FORMULATED OR SUPPLIED DRAWINGS, SPECIFICATIONS, OR OTHER DATA DOES NOT LICENSE THE HOLDER OR ANY OTHER PERSON OR CORPORATION; OR CONVEY ANY RIGHTS OR PERMISSION TO MANUFACTURE, USE, OR SELL, ANY PATENTED INVENTION THAT MAY RELATE TO THEM.

THIS REPORT IS RELEASABLE TO THE NATIONAL TECHNICAL INFORMATION SERVICE (NTIS). AT NTIS, IT WILL BE AVAILABLE TO THE GENERAL PUBLIC, INCLUDING FOREIGN NATIONS.

THIS TECHNICAL REPORT HAS BEEN REVIEWED AND IS APPROVED FOR PUBLICATION.

C. Obringer

CYNTHIA OBRINGER
Fuels Branch
Propulsion Sciences and Advanced Concepts Division

William E. Harrison III

WILLIAM E. HARRISON III
Chief, Fuels Branch
Propulsion Sciences and Advanced Concepts Division

L. S. Harootyan

LEO S. HAROOTYAN
Deputy
Propulsion Sciences and Advanced Concepts Division

REPORT DOCUMENTATION PAGE

Form Approved
OMB No. 0704-0188

1. AGENCY USE ONLY *(Leave blank)*	2. REPORT DATE	3. REPORT TYPE AND DATES COVERED
	FEBRUARY 2000	FINAL REPORT FOR 05/01/1998 - 03/31/2000

4. TITLE AND SUBTITLE
COMBUSTION STUDIES OF COAL DERIVED FUELS -- DELIVERY ORDER 4

5. FUNDING NUMBERS
C F33615-98-D-2802
PE 62203
PR 3048
TA 05
WU EX

6. AUTHOR(S)
R.J. SANTORO

7. PERFORMING ORGANIZATION NAME(S) AND ADDRESS(ES)
Energy Institute and Department of Mechanical and Nuclear Engineering
The Pennsylvania State University
University Park, PA 16802-2320

8. PERFORMING ORGANIZATION REPORT NUMBER
D.O. 0004

9. SPONSORING/MONITORING AGENCY NAME(S) AND ADDRESS(ES)
PROPULSION DIRECTORATE
AIR FORCE RESEARCH LABORATORY
AIR FORCE MATERIEL COMMAND
WRIGHT-PATTERSON AFB, OH 45433-7251
POC: CINDY OBRINGER, AFRL/PRSF, 937-255-6390

10. SPONSORING/MONITORING AGENCY REPORT NUMBER
AFRL-PR-WP-TR-2000-2036

11. SUPPLEMENTARY NOTES

12a. DISTRIBUTION AVAILABILITY STATEMENT
APPROVED FOR PUBLIC RELEASE, DISTRIBUTION UNLIMITED.

12b. DISTRIBUTION CODE

13. ABSTRACT *(Maximum 200 words)*

Combustion studies were conducted to evaluate the suitability of using a coal-derived aviation fuel as a candidate JP-900 (i.e. a aviation fuel having maximum temperature capability of 482C (900F). Specific progress made for the four tasks constituting Delivery Order 4 is described here. These tasks are 1) Combustion Studies of Coal-Based JP-900 at High Temperature and High Pressure Conditions, 2) Combustion Instability Studies Applicable to Coal-Based JP-900, 3) Pulse Detonation Engine Studies Using Coal-Based JP-900, and 4) Coal Derived Fuel Combustion Studies of an Advanced Gas Turbine Engine Fuel System.

14. SUBJECT TERMS
Fuel, Coal Derived Fuel, Thermal Stability, High Temperature Fuels, Combustion, Pulse Detonation Engine, Combustion Instability.

15. NUMBER OF PAGES
94

16. PRICE CODE

17. SECURITY CLASSIFICATION OF REPORT	18. SECURITY CLASSIFICATION OF THIS PAGE	19. SECURITY CLASSIFICATION OF ABSTRACT	20. LIMITATION OF ABSTRACT
UNCLASSIFIED	UNCLASSIFIED	UNCLASSIFIED	SAR

EXECUTIVE SUMMARY

This report serves as the final report for the Combustion Studies of Coal-based Fuels, Air Force Contract No. F33615-98-D-2802 0004, Delivery Order 4, encompassing a performance period of May 1998 through August 1999. The purpose of Delivery Order 4 was to continue research work towards determining the suitability of coal-based aviation fuels as candidate JP-900 fuels [i.e., having maximum temperature capability of 482°C (900°F)]. The overall contract awarded to the Energy Institute at The Pennsylvania State University addresses the three main challenges of a coal-based JP-900: economic production, adequate thermal stability under advanced aircraft fuel system conditions, and effective combustion in advanced aircraft. The addition of fuel combustion studies was a new aspect, beginning with Delivery Order 4, to the pre-existing program. The progress made for Combustion Studies of Coal-based Fuels is reported here for the performance period noted above. Specific progress made for the four tasks constituting Delivery Order 4 is described here. These tasks are 1) Combustion Studies of Coal-Based JP-900 at High Temperature and High Pressure Conditions, 2) Combustion Instability Studies Applicable to Coal-Based JP-900, 3) Pulse Detonation Engine Studies Using Coal-Based JP-900, and 4) Coal Derived Fuel Combustion Studies of an Advanced Gas Turbine Engine Fuel System.

TABLE OF CONTENTS

I Introduction

This report serves as the final report for the Combustion Studies of Coal-based Fuels, Air Force Contract No. F33615-98-D-2802 0004, Delivery Order 4, encompassing a performance period of May 1998 through August 1999. The purpose of Delivery Order 4 was to continue to work toward the determination of the suitability of coal-based aviation fuels as candidate JP-900 fuels [i.e., having maximum temperature capability of 482°C (900°F)]. The overall contract awarded to the Energy Institute at The Pennsylvania State University addresses the three main challenges of a coal-based JP-900: economic production, adequate thermal stability under advanced aircraft fuel system conditions, and effective combustion in advanced aircraft. The addition of fuel combustion studies was a new aspect, beginning with Delivery Order 4, to the pre-existing program. The following manuscript reports the progress of Combustion Studies of Coal-based Fuels for the performance period noted above.

Future Air Force technology needs demand that hydrocarbon fuels play dual roles of fuel and coolant over wide ranges of combustion-chamber conditions in terms of temperature and pressure as well as in terms of coolant heat-sink capacity. The operations aspects of using a versatile and multiple-use fuel must be achieved consistent with high combustion efficiency, excellent combustion stability, and acceptable emissions from both signature and environmental-impact perspectives. These characteristics must be maintained over the entire flight envelope and be consistent with the operability and reliability objectives of future aircraft systems. Realizing the production of a coal-based aviation fuel that has the required thermal stability without satisfying engine combustion requirements is a hollow achievement. Therefore, a concurrent combustion research effort, carefully coordinated with the fuel production and fuel stability tasks, was initiated.

This effort focuses on the combustion of the coal-based fuels and representative simulants. Ultimately, the baseline fuels to be studied will be those that demonstrate high thermal-stability characteristics as a result of the fuel stabilization part of the program. Also, comparisons will be made with current aviation fuels such as JP-8 as well as with simulants such as tetradecane (good model for petroleum-based aviation fuels) and decalin (good model for high thermal stability coal-based fuel).

Investigations of the key processes of injection, atomization, vaporization, and mixing are being conducted as part of the combustion studies effort to determine their effect on ignition, combustion efficiency and stability, lean-blow-out (LBO) limits, and emission characteristics. Consideration is also given to the combustion environment that future coal-based fuels will encounter. This includes consideration of advanced gas-turbine combustor concepts as well as novel engine technologies such as pulse-detonation engines (PDE). Improvements in the performance of advanced gas-turbine engines and PDEs require a high heat sink, thermally stable fuel that can be used to cool hot engine components. Thus, combustion studies carried out under this task are comparing and contrasting thermally stressed fuels with unstressed fuels. This aspect of the work draws on the techniques and results of the fuel stabilization studies.

At the conclusion of Delivery Order 4 in August 1999, the bulk of the combustion work has been in the preparation for combustion studies with coal-based fuels. Delivery Order 4 involved substantial facility development and experiments with first-order simulants such as gaseous fuels and liquid heptane. The progress made in Delivery Order 4 will be described here in four sections corresponding to the Combustion tasks of 1) Combustion Studies of Coal-Based JP-900 at High Temperature and High Pressure Conditions, 2) Combustion Instability Studies Applicable to Coal-Based JP-900, 3) Pulse Detonation Engine Studies Using Coal-Based JP-900, and 4) Coal Derived Fuel Combustion Studies of an Advanced Gas Turbine Engine Fuel System.

II Combustion Studies of Coal-based JP-900 at High Temperature and High Pressure Conditions (Task 1)

In order to satisfy future efficiency and performance goals of the Air Force, the gas turbine operating temperature and pressure regime must be increased. Operating pressures approaching 5 MPa (50 atm.) in an advanced gas turbine combustor are envisioned. However, several key engineering science problems must be resolved before higher operating pressure gas turbine engines can be developed. Since the fuel serves a dual role as coolant and fuel, it may be injected into the chamber under some conditions at supercritical temperatures. (Critical properties of JP-8 are approximately 400°C (750°F) and 2.2 to 3.3 MPa (22-33 atm.), depending on the exact formulation [1].) Furthermore, the possibility of either thermal or catalytic decomposition of the fuel at extreme conditions further complicates the physics because of the multi-species, multi-phase nature of the decomposed fuel. The increased heat load on the fuel is forcing the Air Force to seek development of a fuel capable of maintaining thermal stability to 482°C (900°F, i.e., JP-900).

Clearly, the functionality of the gas turbine combustor will be strongly impacted by the fuel injection process in terms of performance, emission characteristics, stability and operability over extreme variations in fuel mass flowrate, temperature and pressure conditions, fuel composition and phase. The utilization of coal-based JP-900 will require that suitable performance and operability characteristics be achieved. The most challenging aspects faced in developing advanced gas turbine engines arise because the injector must operate in the four thermodynamic regimes depicted in Fig. 2.1. The injector needs to function with high performance, reasonable pressure drop margins, and acceptable emission characteristics and stability margins for all four flow scenarios encompassing fuel properties ranging from a high density liquid to low density, multi-species, multi-phase decomposed fuel products at a

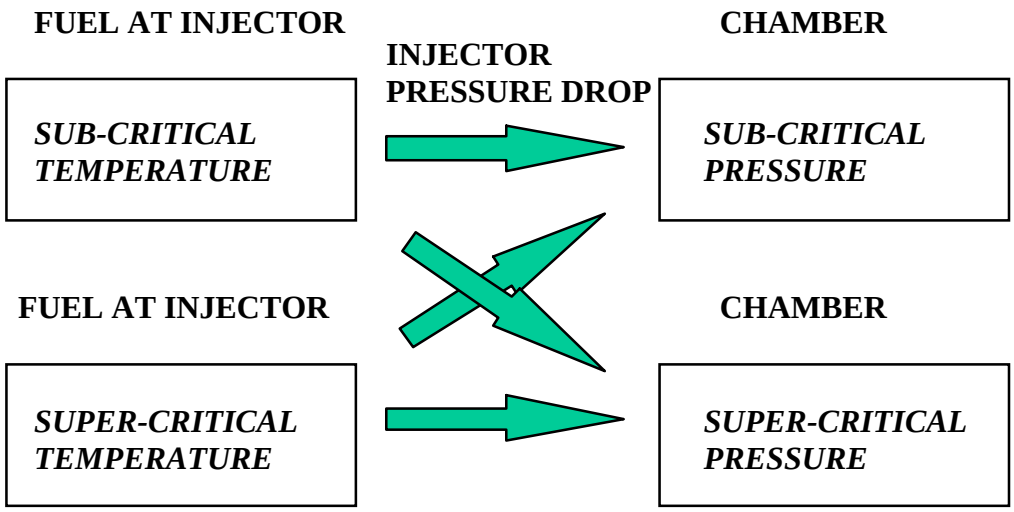

Fig. 2.1. Flow conditions for fuel injection into chamber. The four unique regimes differ widely in terms of fuel properties. Decomposition of fuel will further complicate physics. Injector design requires functionality over density variations of about 20.

supercritical temperature. Thus, atomization, ignition, and flame holding are critical processes for combustors operating on coal-based JP-900 if such fuels are to be effectively utilized.

2.1 Objectives and Approach

For this task, an integrated comprehensive experimental effort that investigates the key processes of injection, atomization, vaporization and mixing for coal-based JP-900 and more conventional fuels has been initiated. The experiments have been geared towards characterizing the fundamental injection behavior of JP-900 and simpler hydrocarbon fuels and simulants over the range of conditions including sub- to supercritical fuel pressures and temperatures as illustrated in Fig. 2.1. The investigations focus mainly on characterizing prototype coal-based JP-900 fuel, although as a basis for comparison and understanding, experiments with other fuels such as JP-8 (and derivatives) and simple hydrocarbon fuels such as *n*-heptane, tetradecane and decalin are included. At the conclusion of Delivery Order 4, injection experiments with *n*-heptane have been conducted. As an intermediate step between pure hydrocarbon fuels and

JP-900, experiments will be conducted in the follow-on program with mixtures of tetradecane and compounds such as tetralin to understand the effect of representative fuel additives relevant to JP-900. Studies of a light cycle oil/tetralin blend, which has shown high thermal stability, will also be investigated in the future as a prototypical coal-based fuel.

The high-pressure, high-temperature experiment focuses on the characterization of fuel injection behavior of small scale single jets (approximately 1 mm injector diameter) over a broad range of thermodynamic conditions and at jet Reynolds numbers from about 500 to 5000, covering both the laminar and turbulent regimes. Shadowgraph (and eventually laser sheet) imaging diagnostics are incorporated to determine the nature of fuel jet disintegration, also providing insight into the vaporization and mixing processes. Characterization will ultimately include quantitative and qualitative evaluation of related phenomena such as (1) liquid jet breakup versus viscous gas-like jet breakup, i.e., the influence of surface tension on jet disintegration, which is of particular interest with respect to the thermodynamic state of the fuel and fuel/air mixture; (2) jet spreading rate; and (3) size and range of characteristic length scales in the fuel/air shear layer. The experiments will attempt to define operational boundaries of coal-derived JP-900 based on different regimes of jet breakup, vaporization, and mixing as a function of pressure, temperature, and fuel composition (including multi-phase effects) that result from varying degrees of fuel stressing.

2.2 High-Pressure/High-Temperature Facility

The high-pressure/high-temperature experimental facility consists of (1) an instrumented, high-temperature, stressed fuel delivery rig, (2) a windowed chamber for visualization of phenomena resulting from fuel injection into gaseous nitrogen, (3) a low pressure fuel collection

and vent system, (4) a remotely operated electronic control system, and (5) an automatic safety circuit. These experimental apparati have been developed under Delivery Order 4.

The fuel delivery system is a flow reactor design similar to those used for investigating fuel thermal stability under that thrust of the overall coal-based JP-900 program. Its purpose is to expose the fuel to high-pressure and high-temperature conditions prior to injection. This process is referred to as "stressing" the fuel. By this means, the effect on injection and atomization behavior is investigated for varying degrees of fuel stressing. Also, characterization of the fuel decomposition products and deposits are accomplished in conjunction with injection experiments.

The main components of the fuel delivery system are a HPLC pump, furnace, chiller, and heat exchanger. A photograph of the fuel delivery system is shown in Fig. 2.2. The fuel is first pumped from a source bottle and then through coils in the furnace. The heated fuel exiting from the furnace can either be injected into the chamber if desired, or it can be cooled through the heat exchanger connected to the chiller and then injected into the chamber at a reduced temperature.

Fig. 2.2. Fuel Delivery System

Thus, the pre-stressed fuel can be injected either through a high-temperature or a low temperature route.

The fuel stressing system is capable of fuel delivery rates of 0–150 mL/min at constant fuel temperatures up to 538°C (1000°F). Automated feedback controls in the pump allow for fuel delivery at a constant flow rate. This apparatus is portable so that precisely stressed fuel of known composition can be supplied on-site to either the high-pressure inert injector or the model gas turbine combustor for combustion performance and stability experiments.

The high-pressure, high-temperature optically accessible injection chamber is designed for a maximum working pressure of 6.89 MPa (1,000 psia) at a 482°C (900°F) ambient steady state temperature. The chamber is water cooled so that high-temperature steady state operation is possible while ensuring seal integrity and maintaining exterior surface temperatures at a manageable level for safety reasons. The vessel is constructed of modular components, one of which is a windowed section, so that the chamber can be rearranged to change the window location with respect to the injector. The windowed section employs a 51 mm (2 in.) diameter, 25 mm (1 in.) thick quartz window on each of the four sides to provide sufficient optical access for imaging and laser diagnostics. An external gaseous nitrogen heat exchanger as well as an internal chamber electrical heating system has been developed to maintain the ambient nitrogen at a constant operating temperature.

The injection chamber assembly is shown in Fig. 2.3 as an assembly drawing and in a photograph in Fig. 2.4. The chamber assembly is comprised of five main structural pieces made from 304 stainless steel. These include the top and bottom plates, a main body consisting of two sections (the windowed section and a similar size blank section), and a water manifold between the two main body sections. The internal cross section of the pressure vessel is a 51 mm (2 in.)

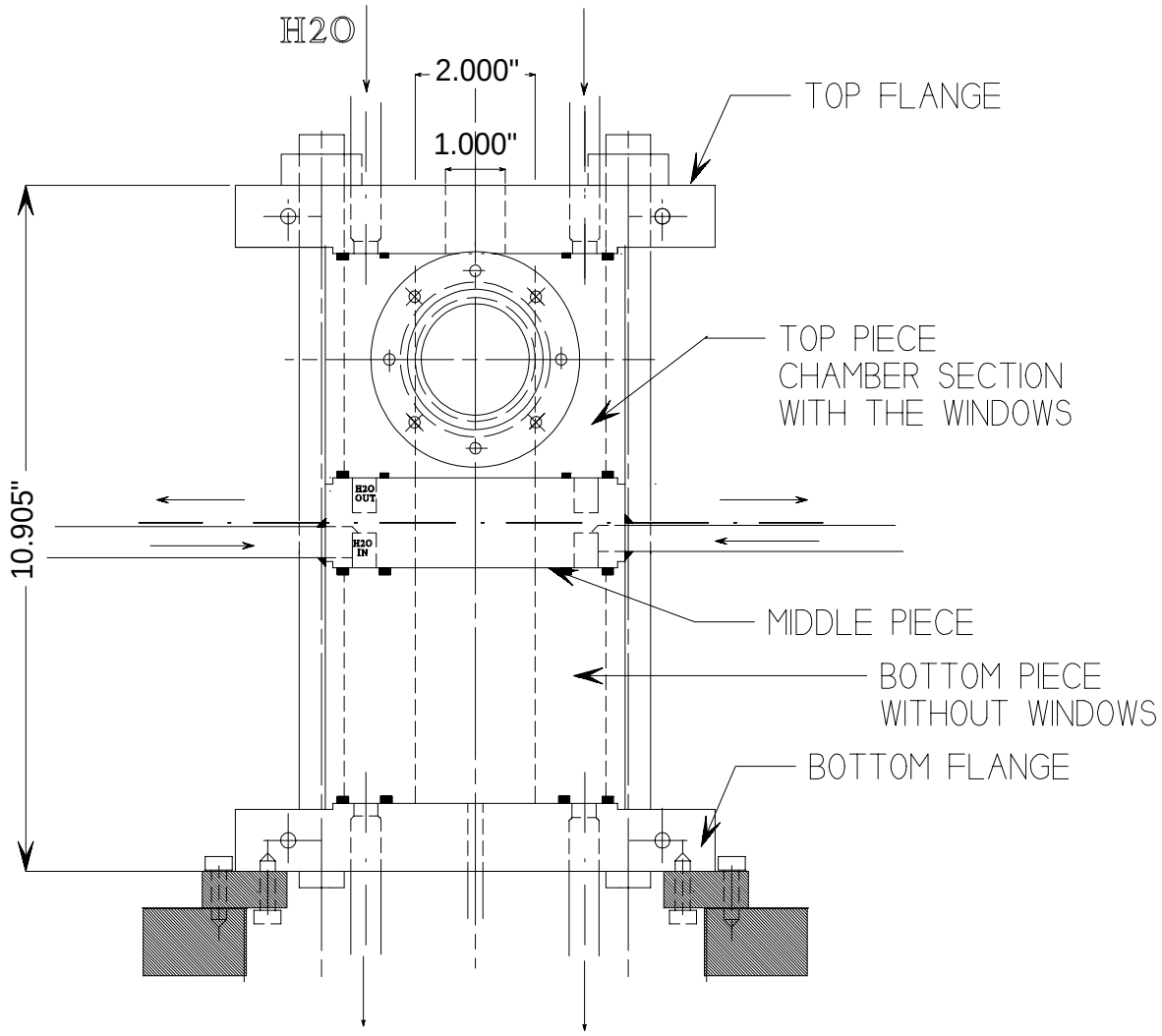

Fig. 2.3. High-pressure/high-temperature injection chamber assembly.

square with a 6.4 mm (1/4 in.) radius at each corner. An effort was made to keep the chamber as compact as possible to minimize heating requirements.

The fuel injector assembly is designed to study small scale, simple round jets issuing from a long L/D cylindrical tube injector. The injector is not necessarily representative of a comparatively complex gas turbine fuel injector, but it offers a simple geometry with which to study these complex physical phenomena and one for which the bulk of jet breakup and atomization studies have been conducted. The injection system is comprised of the injector

Fig. 2.4. Photograph of high-pressure/high-temperature injection chamber.

body, a height adjusting nut and flange, the injector tube, and a faceplate. The injector body is threaded at the upper end to allow 19 mm (0.75 in.) of injector height adjustment by simply turning the captured adjusting nut. In this manner, the position of the injector exit can be altered with respect to the window location without having to unseal or take apart the chamber. The injector faceplate is used to minimize recirculation zones around the injector tube. One faceplate fills the entire chamber cross section (51 mm square), while an alternative one fills the cross section (32 mm square) of a smaller internal chamber. The injector assembly is depicted in Fig. 2.5.

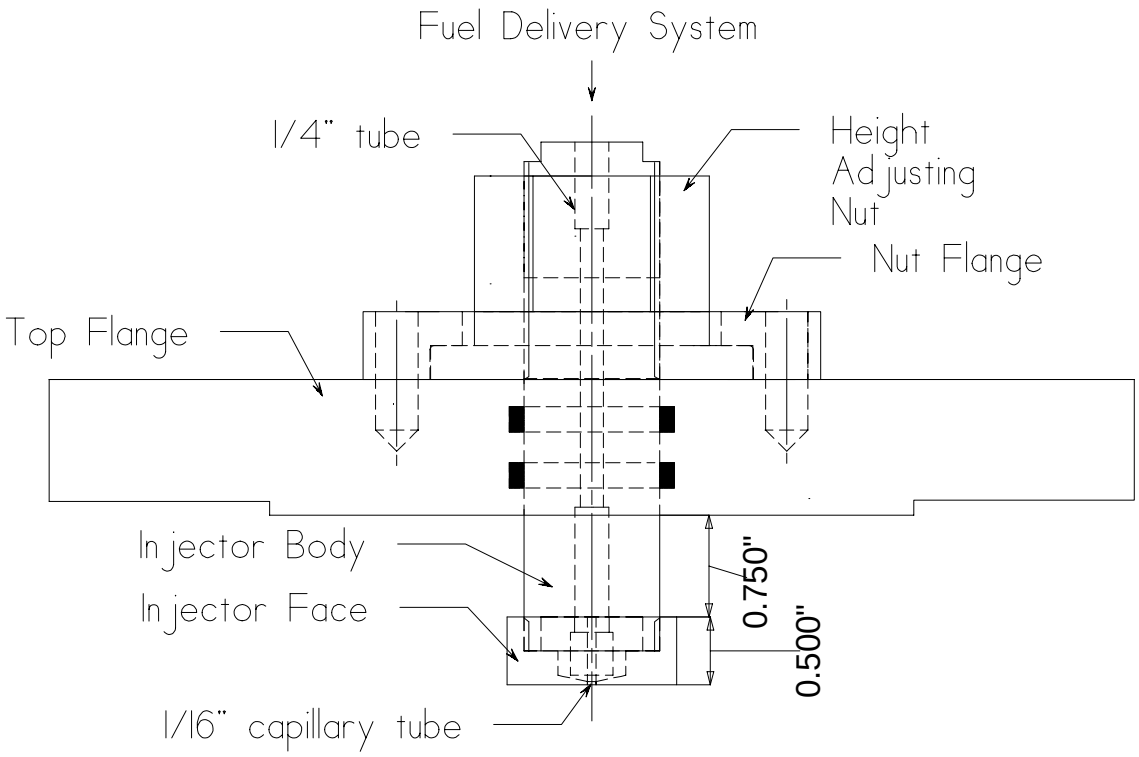

Fig. 2.5. Injector assembly.

Another important feature of the injection chamber is the internal non-structural heated cell. To minimize thermal losses to the stainless chamber and to provide a nearly isothermal wall for the injection region, an aluminum 32 mm (1.25 in.) (inside dimension) square tube was fabricated into a windowed internal chamber and fixed with cartridge heaters. The internal windows are simply made from 25 mm × 76 mm (1 in. × 3 in.) microscope slides since they do not contain pressure between the internal and structural chambers. Four 6.4 mm (1/4 in.) diameter × 140 mm (5.5 in.) long cartridge heaters, rated at 500 Watts each, pass through the bottom plate and attach to the aluminum chamber, one on each outer face, as shown in Fig. 2.6. Heated nitrogen from the external heater passes through tubes in the bottom plate and travels along the outer walls of the internal chamber. Holes near the top of the aluminum chamber allow the nitrogen to pass into the internal chamber and flow down along the injection axis at a

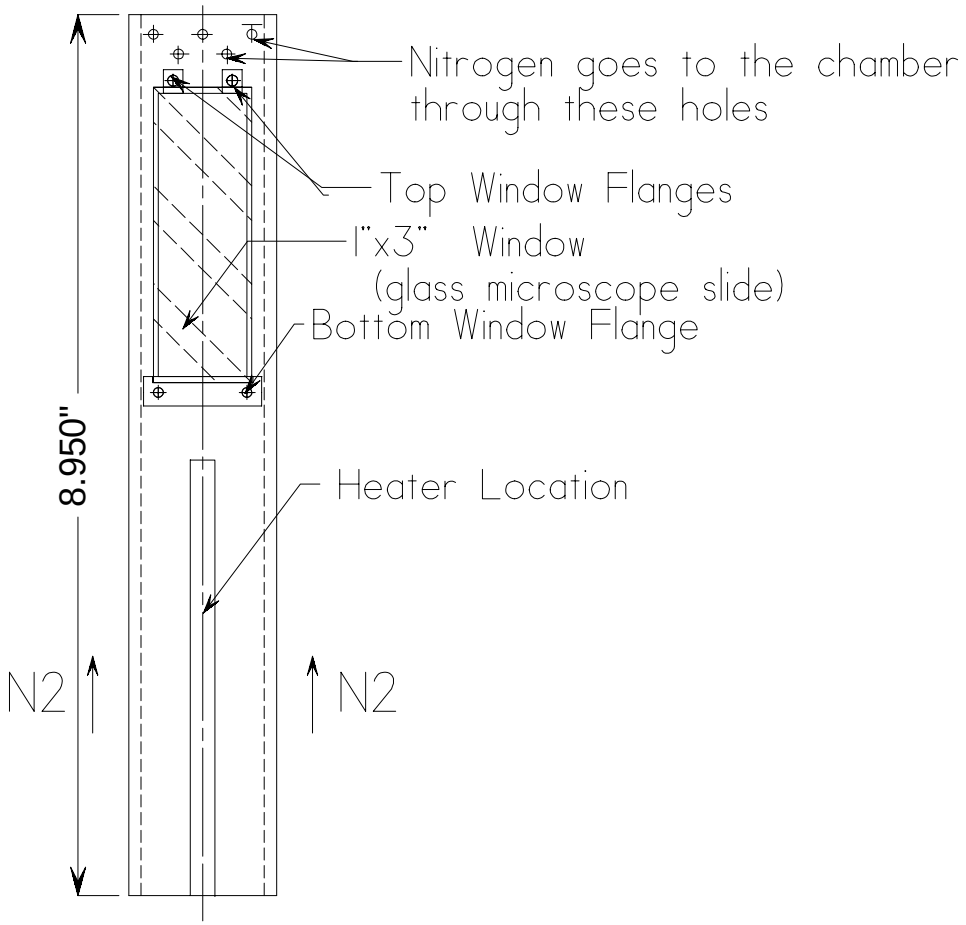

Fig 2.6. Heated internal chamber.

velocity of approximately 1-2 cm/s, approximately an order of magnitude lower than the fuel injection velocity. The intent is to refresh the heated nitrogen in the internal chamber while flushing fuel vapor through the vent in the bottom plate.

A water cooling system was implemented in the high-pressure/high-temperature injection chamber design to enhance safety and so that elastomer seals could be employed between the modular sections and for the windows. A water manifold is used between the window and blank main chamber sections so that there are two independent water cooling paths, one for the upper section and one for the lower section. This allows tailoring the water flowrate for each section.

The water cooling system creates a secondary barrier in case of a primary seal failure, preventing hot fuel from being released into the air where it has a potential to autoignite.

To maintain a constant pressure in the injection chamber, nitrogen and fuel is continually vented through a hole at the center of the bottom plate. A remotely controlled motorized metering valve is used on the vent line to adjust the exit flowrate and control the chamber pressure. The vent flow is directed into a fuel collection system. The collection system is comprised of a low pressure [1 MPa (130 psig) max.] tank, a heat exchanger, and a gas vent system. Water from the chiller in the fuel delivery system cools the collection tank and the incoming vent flow, condensing a majority of the fuel vapor. Thus, liquid fuel collects and is temporarily stored in this tank while nitrogen and any uncondensed fuel vapor is directed through a tube into the laboratory vent hood where it exits the building through the roof.

Fig. 2.7 is a photograph of the setup for the high-pressure/high-temperature fuel injection experiments. In this photograph, the fuel delivery system, injection chamber, water cooling lines, fuel collection system, and laboratory vent hood can be seen. Fig. 2.8 is a flow schematic diagram for the experiment.

As a safety precaution, the high-pressure/high-temperature experiment is controlled remotely from an adjacent room using a video monitoring system. A safety circuit which requires continuity in a 5V control circuit that includes a key switch, a mushroom kill switch, and a multi-channel temperature alarm in order for all heaters and fuel and nitrogen supplies to be operational. Thus in case of an emergency or pre-set over-temperature condition, all power can be manually or automatically removed from these devices, putting the experiment in a safe state. The electrical schematic including the safety circuit is shown in Fig. 2.9.

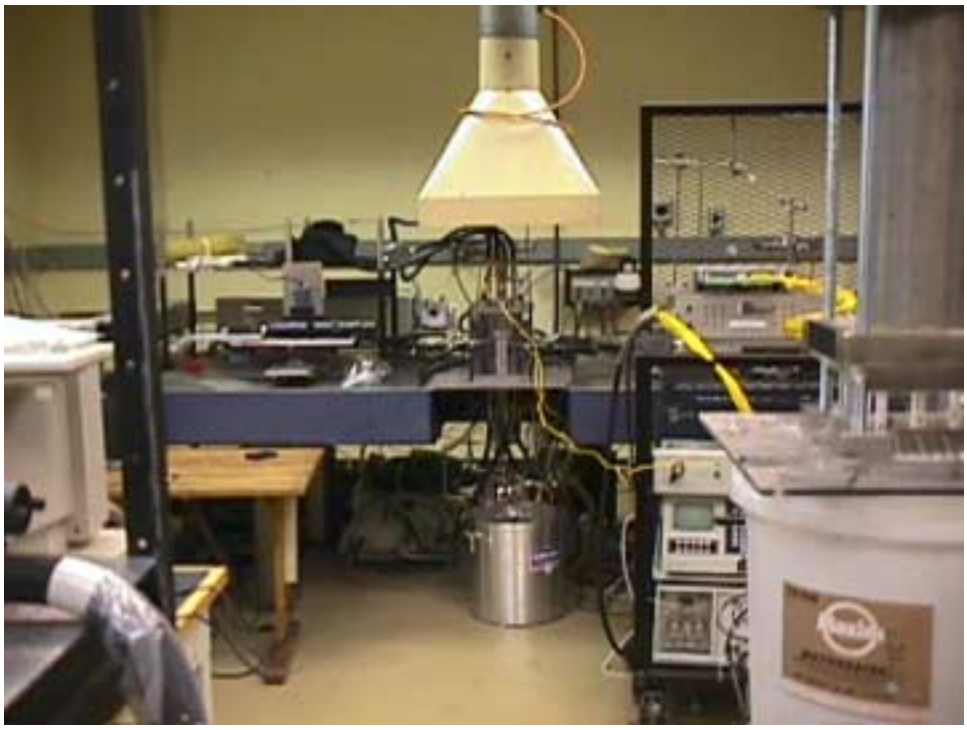

Fig. 2.7. Photograph of high-pressure/high-temperature fuel injection experimental setup.

2.3 Imaging Diagnostic

A shadowgraph imaging diagnostic technique has been and will continue to be utilized to determine fuel jet characteristics as a function of injection and ambient conditions. In this setup, a high resolution ($1024\text{H} \times 1024\text{V}$) monochrome progressive scan CCD camera (Pulnix TM-1010) is used to record the jet images. This camera has a dynamic range of 10 bits and outputs a digital signal. The camera is operated in the asynchronous reset mode to synchronize the electronically shuttered exposure with a short duration (1.2 μs) strobe flash. The video reset signal from the camera triggers a digital pulse delay generator which sends a precisely delayed signal to trigger the strobe lamp. The strobe is located at the opposite window of the chamber in line with the camera. A long distance microscope lens (Infinity Photo-Optical Model K2) is used with the camera to produce high resolution images of the small scale jets. The camera/lens assembly is mounted on a stepper motor actuated translation stage so that the imaging system

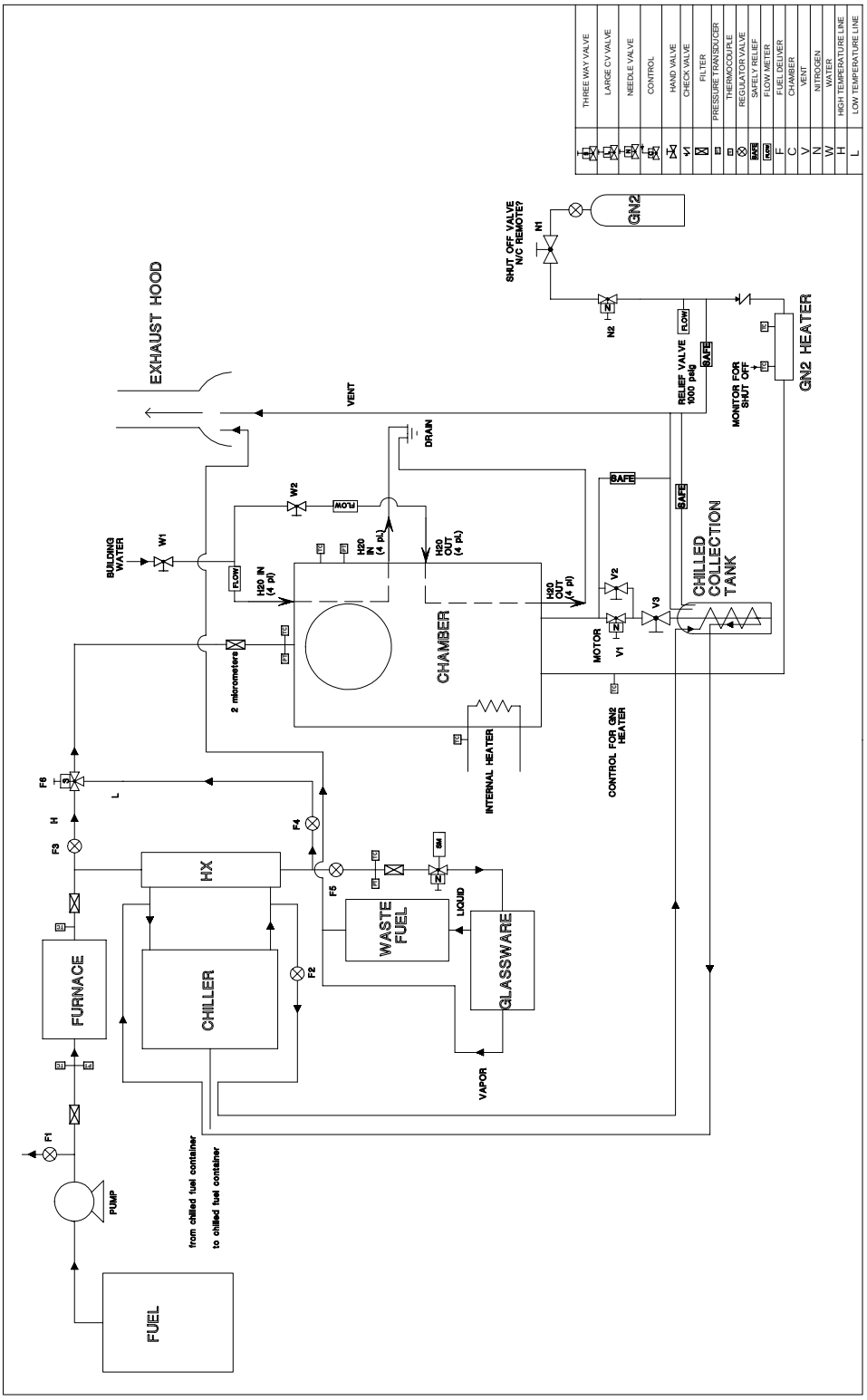

Fig. 2.8. Flow schematic of high-pressure/high-temperature fuel injection experiment.

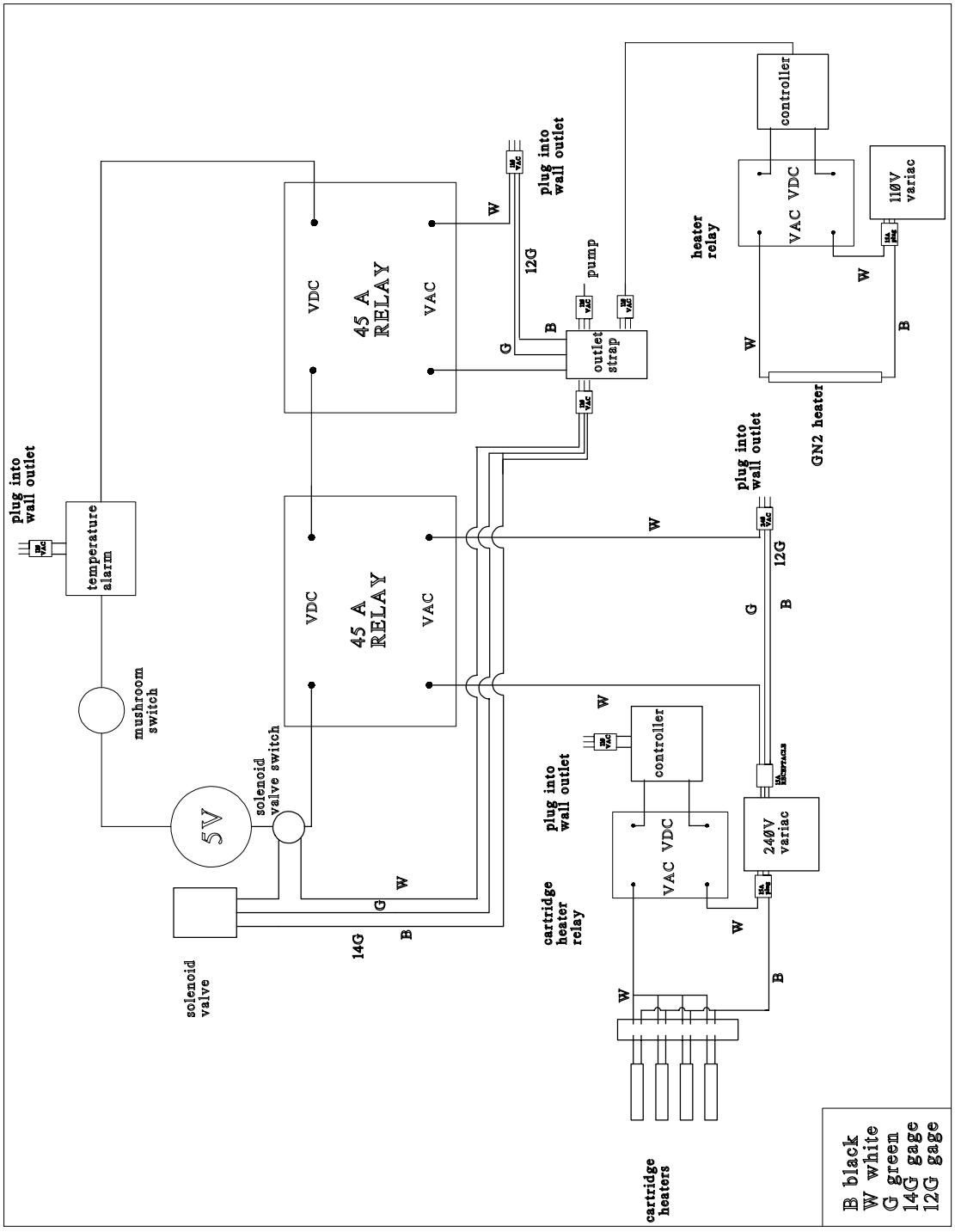

Fig. 2.9. Electrical schematic of high-pressure/high-temperature fuel injection experiment.

can be remotely re-positioned in the vertical and transverse (to adjust focus) directions. Image data from the camera is transferred to a National Instruments IMAQ-PCI-1424 digital frame grabber board installed in an AMD K6-233 Pentium-class computer. An NI-IMAQ Vision and LabVIEW software program is used to capture and store short multiple image sequences at a rate of about 2 Hz.

2.4 Results and Discussion

2.4.1 High-Pressure, Room-Temperature Results

The first model fuel tested was n-heptane (95% purity) because of its well known properties, single component simplicity, and accessible critical properties [T_{crit} = 267˚C (513 ˚F), P_{crit} = 2.74 MPa (27 atm, 397 psia)]. The first set of injection experiments with n-heptane into nitrogen was conducted at room temperature but using the full pressure range of the chamber from 1.83 MPa (250 psig) to 8.38 MPa (1200 psig). [Note the design working pressure of the chamber is 6.89 MPa (1,000 psia) at 482°C (900˚F) so that higher operating pressures are allowable at room temperature. The chamber was hydrostatically pressure tested to 12.5 MPa (1,800 psig).] The fuel was injected into the chamber at a flow rate of 20 ml/min. The jet issued through a capillary tube of 0.51 mm (0.020 in.) inner diameter at an average velocity of 1.6 m/sec. The data consists of shadowgraph images taken at different locations inside the chamber from the injector exit to 75 jet diameters downstream.

Fig. 2.10 shows a series of shadowgraph images of n-heptane jets at the injector exit at high-pressure [image (a) at 8.38 MPa (1200 psig)] down to low pressure [image (f) at 1.83 MPa (250 psig)]. For each of these images, the reduced pressure, chamber pressure/critical pressure

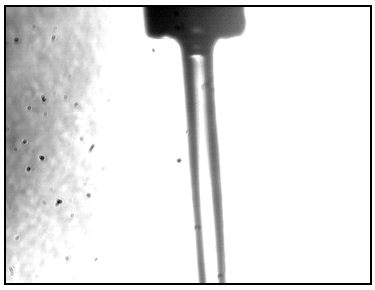

(a) P=1200 psig, P/Pcrit=3

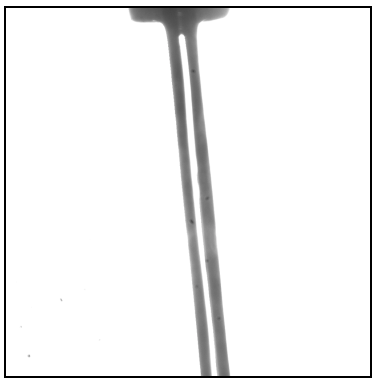

(b) P=975 psig, P/Pcrit=2.4

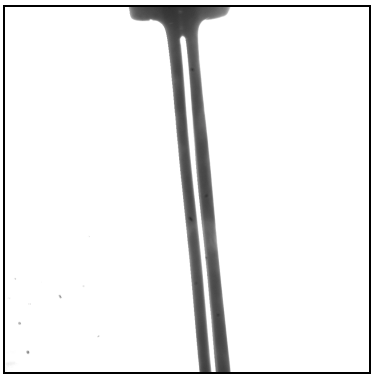

(c) P=800 psig, P/Pcrit=2

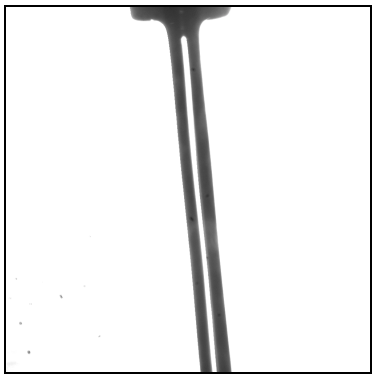

(d) P=600 psig, P/Pcrit=1.5

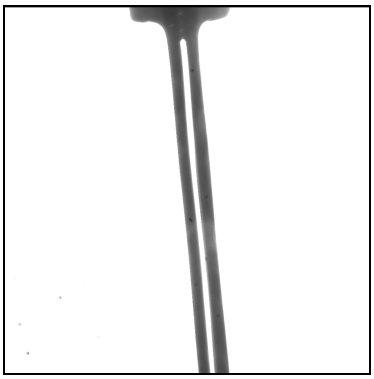

(e) P=400 psig, P/Pcrit=1

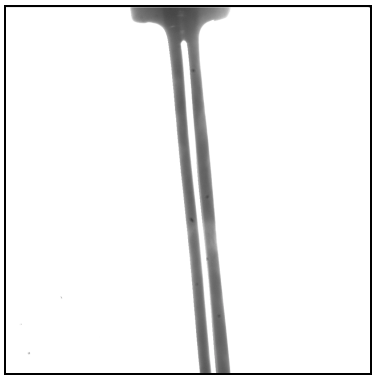

(f) P=250 psig, P/Pcrit=0.6

Fig. 2.10. Shadowgraph images of liquid n-heptane jets issuing into nitrogen at room temperature. Top of images corresponds to exit of the injector. Orifice diameter is 0.51 mm.

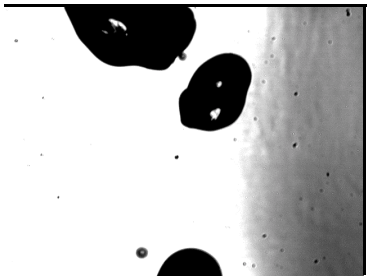

(a) P=1200 psig, P/Pcrit=3

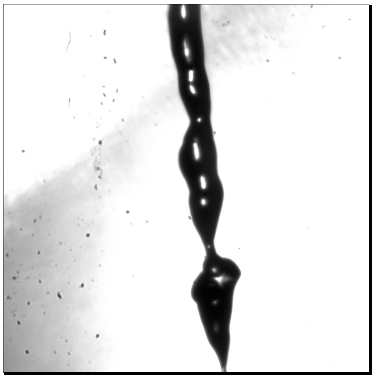

(b) P=975 psig, P/Pcrit=2.4

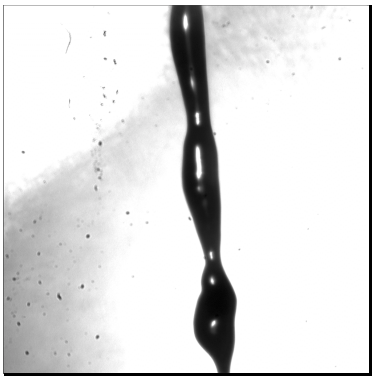

(c) P=800 psig, P/Pcrit=2

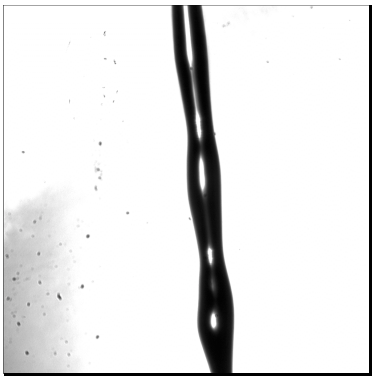

(d) P=600 psig, P/Pcrit=1.5

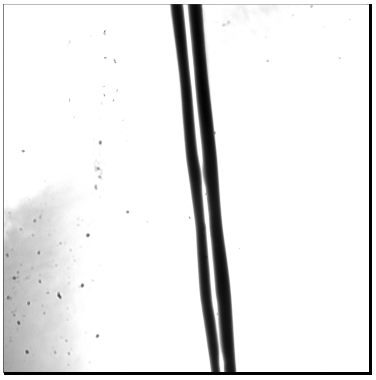

(e) P=400 psig, P/Pcrit=1

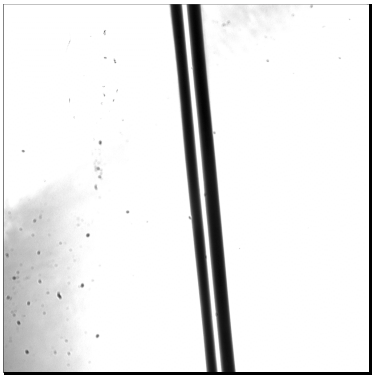

(f) P=250 psig, P/Pcrit=0.6

Fig. 2.11. Shadowgraph images of liquid n-heptane jets issuing into nitrogen at room temperature. Top of images corresponds to a location 75 diameters from exit of the injector.

(P/P_{crit}), is given with respect to pure n-heptane. The injection of the n-heptane into nitrogen produces a smooth laminar jet which does not exhibit any breakup or disturbances on the surface of the jet for many jet diameters downstream. As expected, distinct interfaces between gas (nitrogen) and liquid (n-heptane) phases exist for the whole range of pressures since the ambient temperature was subcritical for n-heptane. Since the primary breakup mechanism at these conditions is due to the interaction of surface tension and viscous forces (Rayleigh breakup) ambient pressure (at far-subcritical temperature) does not greatly affect the near injector region.

Similarly, Fig. 2.11 shows a series of n-heptane jet images for the same range of pressure but at a location 75 injector diameters farther downstream. At the lowest pressure, in the jet image (f), it is apparent that a smooth liquid column still exists at this location under these conditions. At 2.86 MPa (400 psig), image (e), capillary symmetric disturbances are just beginning to appear at this downstream location. With increasing pressure, the capillary disturbances become more unstable and less symmetric at the same location. In image (b) at 6.82 MPa (975 psig), an irregularly shaped droplet is about to be pinched off from the column. In image (a) at 8.38 MPa (1200 psig), the liquid jet is broken up at this location into a series of large non-spherical droplets. The jet breakup mode is still in the Rayleigh regime with respect to droplet production; however, it is obvious that increasing pressure advances the stage of jet breakup at the same axial distance. The pressure effect is more likely an aerodynamic effect through the gas density and consequent drag enhancement rather than by affecting the surface tension or liquid viscosity. Although there is a pressure effect, as expected at this far-subcritical temperature condition, there appears to be no significance with respect to jet breakup to the fact that the critical pressure was substantially exceeded [$P/P_{crit} = 3$ in image (a)].

2.4.2 High-Pressure, High-Temperature Results

Obviously more dramatic results with greater relevance to engine operating conditions are to be obtained at elevated temperatures. Such experiments were attempted under Delivery Order 4 with n-heptane into heated nitrogen. For these experiments, the external nitrogen heater and the chamber internal cartridge heaters were operated, initially with the desire to at least raise the ambient nitrogen temperature above the critical temperature of n-heptane. However, difficulty was encountered in maintaining high temperature operation. Internal chamber temperatures of about 315°C (600˚F) were achieved after extensive heating. This was a sufficient temperature to look at critical effects for n-heptane; however, these temperatures could be maintained only for short periods of time whereupon the internal cartridge heaters would invariably fail. Hence, no injection data at these conditions was obtained. The internal cartridge heaters were being overheated in order to raise the internal ambient temperature to that degree. In fact, the internal aluminum chamber to which the cartridge heaters were attached locally melted at the heater interface. The external nitrogen heater worked as intended, realizing nitrogen temperatures at the design goal of 482°C (900˚F) at the heater exit; however, it was discovered that by the time the heated nitrogen flow reached the inside of the chamber, the nitrogen was barely above room temperature. Thus, higher than anticipated heat losses to the short length of stainless tubing from the external heater to the chamber and especially to the stainless chamber itself completely negated the efficacy of the external nitrogen heater, requiring the internal cartridge heaters to be overdriven to realize any appreciable temperature rise in the internal chamber.

At the conclusion of Delivery Order 4, it was determined that it was necessary to redesign the heating system. This has been carried out as part of the following year's effort.

III Combustion Instability Studies Applicable to Coal-based JP-900 (Task 2)

The concept of lean-premixed combustion in gas turbine engine operation has become a standard in recent years as an effective means to meet stringent environmental standards on NO_x emissions [2]. However, the understanding and control of pressure oscillations in the combustor represents one of the most challenging and least understood phenomena potentially limiting the development of future high performance gas turbine engines. In the present work, experiments were performed to investigate combustion instability under high pressure and high temperature operating conditions for various air swirl conditions. These experiments, conducted with natural gas as the fuel, utilized an Annular Counter Rotating Swirl (DACRS) injector designed and fabricated by General Electric Aircraft Engines. The experimental results, detailed in this report for the DACRS injector, complement earlier work for a Penn State designed swirl injector [3,4] conducted under separate funding from the U.S. Department of Energy, Federal Energy Technology Center, through a cooperative agreement with the South Carolina Energy Research and Development Center at Clemson University. In addition to the combustion instability research involving the DACRS injector, the experimental definition for a trapped vortex combustor is also presented. In the area of analysis, complementary CFD analyses of the combustion instability phenomenon for the Penn State injector [3,4] are presented and discussed

In this section, experimental results obtained for the DACRS injector at elevated temperature and pressure operating conditions are presented first. This is followed by a discussion of the experiments to be conducted in the future for the trapped vortex combustor. Following this discussion, the numerical modeling results for gas turbine combustion are presented and discussed in lieu with the experimental results.

3.1 Experimental Investigations of Combustion Instability

3.1.1 DACRS Injector Combustion Instability Studies

The major objective of this study was to provide detailed measurements of the stability characteristics of an uni-element combustor under well-controlled conditions. Parameters known to affect combustion instability were systematically varied and included inlet air temperature, equivalence ratio, combustion chamber pressure, chamber length and swirl injector design. Corresponding stability maps were determined. In an attempt to learn more about the mechanism responsible for the sustenance of combustion instability, efforts also focused on correlating combustion heat release with the observed pressure oscillations.

3.1.1.1 Experimental Setup

The injector studied here was a Dual Annular Counter Rotating Swirl (DACRS) injector designed and fabricated by General Electric Aircraft Engines. This injector consists of two swirl rings that counter rotate air at specified swirl angles. The rings are made of curved vanes for better aerodynamics and smaller pressure losses. Before burning, the air is swirled and mixed with natural gas at a given equivalence ratio. Two combinations of swirl angles were studied: a 45º/55º and a 55º/65º swirl combination, where the angles represent the outer and inner ring angles respectively. The natural gas fuel was introduced through the outer swirl vanes using three injection holes on each of the ten swirl vanes. The swirl rings are attached to a center body that is tapered to a point at the dump plane. A photograph of the injector is shown in Fig. 3.1.

For the DACRS injector, the injection holes were sufficiently small to be choked, thus preventing any modulation of the natural gas mass flow rate. The chamber setup for the injector

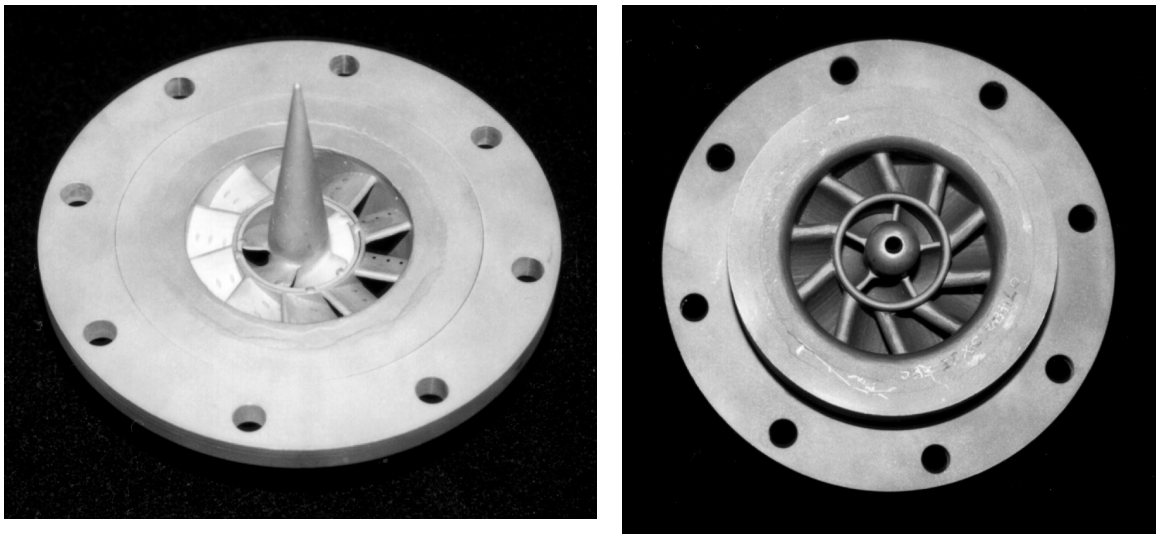

Fig. 3.1. Photograph of the Dual Annular Counter Rotating Swirl (DACRS) injector.

is shown schematically in Fig. 3.2. The modularity of the design allows for variation of the total chamber length in order to study its effects on combustion instability behavior. Chamber lengths of 235 mm and 350 mm were chosen for this study. Their respective residence times of 5.5 ms and 8 ms correspond to high flow velocities characteristic of real gas turbine engine conditions. To acoustically isolate the combustor and the injector, the combustor design includes two sonic choked points, one located upstream of the injector, one located at the exit nozzle of the combustor. Also shown in Fig. 3.2 is the fully optically accessible cylindrical quartz section.

3.1.1.2 Results and Discussion

3.1.1.2.1 Characterization of Instability Modes

Almost every encountered instability displayed the same characteristic properties in terms of the observed modes and corresponding frequencies. The pressure records show a strong mode (around 1200 Hz *and 1800 Hz* for the 350-mm long *and the 235-mm long* chambers respectively) superimposed with its much weaker first harmonic. Pressure profiles from transducers located at the same axial but different angular locations are always nearly identical. Therefore

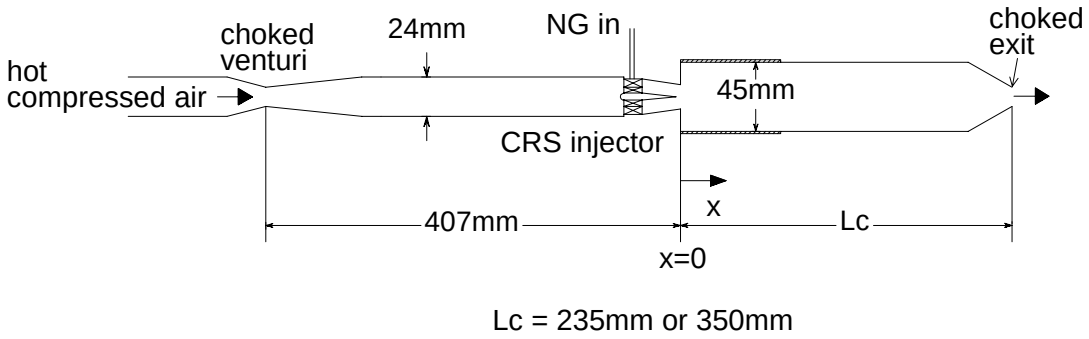

Fig. 3.2. Experimental Setup for DACRS Injector.

circumferential modes can be ruled out. Furthermore, pressure measurements from transducers located at different axial locations were always clearly out of phase, indicating that the two modes must be longitudinal. A simple 1-D analysis of the acoustics in the chamber indicated that the modes present are the first longitudinal mode of the combustion chamber and its harmonic.

The pressure profile in the combustor is well known and closely resembles that of a pure 1L (and 2L) standing wave in the combustor, between the dump plane and the exit nozzle. The amplitude profiles of these acoustic modes are represented in Fig. 3.3. The 2L mode is negligible compared to the 1L mode everywhere in the chamber, except maybe in the middle part. In particular, only the 1L mode is of significance in the region of the heat release zone, whatever the flow conditions and chamber configuration employed, which simplifies the correlation between heat release and pressure oscillations.

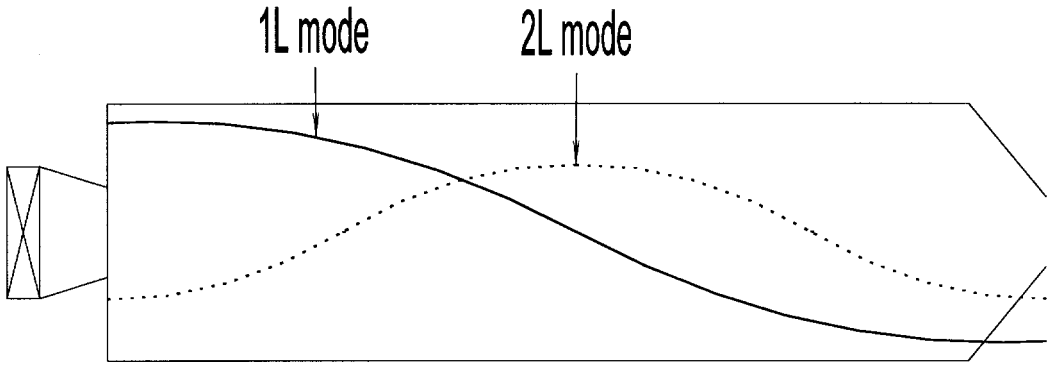

Fig. 3.3. Amplitude Profiles of 1L and 2L Acoustic Modes.

3.1.1.2.2 Effect of Equivalence Ratio

235-mm Long Chamber

Using the 45º/55º DACRS injector, tests were conducted using the shorter (L_c=235 mm) of the two chambers studied. For this chamber length, it was quite difficult to produce instabilities. The stability map for this case is shown in Fig. 3.4. In particular, higher chamber pressures and richer mixtures were needed (no instabilities were found at pressures equal to or less than 0.36 MPa). Even then, the amplitudes were always fairly small with maximum values corresponding to 5% of the chamber pressure.

350-mm Long Chamber

The 350-mm long chamber produced drastically different instabilities with the following general trends. For both DACRS injectors, the flame became unstable if the inlet air temperature T_o and the equivalence ratio ϕ were increased to values higher than threshold values

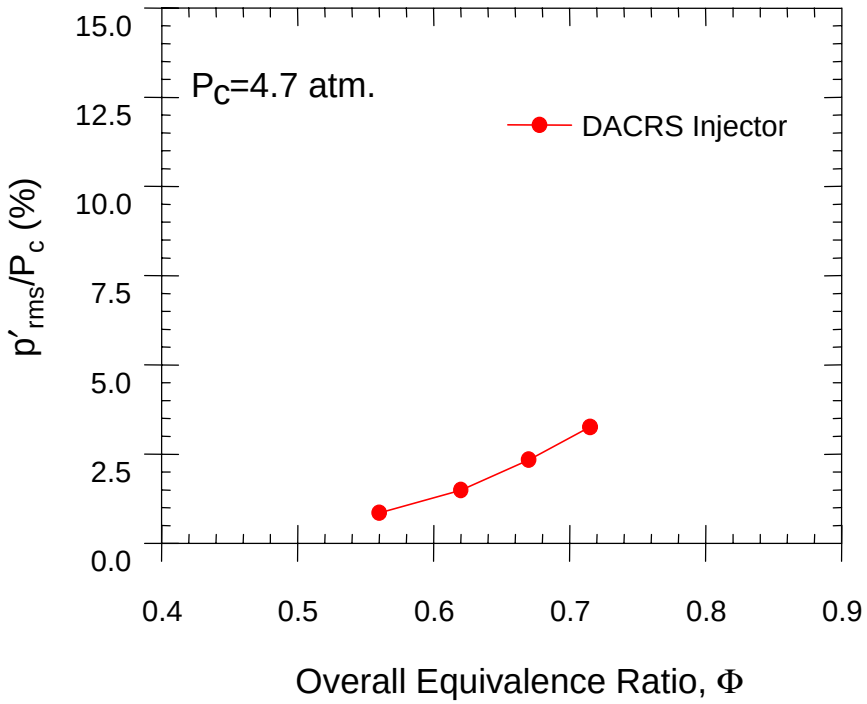

Fig. 3.4. Stability map obtained for the 235-mm long combustion chamber.

$T_{0min} \cong 672$ K and $\phi_{min} \cong 0.59$ respectively. In Fig. 3.5, the stability maps for both DACRS injectors are quite similar, with that for the 55°/65° swirler being slightly shifted towards leaner conditions. Both curves show very high maxima with respect to amplitudes of the observed combustion instabilities (18% rms of the chamber pressure P_c, i.e. more than 25% absolute amplitude). At higher values of ϕ, the instabilities become weaker but are still substantial. Another important trend is that the instabilities died out at the leanest conditions well before LBO, which typically occurred around ϕ = 0.48 - 0.50. This is particularly interesting to note since combustion instabilities are commonly thought to occur (or at least worsen) towards the leanest conditions.

Some experiments were conducted in a "fully premixed" mode with both DACRS injectors. The natural gas was injected upstream of the inlet choked venturi instead of being

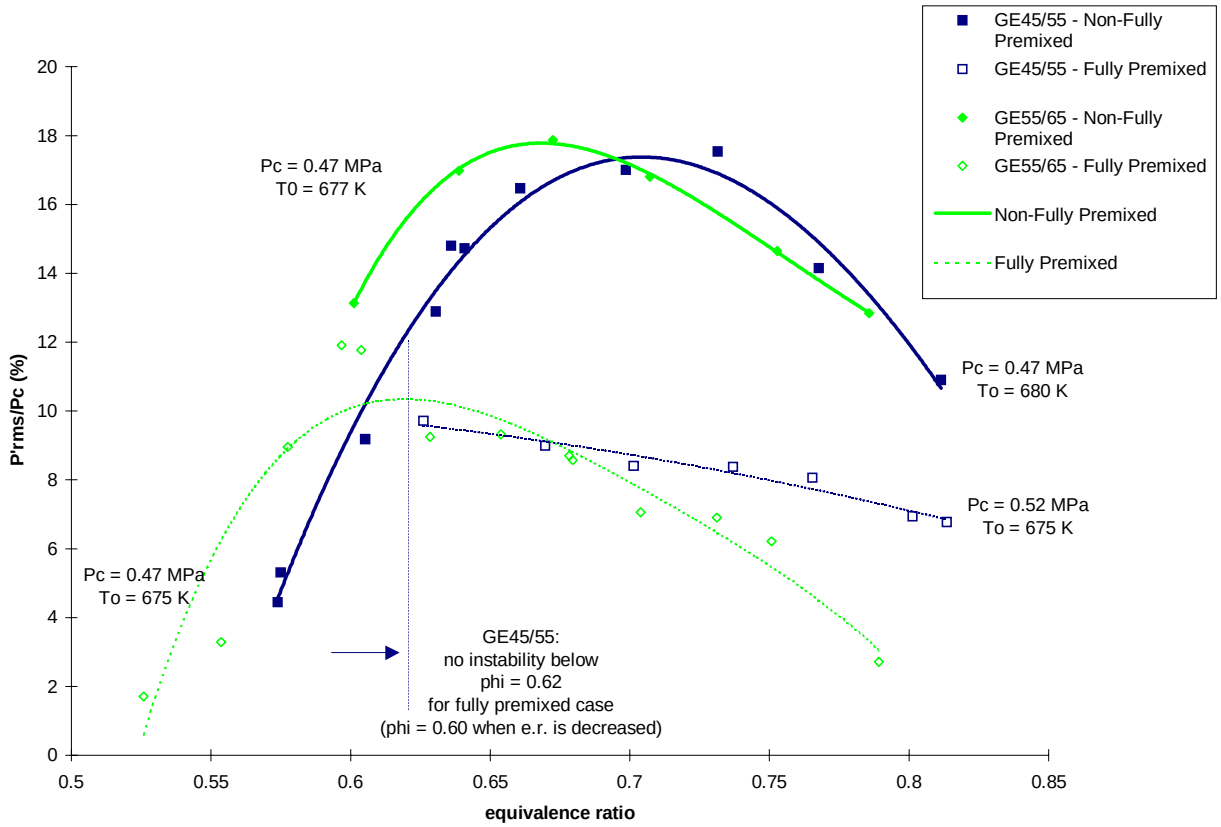

Fig. 3.5. Stability map obtained for DACRS injectors for the 350-mm long chamber.

injected through the swirl vanes. The goal of this procedure was to ensure a completely uniform premixed combustible mixture entering the combustor, but also to provide a time-constant equivalence ratio independent of the presence of any combustion instability. Strong instabilities were still observed even though the level of the oscillations amplitude remained significantly lower than the level observed for the normal injection case. The corresponding stability maps for the DACRS injector are represented by the lines shown in Fig. 3.5. The maximum amplitude of the observed combustion instabilities under these fully premixed conditions was about the same for both DACRS injectors (about 10% rms of chamber pressure), but the shape of each stability curve was quite different. For the 45°/55º DACRS swirler, significant hysteresis effects were observed with respect to equivalence ratio. When ϕ was increased above 0.62, instabilities set in suddenly and then decreased only slowly at richer conditions. When ϕ was then decreased, instabilities disappeared at a lower value of 0.60. For the 55°/65º DACRS swirler, the stability curve follows a more dome-like shape, with unstable conditions occurring only when $0.53 < \phi < 0.80$.

The pressure amplitudes observed for the combustion instabilities obtained during fully premixed operation were about half the amplitude of those observed when the natural gas was injected through the swirl vanes. A possible explanation is the absence of one mechanism often seen as playing a major role in driving instabilities, namely the equivalence ratio modulation [4-7]. In all experiments, pressure oscillations could not propagate upstream past the choked venturi. Hence, by injecting the fuel upstream of this choked venturi, the equivalence ratio was kept constant, decoupled from and independent of any instability occurring downstream. Under these conditions, there could not be any equivalence ratio modulation. However, the fact that combustion instabilities still occurred, although at a lower strength,

indicates that in these fully premixed experiments, other mechanisms were responsible for the sustenance of the observed instabilities. This result is not really surprising since combustion instabilities are often the result of several mechanisms coupled together [8]. One such mechanism could be a total mass flow rate modulation upstream of the dump plane [3,8]. The importance of this potential mechanism is currently under investigation.

3.1.1.2.3 Effect of Inlet Temperature

For both DACRS injectors, when the equivalence ratio was fixed at a value higher than $\phi_{min} = 0.59$, an increase of the inlet air temperature to a value higher than $T_{0min} = 672$ K did not alter the strength of the instabilities significantly, as shown in Fig 3.6. However, similar to the hysteresis effect with respect to equivalence ratio described earlier, very significant hysteresis effect with respect to temperature was observed. When T_0 was reduced below T_{0min}, the instabilities generally weakened but did not disappear until T_0 was significantly reduced below T_{0min},, sometimes to levels as low as 616 - 628 K.

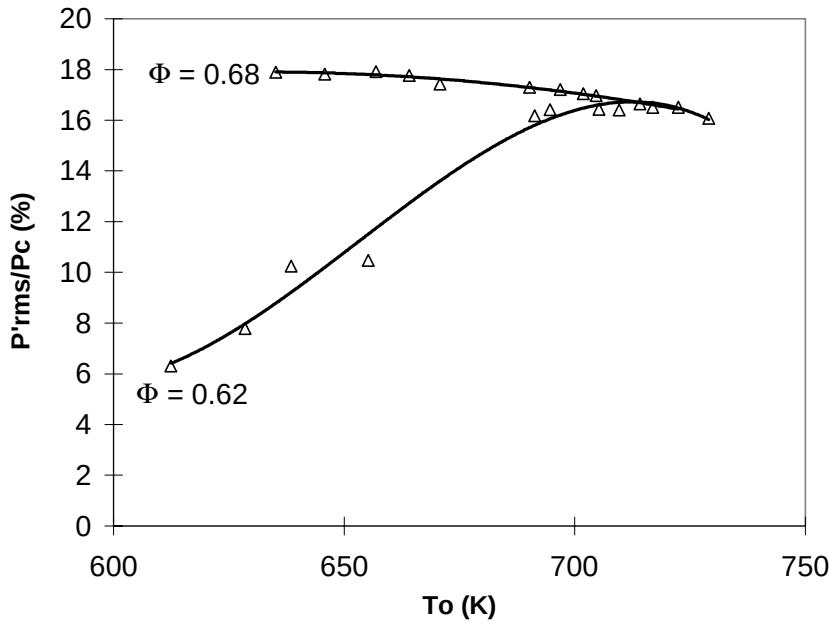

Fig. 3.6. Effect of Inlet Air Temperature on Instabilities Obtained for DACRS Injector GE55º/65º with the 350-mm long Combustion Chamber (P = 0.45 MPa).

It should be noted that the value of T_{0min} had a slight dependence on equivalence ratio. Specifically, it decreased slowly with the increase of ϕ, for example $T_{omin} \cong 678$ K at $\phi = 0.59$ and $T_{omin} \cong 655$ K at $\phi = 0.70$. Hence, richer mixtures tended to exhibit unstable operation for lower inlet temperatures than leaner mixtures. This trend was amplified with the hysteresis effect mentioned previously, i.e. unstable flames at richer conditions remained unstable at an even lower inlet temperature when the inlet temperature was decreased. This explains why, in Fig. 3.6, the flame at $\phi = 0.68$ is still unstable at $T_o = 633$ K while it is already much less unstable at $\phi = 0.62$.

3.1.1.2.4 Phase-Resolved CH Chemiluminescence Images of Unstable Combustion*

CH* chemiluminescence images were taken in order to obtain the temporally resolved structure of the flame heat release zone associated with pressure dynamics. CH* chemiluminescence images are shown in Fig. 3.7 for the DACRS injector. The results show a strong temporal correlation between the dynamic pressure and the CH* chemiluminescence intensity. During the minimum of the local pressure fluctuations, the flame is weak but when the pressure fluctuation rises and approaches its maximum value, the flame becomes quite intense. Hence, the heat release occurs precisely during the maximum of the pressure amplitudes corresponding to images 2 through 6, thus satisfying Rayleigh's criterion.

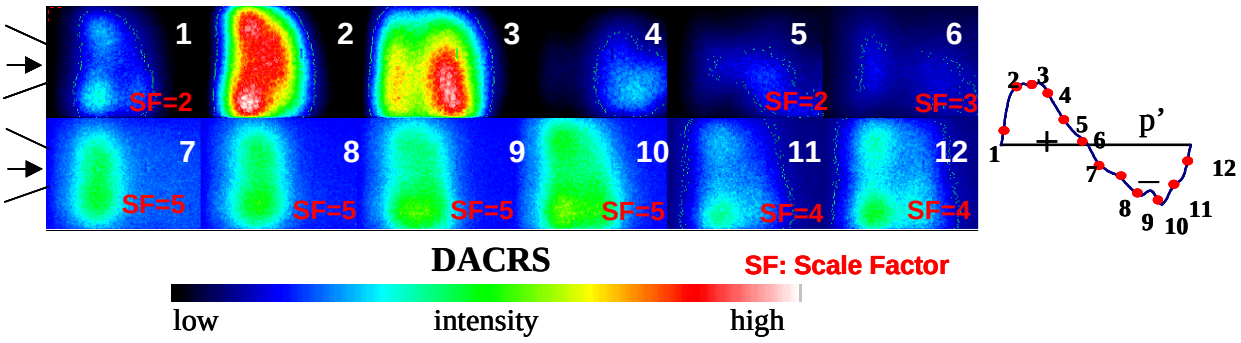

Fig. 3.7. Phase-resolved CH* chemiluminescence for the DACRS 55º/65º injector (P = 0.43 Mpa, $\phi = 0.62$, $T_0 = 705$ K). Chamber length is 350 mm.

3.1.1.3 Summary

Under the conditions most relevant to real gas turbine applications (residence time 5.5 ms, i.e. 235-mm long chamber configuration), the DACRS injectors showed excellent combustion stability characteristics over a wide range of equivalence ratios and inlet temperature conditions. The use of a counter rotating swirl configuration may contribute to the stability through effects on the fluid mechanics occurring in the region of the dump plane. The DACRS injector exhibited a uniformly distributed flame that extended over a greater portion of the combustion chamber. For the 350-mm long combustion chamber, significant combustion instability was observed for the DACRS swirl injector. For the longer combustion chamber conditions, the region over which the 1L mode can be influenced, that is driven, extends further from the dump plane than in the shorter chamber length case. Thus, more of the flame energy release is capable of coupling to the pressure sensitive response region to sustain instabilities. Combustion instabilities observed under fully premixed conditions indicate that a combination of mechanisms is responsible for the instabilities encountered in our study. One such mechanism could be a total mass flow rate modulation upstream of the dump plane. The importance of this potential mechanism is currently under investigation.

3.1.2 Experimental Definition for Trapped Vortex Combustor

The Trapped Vortex Combustor (TVC) is a recent development in low emissions combustion devices that can be utilized equally well in land or air based gas turbine systems. This new technology offers the promise of increased fuel efficiency, higher flow-through velocities, lower pressure drops, reduced emissions, and increased combustion efficiency.

Additionally, the TVC is purported to be far less susceptible to combustion instability and can provide a dramatic reduction in the Lean Blow Out (LBO) limit.

The basic configuration for a TVC is two concentric canisters separated by an annular ring, as shown in Fig. 3.8. Primary air is introduced in the center of the upper canister, and the fuel and secondary air are introduced in such a manner as to create a stably-burning vortex trapped between the upper and lower annular rings. The primary air interacts with the burning vortex ring and carries the lean burning mixture into the second canister. One advantage of the TVC is that premixed fuel may be added with the primary air, which may have a dramatic effect on the overall combustion process.

A Trapped Vortex Combustor supplied by Wright-Patterson AFB will be used for experiments in the next phase of the program. Typical operational conditions for this unit at atmospheric pressure are as follows. The primary airflow is nominally constant at 0.25 lbm/s and the equivalence ratio for the vortex is typically maintained at about 0.8. Overall equivalence ratio is then changed by changing the flowrates of fuel and air supplied to the vortex. The TVC is shown installed in the Penn State Gas Turbine experimental facility in Fig. 3.9. The flow is

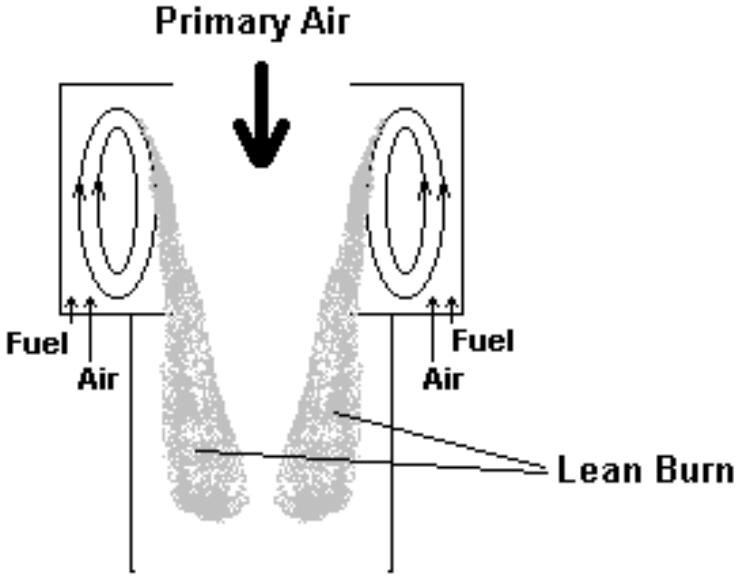

Fig. 3.8. Schematic showing basic principles of a Trapped Vortex Combustor (TVC).

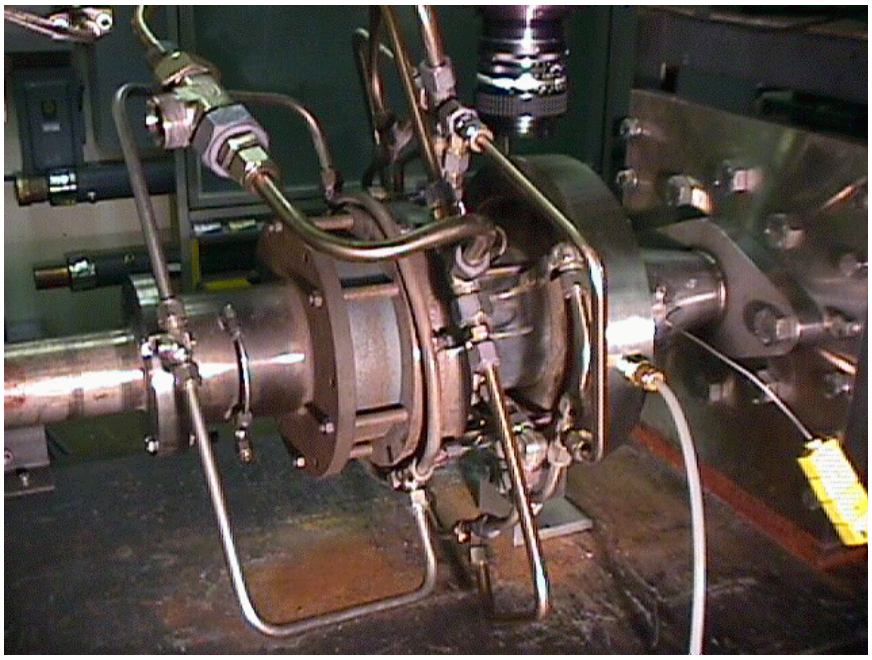

Fig. 3.9. TVC supplied by Wright Patterson Air Force Base installed in Penn State's Gas Turbine Facility.

from left to right. The secondary air and fuel inlet lines begin in the upper left of the picture and feed the rings surrounding the upper cavity. The second cavity is fitted with an optically accessible quartz section and the CCD camera can be seen in the upper middle of the picture. The second cavity is attached to a water-cooled stainless steel adapter cone that connects the TVC to the Gas Turbine exhaust system.

Preparations for testing the TVC are almost complete and include plans to make full use of the extensive diagnostic capabilities available in the High-Pressure Gas Turbine Combustion Laboratory. Initially, acoustic and visual measurements, as well as NO_x emissions, will be made over the range of equivalence ratios from LBO to stoichiometric. Modification of the current device will provide the capability of installing high-speed pressure transducers to record pressure fluctuations and enable phase resolved CH* chemiluminescence. The effect of adding premixed fuel in the primary air stream will also be analyzed. Other tests under consideration are the variation of fuel type and utilizing Laser Induced Incandescence (LII) to measure soot formation.

3.2 Numerical Modeling of Gas Turbine Combustion

A comprehensive numerical analysis based on the large-eddy-simulation (LES) technique has been established to provide detailed information about the flame dynamics and its interaction with unsteady flow motions in a premixed, swirl-stabilized gas turbine combustor. The purposes of this task are (1) to use validated LES techniques to systematically investigate the key mechanisms responsible for driving combustion oscillations of a single swirl-stabilized injector, and (2) to present the result in a form that can be readily incorporated into the global stability analysis of a full-scale gas turbine engine.

The theoretical formulation is based on the Favre-filtered conservation equations of mass, momentum, energy, and species concentration in three dimensions, and accommodates finite-rate chemical kinetics and variable thermophysical properties. Turbulence closure is achieved by means of a large-eddy-simulation (LES) technique with the unclosed subgrid-scale terms modeled using the compressible version of the dynamic Smagorinsky model (DSM) [9,10]. A single-step global chemical kinetics scheme, involving five species, is used to treat the chemical reaction of methane with air. The numerical analysis employs a density-based, finite-volume methodology. Spatial discretization is obtained using a fourth-order, central-differencing method in generalized coordinates. A sixth-order numerical dissipation with total-variation-diminishing (TVD) switch is included to ensure computational stability and to prevent numerical oscillations in regions with steep gradients. Temporal discretization is obtained using a third-order semi-implicit Runge-Kutta integration scheme developed by Zong [11] to circumvent the stiffness problem arising from strong chemical reaction source terms. The numerical scheme is implemented on an in-house parallel computing facility consisting of 156 Pentium II 400 MHz processors. A Multi-Block technique based on domain decomposition is employed to parallelize

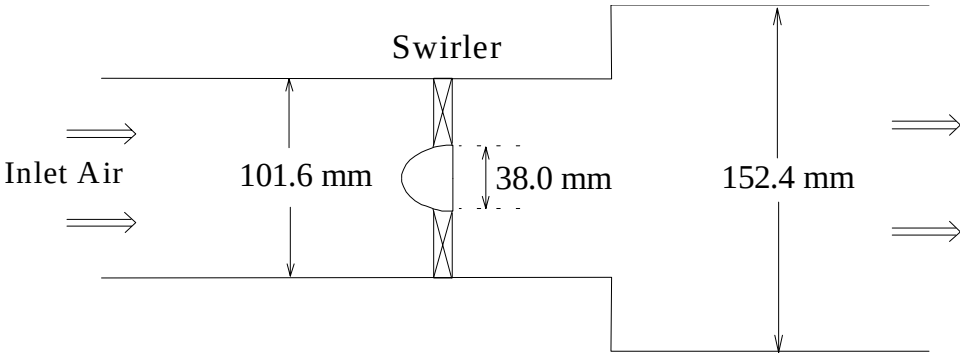

Fig. 3.10. Schematic of swirling flow combustor.

the code. The Message Passing Interface (MPI) library is used to exchange information among processors, i.e., blocks. The parallelization methodology is robust and linear speedup is achieved.

3.2.1 Model Validation

To validate the capability of the code for swirling flow calculations, experimental results were obtained from the Propulsion Directorate of the Air Force Research Laboratory at Wright-Patterson Air Force Base [12]. Fig. 3.10 shows the experimental apparatus. The working fluid is air that is forced through the chamber by a centrifugal type blower. A swirler with 12 circular arc inlet guide vanes is located at 50.8 mm upstream of the dump plane. The leading edge of each blade was designed to be tangential to the incoming flow and perpendicular to the centerline of the combustor. A laser Doppler velocimeter (LDV) was used to measure the three velocity components and some turbulence quantities at different swirl numbers. The centerline velocity in the inlet pipe is 19.2 m/s and inlet Reynolds number is 125,000 based on the inlet radius. The computational domain is composed of 28 blocks assigned to each processor, i.e., total 28 processors, for parallel computation. The numbers of the grid points are 160x75x81 in the axial, radial, and azimuthal directions, respectively, which are clustered in the shear layer and near the

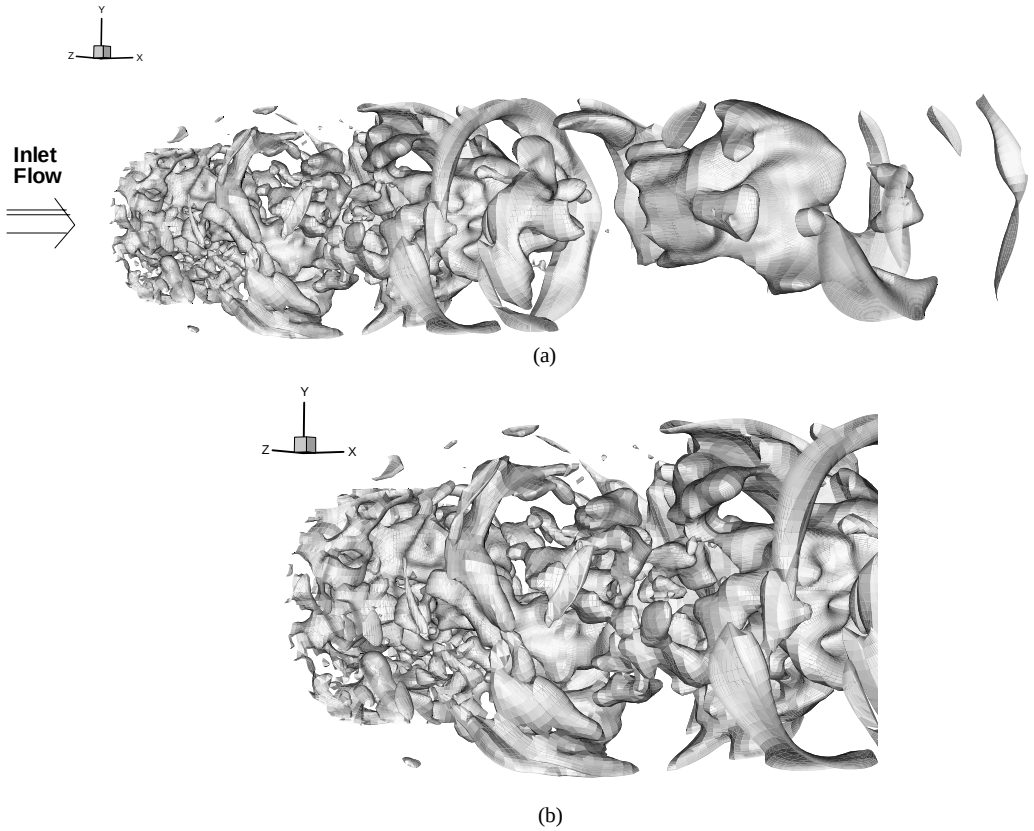

Fig. 3.11. Vortical structures visualized using isosurfaces of instantaneous pressure fluctuations. (a) entire domain (b) zoomed near the dump plane.

interface between the inlet and the chamber. The azimuthal grid is uniformly distributed. A flow structure snapshot illustrated by instantaneous pressure fluctuation isosurfaces is shown in Fig. 3.11. The measured and calculated velocity component comparisons at various axial locations are shown in Fig. 3.12. The solid lines correspond to the numerical result, and the symbols to the measured data. Good agreement of the axial velocity component is obtained. The azimuthal (swirl) velocity near the dump plane (see Fig. 3.12b-1) was over-predicted. However, given the low velocity condition and experimental uncertainty, no conclusive remarks can be given at this point about the numerical accuracy in comparison with measurement error. Fig. 3.13 shows that turbulent kinetic energy varies significantly in the radial direction. The over-prediction of turbulent kinetic energy near the shear layer of the center recirculation

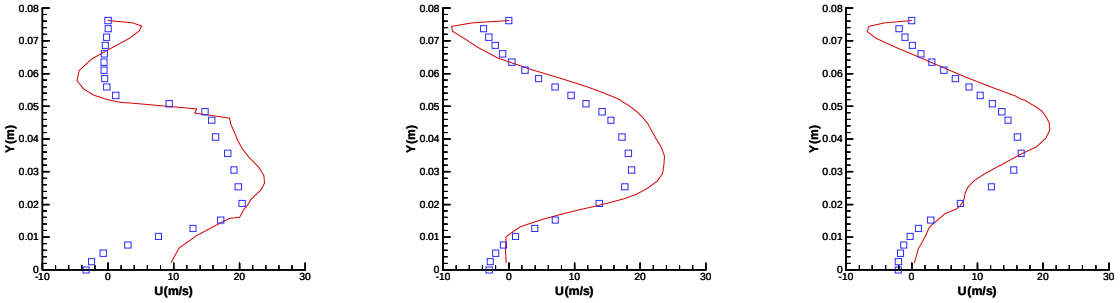

(a-1) X/H=0.38 (a-2) X/H=2.0 (a-3) X/H=4.0

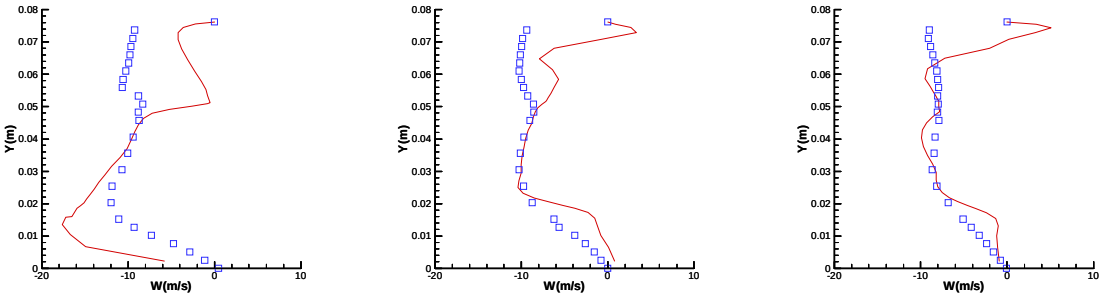

(b-1) X/H=0.38 (b-2) X/H=2.0 (b-3) X/H=4.0

Fig. 3.12. Comparison of experimental and computational results of mean velocity a) axial component and (b) azimuthal component (line :computation ; symbol: experiment).

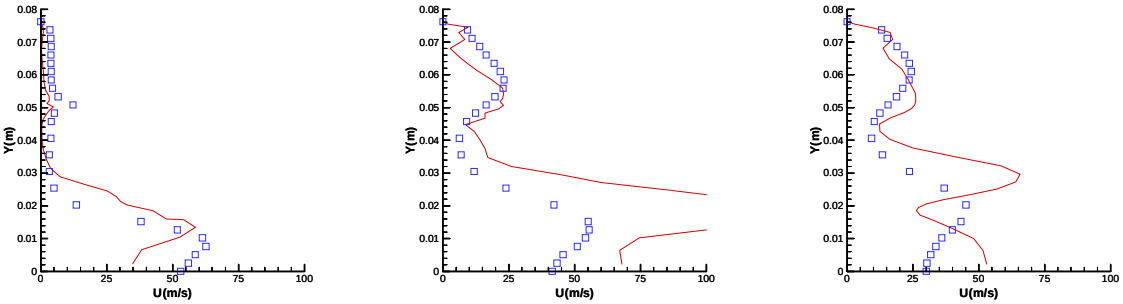

(a-1) X/H=0.38 (a-2) X/H=2.0 (a-3) X/H=4.0

Fig. 3.13. Comparison of experimental and computational results of turbulent kinetic energy (line :computation; symbol: experiment).

zone may be related to the uncertainty of the inlet velocity profiles and the subgrid model used. More effort should be expended in the future to improve the subgrid turbulence modeling. In spite of the few discrepancies observed, the overall agreement between measurements and predictions seems quite acceptable. Fig. 3.14 shows a snapshot of the instantaneous vorticity contours. The flow is highly dynamic. The conventional turbulence-closure scheme based on the Reynolds-averaging technique apparently fails to capture the important flow physics.

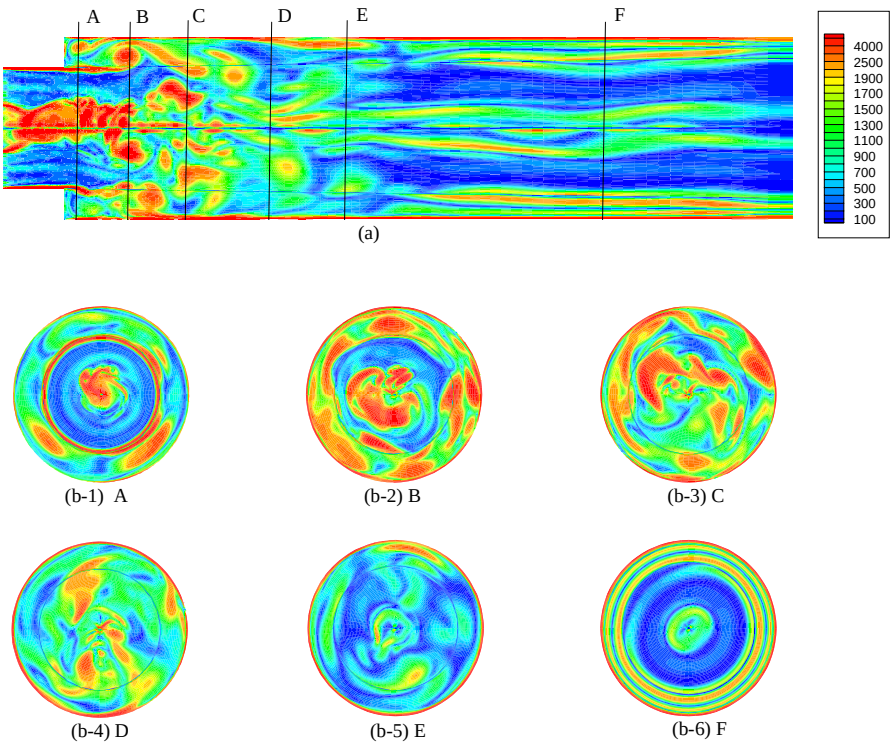

Fig. 3.14. Instataneous vorticity magnitude (a) x-y cross section (b) y-z cross section at different axial location.

3.2.2 Flame Dynamics of a Swirl-Stabilized Injector

The analysis has been employed to study the combustion dynamics in a premixed, swirl-stabilized combustor (i.e., the Penn State lean premixed combustor). The model combustor of concern consists of a single-swirl injector, an axisymmetric chamber, and a choked nozzle, as shown in Fig. 3.15. The swirler has eight straight, flat vanes with angles of 45° relative to the incoming air. The corresponding swirl number is about 0.69. Natural gas is injected radially from the center body through ten holes immediately downstream of the swirler vanes. The fuel/air mixture is expected to be well premixed before entering the combustor. The chamber measures a diameter of 45 mm and a length of 207 mm. The choked nozzle at the exit prevents any downstream disturbances from travelling upstream and to maintain the desired chamber pressure. The baseline condition includes an equivalence ratio of 0.6, a chamber

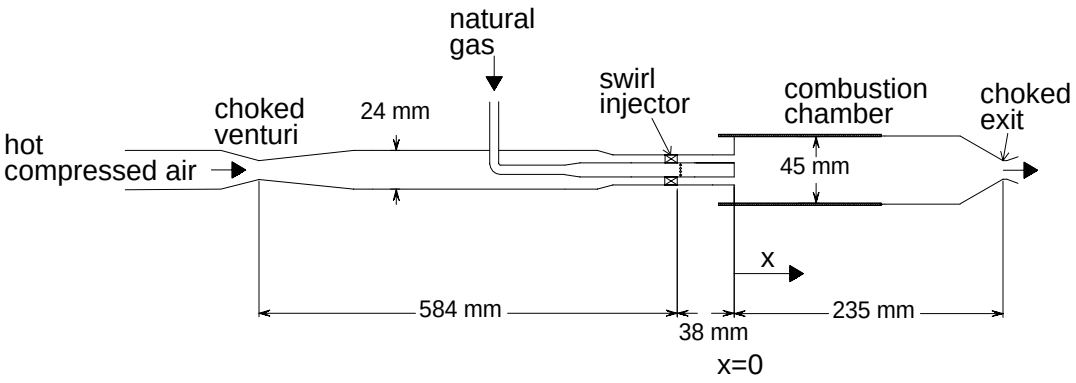

Fig. 3.15. Schematic of a model gas turbine combustor.

pressure of 4 atm, an inlet temperature of 670 K, and an inlet velocity of 83 m/s, corresponding to the case of unsteady combustion.

According to the experimental observations, the combustor exhibits strong flow oscillations when the inlet temperature and/or equivalence ratio exceed certain threshold values. The dominant acoustic motion corresponds to the first longitudinal mode, with the amplitude of pressure fluctuation as high as 20% of the mean chamber pressure. Since there exists an acoustic pressure node at the middle of the chamber, the computational domain only includes the upstream half of the chamber, with a constant back pressure specified at the exit plane. The entire grid system has 135x110x81 points along the axial, radial, and azimuthal directions, respectively, of which 25 axial points are used to cover the inlet section. The axial and radial grids are clustered in the shear-layer regions downstream of the dump plane and near the solid walls. The azimuthal grids are uniformly distributed. This grid resolution was chosen based on the inlet Reynolds number such that the largest grid size falls in the inertial range of the turbulence energy spectrum.

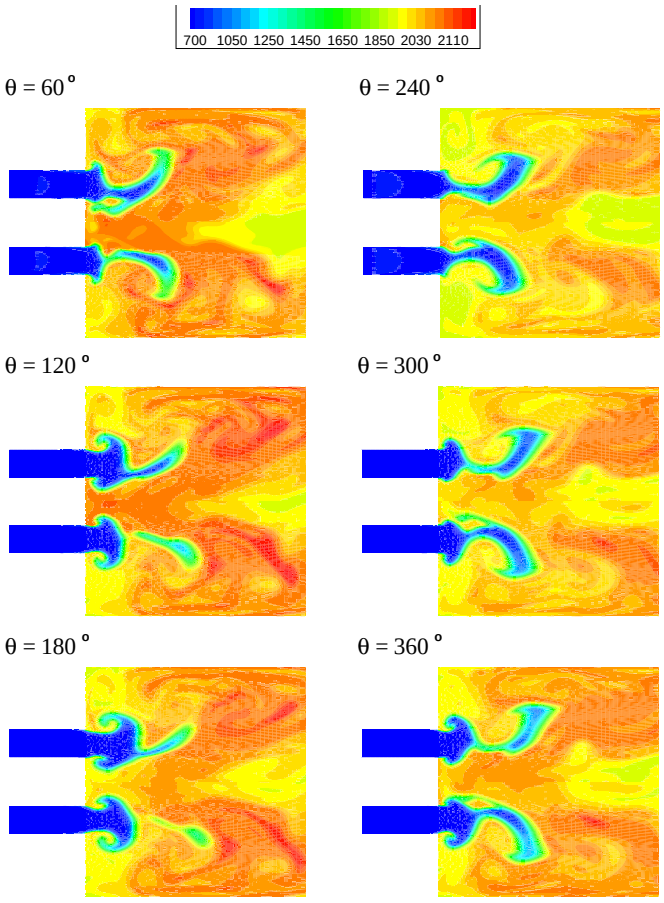

Fig. 3.16. Temperature contours on x-y plane over one cycle of oscillation.

To expedite numerical computation, the analysis was conducted on a distributed-memory parallel computer. The computational domain was divided into 102 blocks and each block is calculated on a single processor, i.e., a total number of 102 processors are used.

Calculations of turbulent flame dynamics were initiated by imposing broadband velocity fluctuations at the inlet, and continued for an extended period of time until statistically meaningful data was obtained. A spectral analysis of the calculated pressure fluctuation shows the existence of a dominant harmonic at 1905 Hz, which corresponds to the first longitudinal acoustic mode of the chamber. The amplitude of pressure oscillation is about 9.3% of the mean chamber pressure. Both results agree well with experimental measurements. Figs. 3.16 and 3.17

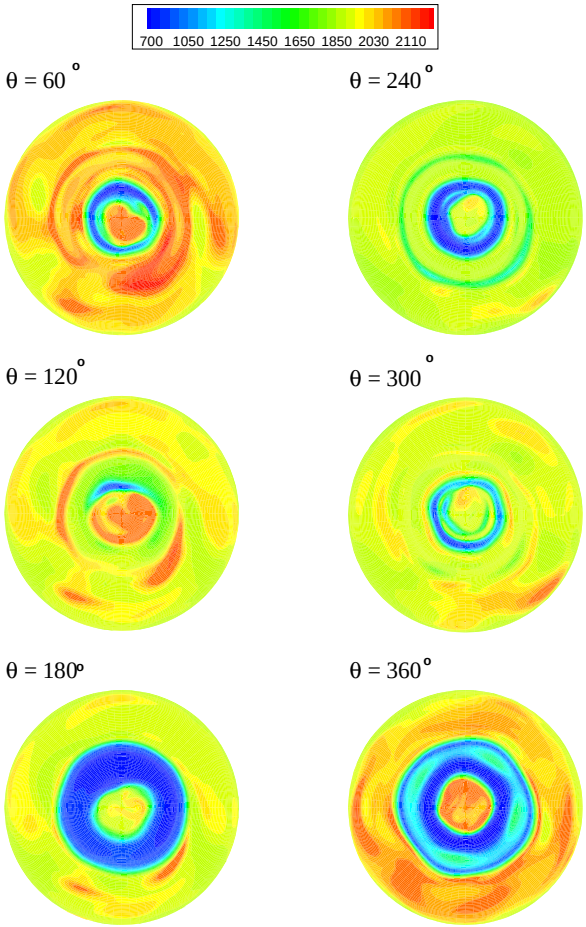

Fig. 3.17. Temperature contours on y-z plane (x = 2.3 mm) over one cycle of oscillation.

present the temperature evolution in the upstream of the chamber on the x-y and y-z planes, respectively, over one cycle of oscillation. The corresponding heat-release distributions are given in Fig. 3.18, which are obtained from the multiplication of the fuel consumption rate and the heat of reaction of the fuel. The phase angle, θ, is referenced with respect to the acoustic pressure of the first longitudinal mode at the chamber head-end. The calculated flame temperature of 2050 K is slightly higher than its equilibrium value of 1980 K, mainly because of the use of the global chemical kinetics scheme and the lack of subgrid turbulent mixing in the modeling of species mass production rate. Nonetheless, the analysis allows for a comprehensive

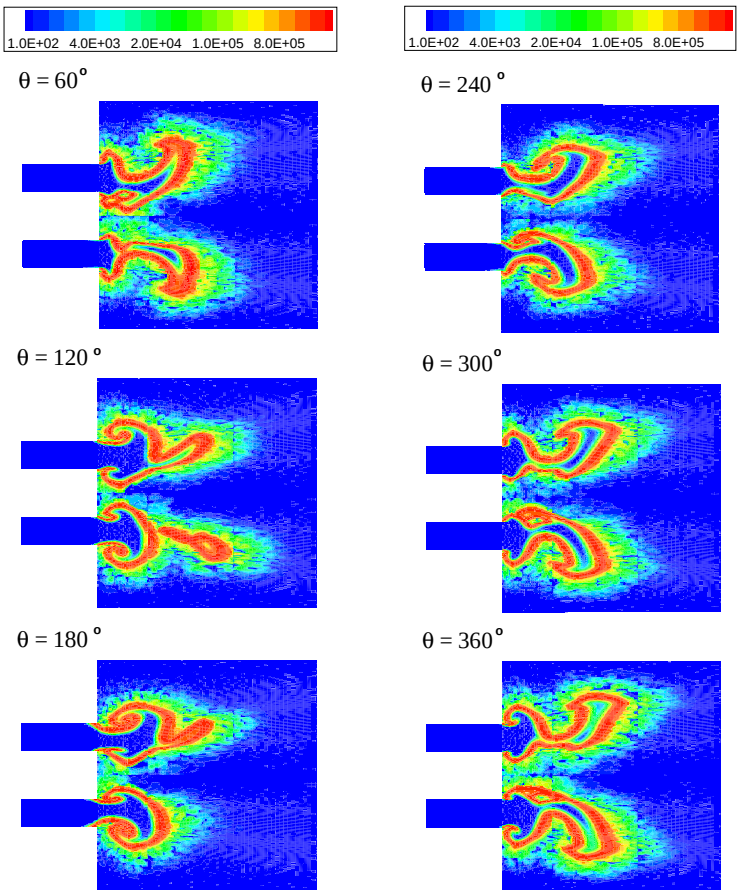

Fig. 3.18. Contours of heat release rate on x-y plane over one cycle of oscillation.

investigation into turbulent flame dynamics, and, for the first time, accurately predicts the detailed flame evolution and chamber acoustic properties *a priori*.

The temperature contours clearly exhibit a double-surface envelope flame anchored at the edges of the center body and the backward-facing step. This is in sharp contrast with the flame structure under stable operating conditions that shows only a single conical flame anchored to the centerbody [3]. One major factor contributing to this phenomenon is the relatively higher inlet temperature and equivalence ratio in the present study compared to the case of stable combustion. As a result, the chemical induction time is shortened and becomes comparable to the flow residence time in the corner circulating zone downstream of the dump plane. A flame is

thus established in that region, and merges with the one originating from the centerbody. The overall flame length is substantially reduced. This situation renders the combustor more prone to instabilities according to the Rayleigh criterion [13], since much heat release occurs within a short distance close to the chamber head-end (i.e., acoustic anti-node point).

The flame dynamics can be elucidated by considering its interaction with the local oscillatory flowfield. The entire process is dictated by the temporal evolution and spatial distribution of the cold flow entrainment into and mixing with hot gases in the vortical structures in the chamber. During the pressure build-up stage (θ = –90°, or 270°, to 90°), the increasing pressure at the dump plane prevents the fresh mixture from entering the chamber. The flame zone is thus reduced and becomes a little compact. In the next phase (θ = 90° to 270°), the decreasing pressure facilitates the delivery of the cold flow into the chamber. More intensive heat release thus follows after a short fluid mixing and chemical induction time. The resultant flow expansion tends to push the flame outward and simultaneously block the inlet flow at the dump plane. Unburned mixture fragments may break up away from the main stream, and are convected downstream and generate local hot spots. It should be noted that the above description of flame evolution is not precisely reflected in the temperature contours shown in Fig. 3.16 due to the various time delays involved in the process, but the qualitative trend remains valid.

Vorticity is of serious concern in the present study because of its dominant influence on the unburned flow entrainment and its subsequent reactions in the flame zone. Fig. 3.19 shows a snapshot of vorticity intensity on the x-y and y-z planes at θ = 120°, respectively. Large vortical structures arise in the shear layers downstream of the dump plane and around the wrinkled flame zone. In addition to the swirling-flow induced vorticity, the volume dilation and baroclinicity

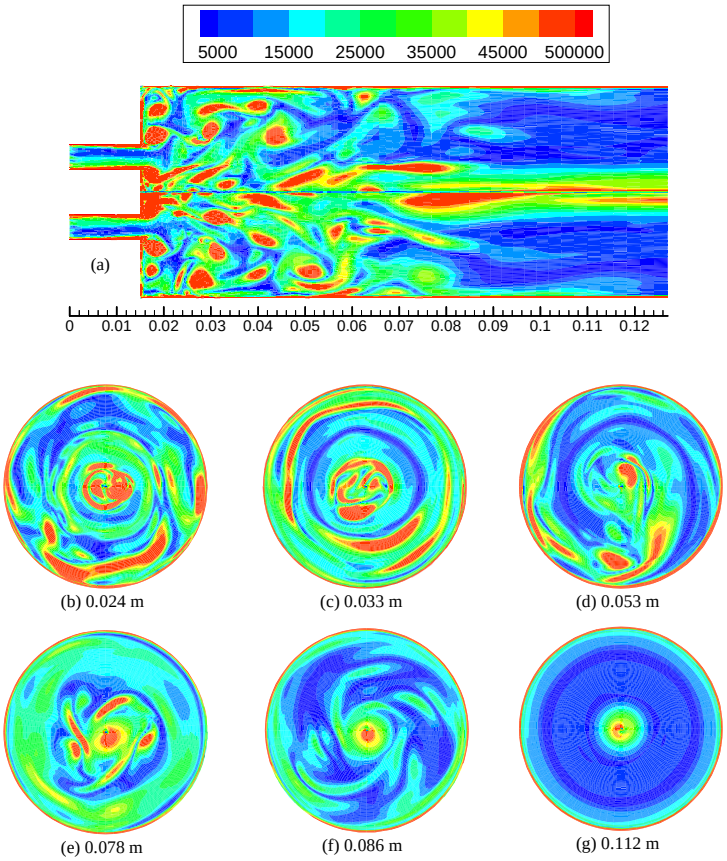

Fig. 3.19. Snapshot of vorticity field on x-y and y-z planes, $\theta = 120°$.

effects in the flame zone significantly contribute to its production. The vorticies are convected downstream with accompanying irregular breaking strength (i.e., vortex breakdown), and spiral into the core region after breakdown. This precessing vortex core may induce strong flow oscillations, and consequently lead to the acoustic instability in the chamber.

The mutual coupling between heat release and acoustic motions can be characterized using the Rayleigh parameter [13], $R(\boldsymbol{x})$, defined as the time-averaged product of the pressure oscillation $p'(\boldsymbol{x},t)$ and heat release fluctuation $q'(\boldsymbol{x}\ t)$. It provides a qualitative measure of the extent to which unsteady heat release drives or suppresses instabilities. The acoustic oscillation is amplified if $R(\boldsymbol{x}) > 0$, or damped out if $R(\boldsymbol{x}) < 0$. Fig. 3.20 presents the spatial distributions of the Rayleigh parameter normalized by the maximum $R(\boldsymbol{x})$ in the field on the x-y and y-z planes,

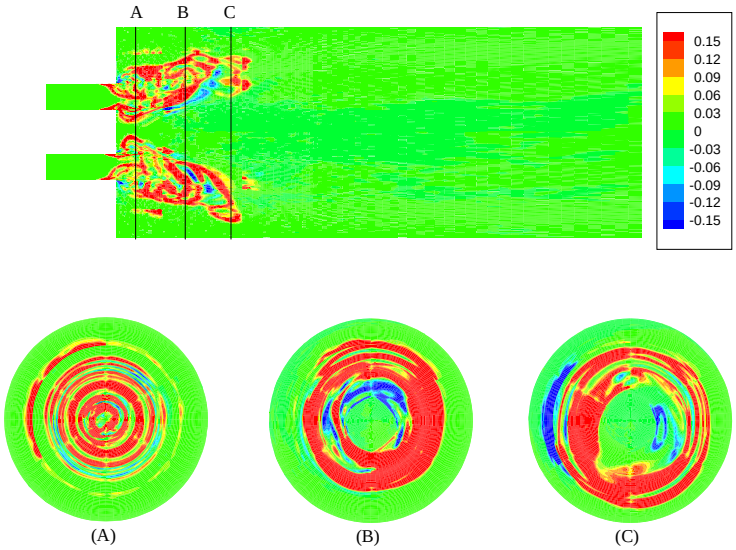

Fig. 3.20. Spatial distributions of Rayleigh's parameter on x-y and y-z planes.

respectively. The Rayleigh parameter has a positive value in much of the volume in the flame zone. The acoustic field is favorably correlated with the unsteady heat release, and as such strong instabilities take place in the chamber. The figure also shows that as a result of the flame compactness compared with the chamber length, the energy transfer from the flame zone to the oscillatory flowfield occurs in a short distance near the acoustic pressure node; this condition

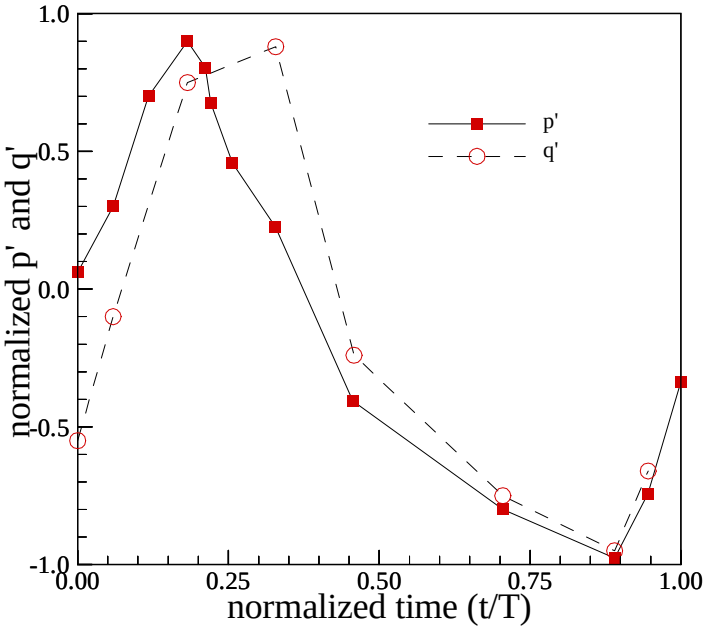

Fig. 3.21. Normalized pressure and heat release fluctuations.

further promotes the excitation and sustenance of combustor instability. The global effect of heat release on acoustic oscillation is measured by plotting the net heat release in the chamber versus the acoustic pressure in the middle of the flame zone. The result is shown in Fig. 3.21, which was obtained by integrating the instantaneous heat release over the entire volume at 15 time instants within one cycle of oscillation. Clearly, the Rayleigh criterion for driving chamber instability is satisfied with the phase difference between the overall heat release and pressure fluctuation less than 50°.

IV Pulse Detonation Engine Studies Using Coal-based JP-900 (Task 3)

The use of detonations for propulsion has been of interest to the scientific and propulsion communities since the 1950's when it was considered for hypersonic aircraft. More recently, in the early 1980's, a number of national programs such as the National Aerospace Plane (NASP) program revived that interest and prompted several analytical and experimental studies on oblique detonation waves as an alternative to supersonic combustion [14]. Within the past decade interest has again developed in the use of detonations in a propulsion device in the form of Pulse Detonation Engines for airbreathing (PDE) and rocket applications (PDRE) [15]. Much of the relevant physics and chemistry issues related to the development of PDEs involve similar understanding of detonation phenomena to studies conducted in the past [16].

Pulse Detonation Engines (PDE) offer the potential for higher specific impulse (Isp), reduced complexity and lower operational costs as compared to current gas turbine technology [15]. One of the key barriers to the realization of an operational PDE lies in the difficulty to ignite the detonation wave in the engine in a reliable and repeatable manner. This barrier is particularly important for applications that involve hydrocarbon-air propellant combinations since it is well known that detonations are difficult to achieve within a practical length in hydrocarbon fuel-air mixtures. Since system engine weight is a key performance parameter, achieving a detonation rapidly is critical to the successful development of a PDE. In essence, meeting this challenge requires a fundamental understanding of deflagration to detonation phenomena and developing means to rapidly enhance the transition to a detonation that can be practicably integrated into engine technology.

The current approaches adopted for initiating a detonation in PDE studies often utilize a initiator, sometimes referred to as a pre-detonator, that produces a strong detonation wave that

then initiates a detonation in the main chamber of the PDE [17,18]. To date initiators using hydrocarbon fuels have required air mixtures that contain approximately 2% excess oxygen. For an operational PDE this approach is unacceptable from a systems perspective due to the added complexity and weight that providing a third propellant involves.

The research work carried out for this part of the delivery item includes both experimental and analytical aspects. The experimental phase of the program was focused on first designing and fabricating a series of modular initiator tubes for scientific investigation and optimization of design strategies for minimizing deflagration to detonation transitions (DDT) for fuel and pure air. The analytical phase of the program was focused on developing and refining numerical techniques for characterizing DDT physics. The experimental and analytical research work are presented and discussed in the following two sub-sections.

4.1 Pulse Detonation Engine Facility and Experiments

Due to the difficulty in scaling up of experimental results on detonations, it was particularly important to carefully select the size and geometry of the initiator. Because its only purpose is to induce a detonation in the main chamber, the practical initiator needs to be compact. However, minimizing the initiator size gives rise to conflicting requirements. For a given explosive mixture, Chapman-Jouguet (CJ) detonations cannot propagate in a tube whose diameter is significantly smaller than the cell width, λ, characteristic of the mixture [19,20]. For air-breathing applications where heavy hydrocarbon (HC) fuels must detonate in air, the corresponding cell width is quite large ($\lambda \sim 40$ - 50 mm), and the initiator cannot be made too small [21,22]. After careful consideration of all these factors, two initiator geometries were chosen for design and fabrication. The first initiator geometry has a circular cross-section with

an inner diameter of 34 mm. This geometry, with no visual access, was chosen to be the workhorse experimental initiator for studying design strategies for optimizing DDT lengths. The second initiator with a square cross section (44.5 ×44.5 mm) was designed and fabricated with optical access for more detailed laser-based experimentation of the DDT phenomenon.

4.1.1 Experimental Setup

In this sub-section, the two initiator geometries are detailed. The ignition system and propellant combinations used for the experiments are also presented.

4.1.1.1 Circular Cross-sectioned Initiator

A schematic and a photograph of the first initiator geometry are shown in Fig. 4.1. The initiator consists of a 1.5–inch stainless steel pipe, schedule 160, cut and fitted with flanges, which results in a flexible and modular system with an adjustable length from 0.3 to 1.83 m. Up to 9 high-speed, water-cooled pressure transducers (PCB Model 113A24) are positioned at different locations along the tube. Analysis of the time-dependant pressure traces measured using the linear array of transducers allowed the DDT distance to be assessed. Because of the complexity of multi-cycle detonation experiments, the goal of the study was, first, to concentrate on single-shot experiments and systematically measure (or at least estimate) the DDT distance for different operating parameters and initial conditions. Based on the results of the single-shot detonation studies, multi-cycle operation was then addressed.

For single-shot experiments, the far end of the initiator was sealed with a 2 μm thick mylar film and the tube was evacuated. When a vacuum level of one torr or less was achieved, the tube was filled with a premixed fuel/oxidizer explosive mixture at atmospheric pressure and

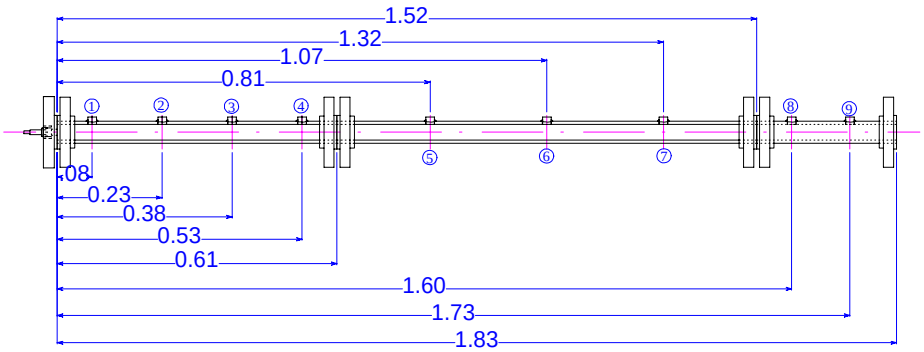

(a) Schematic of initiator tube (dimensions in meters)

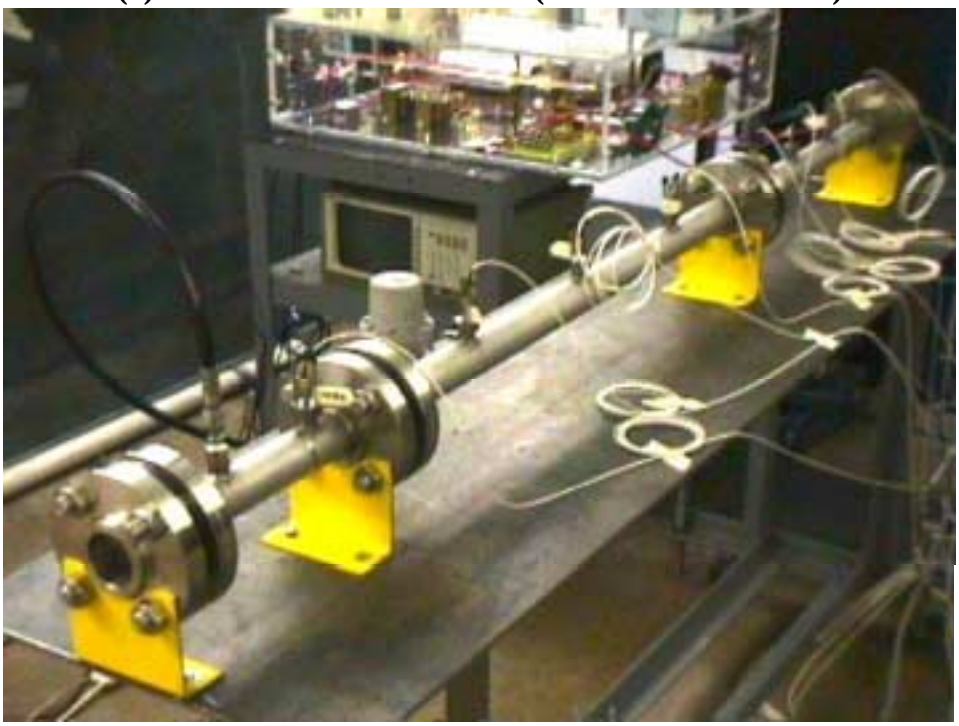

(b) Photograph of assembled initiator tube

Fig. 4.1. Circular cross-sectioned initiator configuration.

ignited at the closed end with an electric spark. The pressure transducers recorded the propagation of the combustion wave as it traveled down the tube. Upon reaching the end of the tube, the wave broke the mylar film and vented out of the laboratory through an exhaust duct.

For the multi-cycle studies where proper air and fuel mixing in the tube, both axially and radially, is necessary for successful detonations, the injector was designed accordingly. Based on the authors' extensive experience with rocket injectors, a multiple-element impinging jet

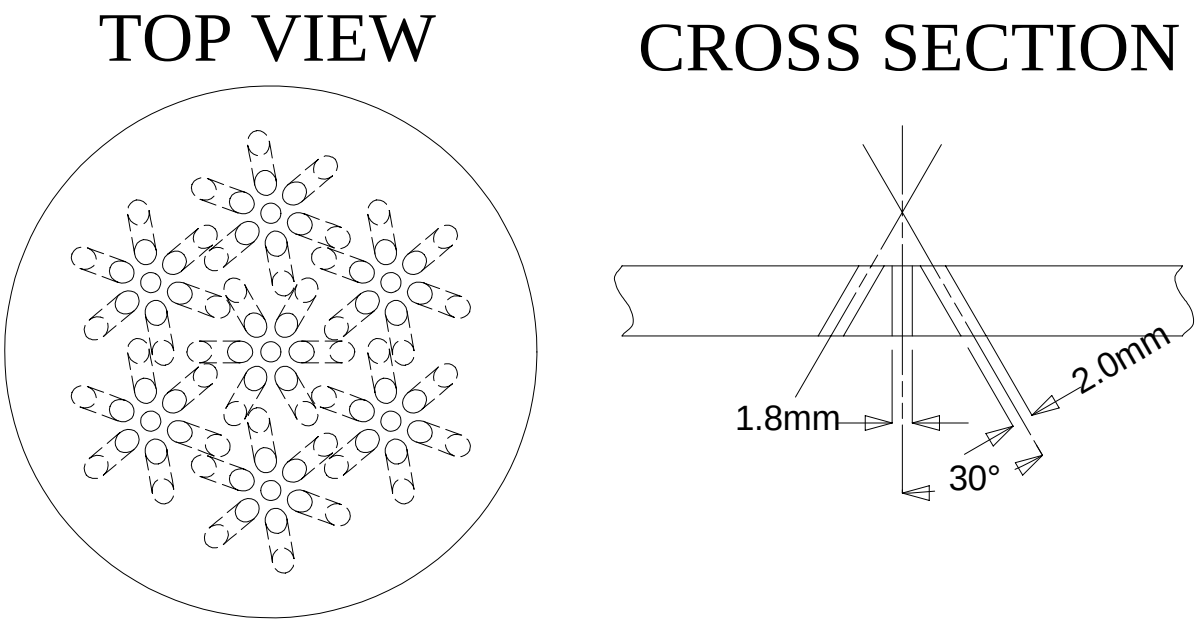

Fig. 4.2. Schematic of PDE impinging jets injector for multi-cycle operation.

injector was designed and fabricated. This low pressure-drop injector consists of seven impinging jet elements evenly distributed across the injector face, each of which consists of six air jets impinging on a central fuel jet (see Fig. 4.2). Finally, to deliver the proper flow rates of fuel and air into the initiator, two fast acting solenoid valves with a measured closing and opening response time of between 3 and 8 ms were used under choked conditions. After proper calibration, these valves were utilized to inject the desired amounts of fuel and air by adjusting the upstream pressure and the opening time of the valves.

4.1.1.2 Square Cross-sectioned Optically-accessible Initiator

The square cross-sectioned (44.5×44.5 mm (1.75×1.75 in.)) optically-accessible initiator is shown in Fig. 4.3. In the figure, both a schematic as well as photographs of the initiator are depicted. The initiator designed in a modular fashion, has four sections of varying length that can be assembled as desired. The optically-accessible section has a length of 254 mm

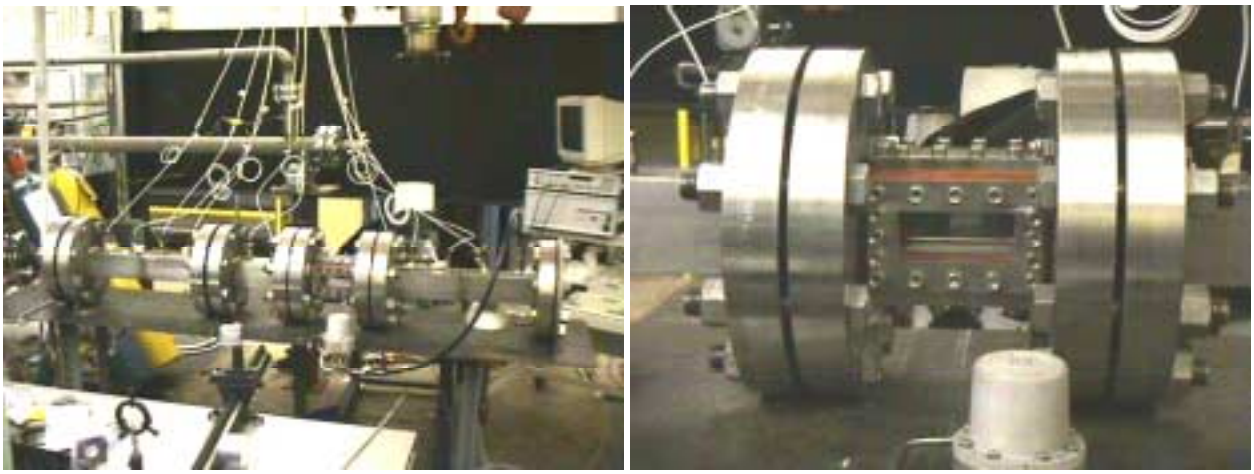

(a) Assembled initiator **(b) Closeup of window section**

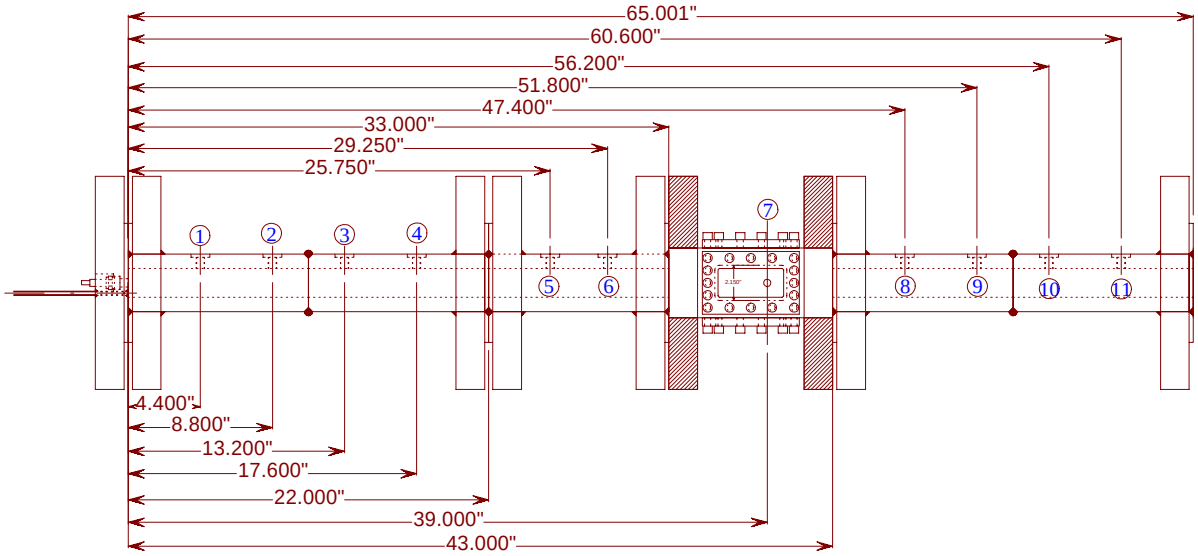

(c) Schematic of initiator

Fig. 4.3. Square cross-sectioned initiator configuration.

(10 in.), two straight sections are 559 mm (22 in.) long, and the remaining straight section has a length of 280 mm (11 in.). All four sections have 51 mm (2 in.) thick flanges at either end. With this modular design, the optically-accessible section can be positioned at various locations. The optically-accessible section has rectangular quartz windows on all four sides for application of laser-based diagnostics. This chamber will be mainly used for studying the fundamental aspects of detonation physics. Diagnostic techniques that will be employed for studying deflagration to detonation transitions and detonation propagation include Schlieren imaging,

Planar Laser Induced Fluoresence (PLIF) and Rayleigh scattering. Up to 11 high-speed, water-cooled pressure transducers (PCB Model 113A24) can be positioned at different locations along the length of the initiator. Analysis of the time-dependant pressure traces measured using the linear array of transducers allow the DDT distance to be assessed. The design and fabrication of this optically-accessible initiator was completed as part of the activities for the current delivery order. To date, only limited single-shot detonations have been attempted using this initiator.

4.1.1.3 Ignition System

Due to the well-documented difficulties in producing detonations with heavy HC/air mixtures [23], a powerful spark ignition system was built. This system was designed to deliver sparks of total energy E_T ~ 100 J on a single-shot basis and up to 20 J for multi-cycle operation at frequencies up to 50 Hz. By adjusting the charging voltage (from 2 to 15 kV) and the capacitor (1 μF or 0.1 μF), the spark energy can range over three orders of magnitude and its effect on DDT distance can also be studied.

4.1.1.4 Propellant Combination

Before starting the experiments, a fuel had to be selected that is representative of a typical hydrocarbon fuel, without being too difficult to detonate with air. Ethylene (C_2H_4) was selected as the candidate, since its detonation properties with oxygen and air are well documented in the literature [21,24,25] and it is a common decomposition component of large hydrocarbon species typical of liquid fuels. This report concentrates, therefore, on the results obtained with C_2H_4 as the fuel.

4.1.2 Results and Discussion

The first set of experiments attempted were for single-shot detonations. This set of experiments was first attempted for stoichiometric mixtures of ethylene/oxygen/nitrogen in the circular cross-sectioned initiator. The experimental results indicated that obstacle geometries, other than the classical Shchelkin spiral, were necessary for obtaining detonations in fuel/air mixtures. Under a separately-funded Office of Naval Research program, a sequence of experiments was conducted to optimize obstacle designs for obtaining stable detonations. Based on the results of these experiments, multi-cycle experiments were then conducted for the current program.

In the following, the results of single-shot experiments are briefly presented first, followed by a more detailed discussion of the multi-cycle experiments conducted for the current program.

4.1.2.1 Single-shot Detonations

Single-shot detonation experiments were conducted for stoichiometric mixtures of ethylene/oxygen diluted with increasing amounts of nitrogen [C_2H_4 + 3 (O_2+βN_2)] using the circular cross-sectioned initiator. A Shchelkin spiral with an optimal blockage ratio and pitch (48% and 32 mm, respectively) was placed in the first meter of the tube to help reduce DDT distances and a moderately strong spark (E_T = 3.5 J) was used for ignition. These initial experiments showed a clear but moderate increase in DDT distance, L_o, with nitrogen dilution factor, β, up to $\beta = 2$, beyond which level L_o increased abruptly. For $\beta > 2.83$, DDT was not achieved within the initiator, and the wave decayed in strength immediately after leaving the spiral. These results indicated that the Shchelkin spiral was not sufficient for inducing detonations with mixtures of ethylene/air. Therefore, the decision was made to improve on the

concept of the Shchelkin spiral and experiment with potentially better-suited obstacles. The Shchelkin spiral is believed to help reduce DDT distances by stretching the flame front and increasing the turbulence level of the flow during the deflagration phase, hence improving burning rates of the flame and increasing the mixing between burned products and fresh mixture immediately ahead [26,27]. This concept was improved through the use of obstacles aimed at producing even more disturbance in the flow, while minimizing blockage and losses. These obstacles were made out of a flat, 152 μm thick nickel alloy rectangular sheet. Protrusions in the shape of half disks (11.1 mm in diameter) were then punched through the sheet and bent perpendicular to the sheet to stick out 90° in the flow. The sheet was then carefully folded and inserted inside the initiator tube to fit snugly against the tube wall. Such an obstacle is shown in Fig. 4.4. Its pattern is such that, when folded inside the initiator, the half disk protrusions follow the same helicoidal path as the Shchelkin spiral, with the same pitch (32 mm).

In contrast to the Shchelkin spiral, this obstacle geometry (1 m long) yielded successful detonations for the same stoichiometric ethylene/air mixture and spark energy (E_T = 3.5 J). Several other obstacle geometries were then experimented upon to further optimize the design.

Fig. 4.4. Photograph of obstacle with half-disk protrusions.

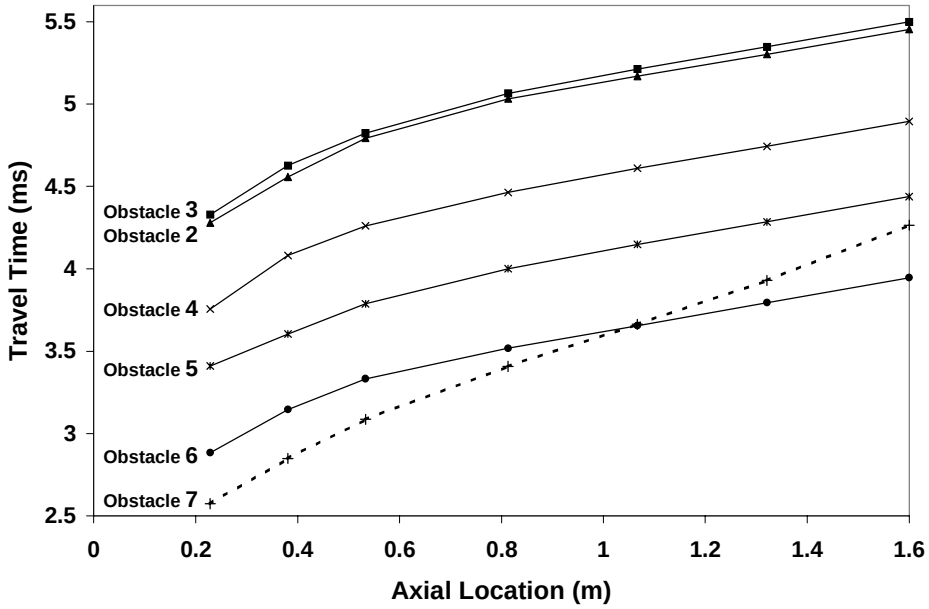

Fig. 4.5. Influence of obstacle size and configuration on travel time of combustion wave.

Representative experimental results are shown in Fig. 4.5. The results show that the DDT distances are fairly insensitive to the obstacles used. All measured DDT distances were about 0.6 m. This result may indicate that a certain amount of mixture must combust before creating conditions conducive to DDT, no matter what the size of protrusions in the flow, and the particular mechanisms leading to DDT.

4.1.2.2 Multi-cycle Operation

Having achieved single-shot detonations of C_2H_4/air mixtures in a controlled, repeatable fashion using the obstacles previously described, an investigation of multi-cycle operation of the initiator with a C_2H_4/air mixture was initiated. For these studies, the energy levels of the electric sparks used to initiate single-shot detonations ($E_T = 4 – 8$ J) were low enough to be used for multi-cycle detonations. The spark ignition system was successfully tested at frequencies up to 70 Hz without any particular problem. The choice of the proper obstacle geometry was also

instrumental for multi-cycle experiments. The single-shot results clearly indicated the benefit of large protrusions for enhancing the formation of detonations. However, these results need to be put in perspective when scaling up to practical PDE applications. The dynamic nature of multi-cycle operation, where gaseous fuel must be uniformly injected and mixed with air all along the initiator in a short time, may render the use of large protrusions in the flow very challenging. A solid obstacle made of half disks welded on a thin stainless steel frame basically resembling the obstacle geometry shown in Fig. 4.4 was adopted. The 7.9 and 5.5 mm high half disks presented a small enough blockage to the flow so as not to hinder the crucial dynamic injection process while already having been proven effective for inducing detonations of C_2H_4 and air within 0.6 m and acceptable DDT time delays. Furthermore, its rugged welded construction enabled it to withstand repeated detonations without failure.

For the C_2H_4/air mixture, successful multi-cycle operations were obtained at frequencies up to 8 - 10 Hz in the same 34 mm ID, 1.83 m long initiator. The number of detonations per sequence was limited to five to ten detonations due to safety concerns in case of misfirings as well as to limit any overheating of the uncooled tube and transducers. In general, most firings could be identified as detonations, with a velocity within a few percent of the CJ velocity and high pressure levels behind the detonation wave. In contrast to the single-shot results, multi-cycle operation had minimal effect on DDT distances, which were still around 0.6 m, but substantially reduced DDT times by 20 to 35%. It should be pointed out that certain firings within sequences above 5 to 8 Hz produced somewhat marginal behavior with detonation wave speeds 10 to 20% below CJ levels. These waves probably fit the description of quasi-detonations rather than fully developed CJ detonations. Fig. 4.6 represents a sequence of seven firings at 5 Hz. It is noted that the regularity of the firing sequence is not perfect, and that the time

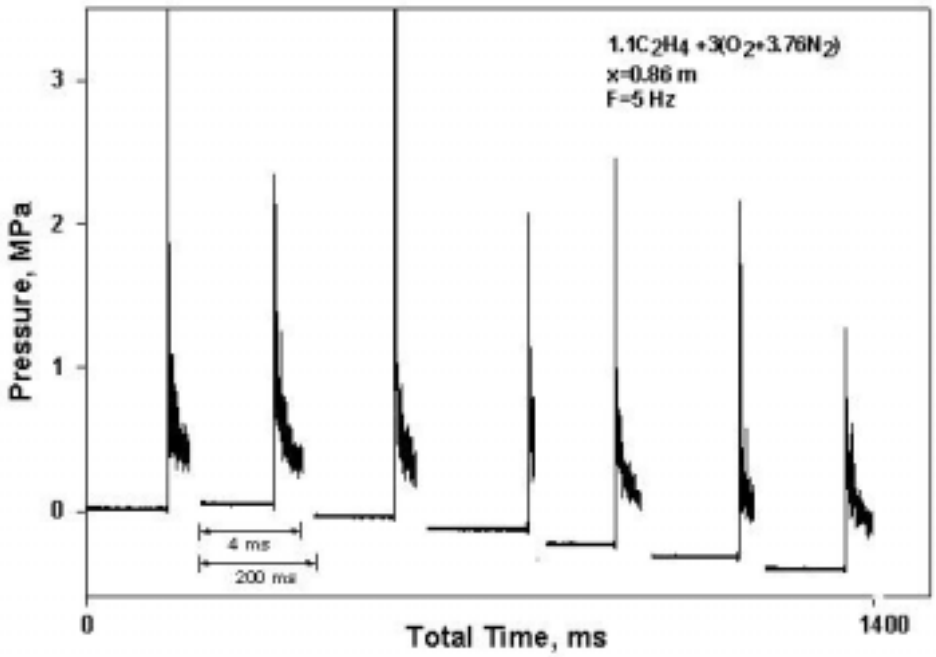

Fig. 4.6. Multi-cycle operation with ethylene/air at 5 Hz.

between two successive detonation/combustion waves and their pressure levels fluctuate slightly. Therefore, further refinements are needed for obtaining reliable and repeatable operation under multi-cycle conditions for fuel/air mixtures.

To avoid this problem and test the initiator at higher frequencies, oxygen-enriched air was used to make the mixture more sensitive to detonations. A premixed O_2+$2N_2$ oxidizer was used with ethylene. This new (easier) combination produced substantial improvements. All firings for any sequence were regular detonations propagating often all the way down the initiator, indicating excellent injection/mixing throughout the tube and correct timing conditions (see Fig. 4.7). Moreover, DDT distances were significantly reduced compared to runs with air and were observed to be between 0.15 and 0.3 m with travel times for the first 0.6 m within 1 ms. However, the gain in operating frequency was first minimal since misfirings suddenly appeared at frequencies above 15 – 20 Hz. In fact, these misfirings were due to very low supply pressures for the fuel solenoid valve, causing the valve to function erratically. After simple setup

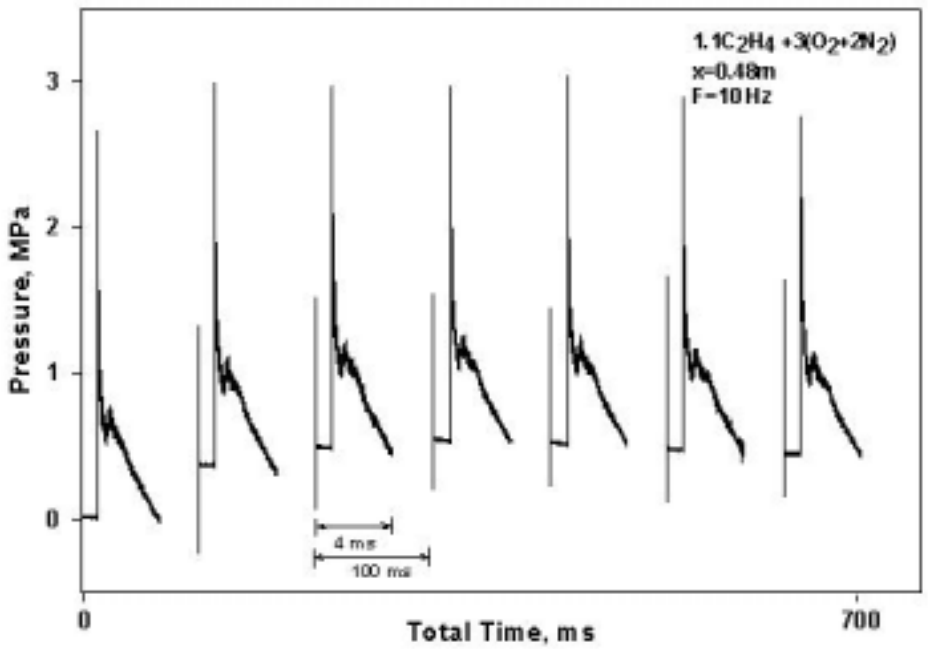

Fig. 4.7. Multi-cycle operation with ethylene/(O_2+2N_2) at 10 Hz.

modifications to increase the supply pressures (for the same fuel flowrates), successful detonations were achieved at frequencies up to 65 Hz. It is believed that these setup changes for the C_2H_4/air experiments would have provided similar high operational frequencies.

4.2 Numerical Modeling of Pulse Detonation Engine (PDE) Dynamics

Throughout this program, effort was expended in three areas. The first was the development of an innovative numerical scheme for chemically reacting flows based on the Space-Time Conservation Element and Solution Element method (the CE/SE method) [28,29]. A sub-time step technique [30] was designed to handle the stiff source terms arising from chemical reactions. The second was the development of a local mesh refinement technique [31] in the framework of the CE/SE method such that the spatial resolution of the detonation wave front can be greatly enhanced without much increase of the total computational load. The third

was the development of a one-dimensional code based on this new scheme to study detonation physics in a pulse detonation engine (PDE) environment [32,33]. The progress made in each of the above three areas is summerized below.

4.2.1 Extension of the CE/SE Method to Chemically Reacting Flows

Chemically reacting flows are much more difficult to simulate than their non-reacting counterparts. This mainly attributes to two reasons. First, the large number of species concentration equations are strongly coupled with the mass, momentum, and energy conservation equations, and consequently substantially increase the computational burden. Second, perhaps more importantly, reacting flows usually involve a wide range of length and time scales. The resultant eigenvalue disparity renders the solution scheme extremely stiff and much effort is required to circumvent the problem.

Existing methods for reacting flow simulations can be grouped into two categories. The first is the splitting method. In this method, the original governing equations are split into two sets. One represents pure hydrodynamics without consideration of chemical reaction source terms so that traditional numerical schemes, such as TVD schemes, can be directly employed to solve it. The other set treats motionless chemical reactions and thus can be solved by stiff ODE solvers. Since the two sets of equations are solved in an alternate way at every time step, the physical conservation laws become difficult to be enforced, often resulting in non-physical wave propagation, as described by LeVeque [34]. The second category attempts to directly tackle the entire system of governing equations. Although much effort has been devoted, so far very few schemes have successfully addressed the issues of numerical stability and accuracy. The main reason is that most of these schemes evolve from conventional schemes that were developed for

non-reacting flows. When directly extended to reacting flows, some underlying assumptions such as the monotonicity property in TVD schemes are no longer valid due to the presence of source terms, especially for problems involving discontinuities.

In view of the deficiencies of existing schemes, a new algorithm for reacting flows was developed based on the CE/SE method. The CE/SE method was originally developed for non-reacting flows. One of its unique features is the unified treatment of space and time so that the flux is kept strictly conservative locally and globally. When extending the CE/SE method to chemically reacting flows, the above feature was retained by integrating the original physical conservation laws over each space-time conservation element. The resultant equation set contains an integral of source terms over the corresponding conservation element. To proceed, a numerical model is required to estimate the integral. For systems involving fast chemical reactions, the hydrodynamic time scales may be several orders larger than the smallest chemical reaction time scales. Consequently, direct integration of source terms over the convection time step fails to resolve chemical processes. On the other hand, the computational time step can not be too small because it would lead to a very small CFL number, and subsequently large numerical dissipation. To overcome this difficulty, a sub-time step integration technique has been devised so that different time step sizes can be used for the hydrodynamic and chemical reaction parts.

4.2.2 Development of Local Mesh Refinement Technique

Numerical simulation of practical problems may require implementation of local mesh refinement (LMR) in regions of interest to accurately resolve some particular properties or characteristics (here mesh refinement implies refinement of both spatial mesh and time step).

For example, in a region where detonation wave or steep gradients are present, accurate resolution of these structures may exclude the use of a uniform coarse grid system. On the other hand, applying a very fine uniform grid system over the entire computational domain often is not practical because it may result in unacceptably high computing cost. In such a case, the use of LMR becomes a necessary alternative. This directly stimulated the development of an LMR technique in the framework of the CE/SE method. By taking advantage of several key features of the CE/SE method, the current LMR technique can easily enforce space-time flux conservation across the interface dividing the fine-grid region and the coarse-grid region, which is a critical design requirement to prevent numerical solutions from being contaminated by spurious reflections originated from that interface. Moreover, in the treatments of grid-to-grid communications, the current LMR procedure is much simpler and more efficient than the adaptive mesh refinement procedures described in [35,36]. In particular, no iterative procedure is used in the current treatments. Furthermore, numerical experiments on shock tube problems [31] showed that a refinement ratio up to 64:1 can be applied successfully across an interface using the current LMR procedure.

4.2.3 Numerical Study of Detonation Initiation Mechanism

Based on the above numerical scheme for chemically reacting flows, a one-dimensional code has been developed to study the detonation initiation and propagation mechanism. The formulation is based on the full conservation equations of the mass, momentum, energy, and species concentrations, with detailed chemical kinetics considered. The sample chemical system was the stoichiometric hydrogen/oxygen mixture. The chemical kinetics scheme involves eight species (H_2, O_2, OH, H_2O, H, O, HO_2, and H_2O_2) and twenty-four elementary reactions. The 1-D

tube used in the numerical experiments measured a length of 20 cm, with the head end closed and the downstream end open. Two grid systems were used in all the numerical calculations, each of which had a uniform mesh size. A coarse grid with a mesh size of 0.01 cm was applied to the entire tube, and remained fixed during time marching. A fine grid, on the other hand, only covered a very small region around the detonation wave front and moved with the detonation wave. Its mesh size was determined by the refinement ratio R that was an input.

Two initiation methods were explored: shock and hotspot initiation. In the shock initiation method, a driver section with the length of 0.2 cm was placed near the head end of the tube. The species mass fractions in that section were determined using the CEC code [37] based on the prespecified temperature and pressure. The remaining part of the tube was the driven section filled with the stoichiometric H_2/O_2 mixture at 1 atm and 300 K. The effect of the driver strength on the detonation initiation and propagation was then studied by changing high pressure and temperature in the driver section. In all the cases studied here, the grid refinement ratio R was fixed to be 4. The results are summarized in Table 4.1.

Numerical results show that the onset of detonation is greatly dependent on the driver temperature, while the role of the driver pressure is minimal. Detonation can easily be triggered under high driver temperatures, provided the driver pressure is larger than the environment pressure. Moreover, for cases having the same driver temperature but different pressure, the corresponding time histories of pressure and temperature are similar. Figs. 4.8-4.10 show the

Table 4.1. Effect of Driver Strength on Detonation Initiation (Shock Initiation Case).

p_{driver} (atm)	Onset of Detonation (T_{driver}= 3000 K)	Onset of Detonation (T_{driver}= 2500 K)	Onset of Detonation (T_{driver}= 2000 K)
30	Y	Y	N
20	Y	Y	N
10	Y	Y	N
5	Y	Y	—
1	N	—	—

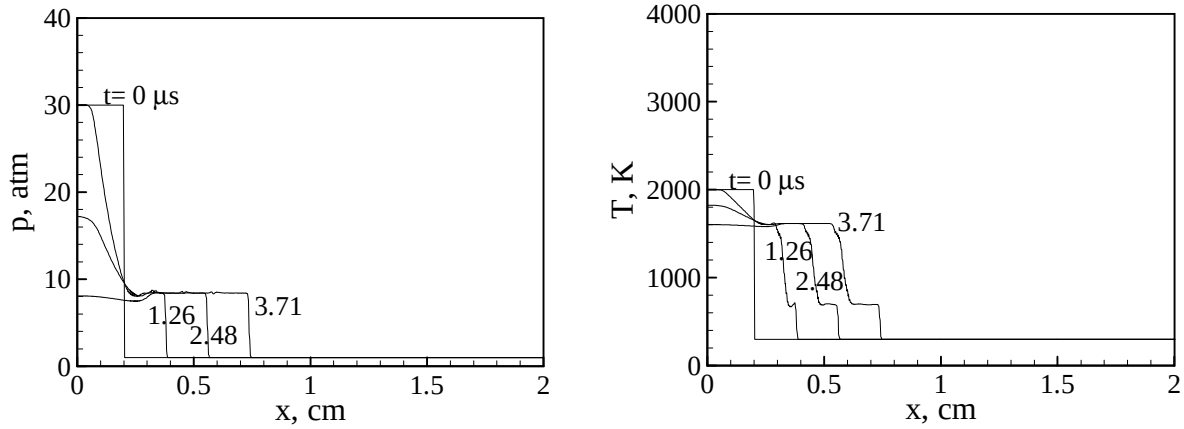

Fig. 4.8. Time evolution of pressure and temperature for shock initiation case; p_{driver} = 30 atm and T_{driver} = 2000 K.

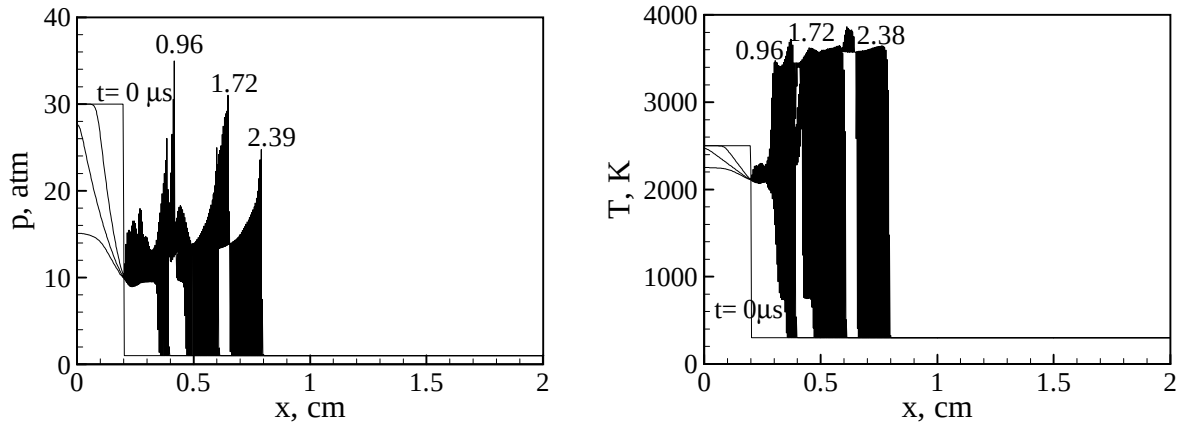

Fig. 4.9. Time evolution of pressure and temperature for shock initiation case; p_{driver} = 30 atm and T_{driver} = 2500 K.

time histories of pressure and temperature in the early stage for the cases of p_{driver} = 30 atm and T_{driver}= 2000 K, 2500 K, and 3000 K, respectively. The third case exhibited a well-developed detonation wave in the later stage, as shown in Fig. 4.11. Table 4.2 compares the detonation properties obtained from the present simulation and the NASA CEC code. The accuracy of the numerical scheme is established in terms of steady detonation propagation.

For the hotspot initiation method, two different initial temperature distributions were tested. The first one has a linear temperature distribution as follows.

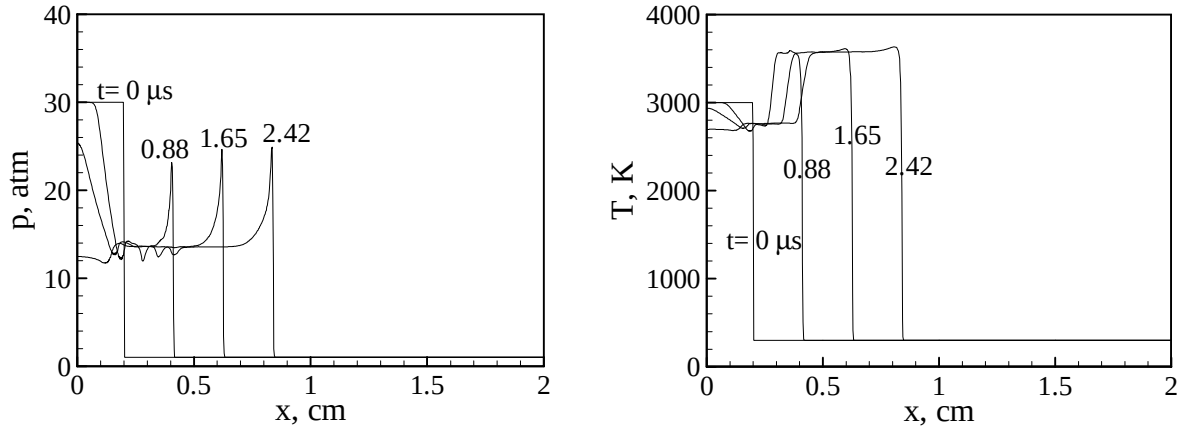

Fig. 4.10. Time evolution of pressure and temperature for shock initiation case; p_{driver} = 30 atm and T_{driver} = 3000 K.

$$T = \begin{cases} T_{I0}\,(1-\xi\,x), & 0 \le x \le L_I \\ T_0, & L_I \le x \le L_0 \end{cases} \qquad (4.1)$$
$$\xi = (1-T_0/T_{I0})/L_I$$

where L_I, and L_0 are the lengths of the hotspot and computational domain, respectively. T_{I0} and T_0 are, respectively, the maximum and environment temperatures. The second one has a stepwise temperature distribution as follows.

$$T = \begin{cases} T_{I0}, & 0 \le x \le L_I \\ T_0, & L_I \le x \le L_0 \end{cases} \qquad (4.2)$$

In all the cases studied here, the initial pressure was set to be uniform at 1 atm throughout the chamber which was filled up with a stoichiometric H_2/O_2 mixture. The coarse grid size was 0.01cm. The grid refinement ratio R was 2 for the case of the linear temperature distribution and 4 for the case of the stepwise temperature distribution. Figs. 4.12 and 4.13 show the time

Table 4.2. Comparison of Detonation Wave Properties (Shock Initiation Case: p_{driver} = 30 atm and T_{driver} = 3000 K).

	Detonation Velocity, m/s	Y(H_2)	Y(O_2)	Y(OH)	Y(H_2O)
NASA CEC	2837	0.0226	0.1067	0.1579	0.6644
present	2812	0.0222	0.1047	0.1561	0.6452
difference	0.88%	1.77%	1.87%	1.08%	2.86%

evolution of temperature and pressure for the linear temperature distribution case with the parameters of L_I = 1.65 cm, L_0 = 20 cm, T_{I0} = 1350 K, and T_0 = 450 K. Fig. 4.14 shows the snapshot of pressure and temperature at 76.0 μs for the same case. The effect of the initial temperature gradient was also studied by reducing the size of the hotspot from L_I = 1.65 to 1.0 cm with the other parameters unchanged. The corresponding time evolution of pressure and temperature is shown in Fig. 4.15. Although the onset of detonation also took place in this case, the initiation process took a longer time than the previous case. Figs. 4.16 and 4.17 show a typical time evolution of temperature and pressure for the case with a stepwise initial temperature distribution (i.e., L_I = 1.5 cm, L_0 = 20 cm, T_{I0} = 1000 K, and T_0 = 450 K). The same

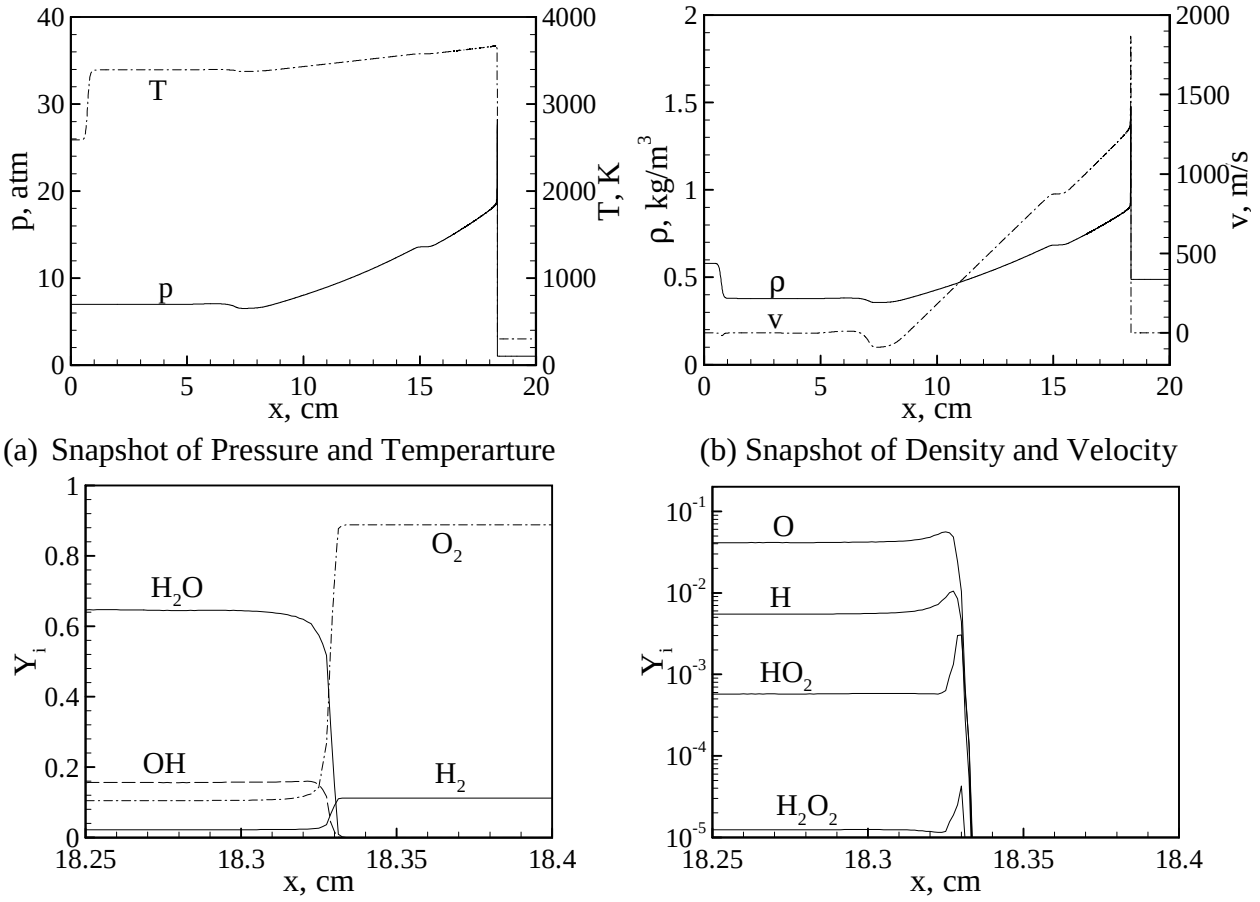

(a) Snapshot of Pressure and Temperarture

(b) Snapshot of Density and Velocity

(c) Snapshot of Species Mass

Fig. 4.11. Snapshot of properties at 64.5 μs for shock initiation case; p_{driver} = 30 atm and T_{driver} = 3000 K.

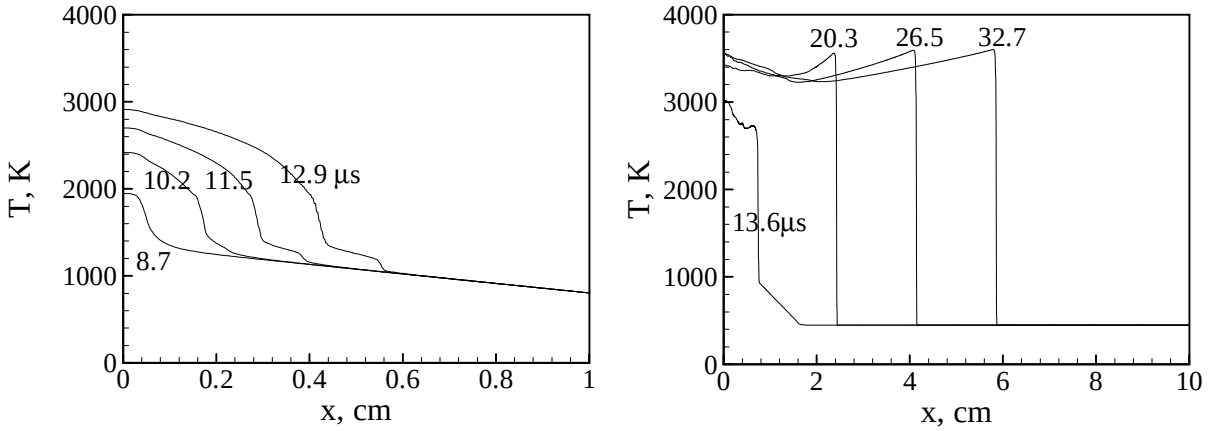

Fig. 4.12. Time evolution of temperature for hotspot initiation case with linear temperature distribution; L_I = 1.65 cm, L_0 = 20 cm, T_{I0} = 1350 K, and T_0 = 450 K, and p = 1 atm.

hotspot was also used to initiate detonation with an environment temperature T_0 = 300 K to study the initiation energy requirement. Figs. 4.18 and 4.19 are the time evolution of temperature and pressure for this case. Comparison of these two cases shows that more time was needed to initiate detonation in a mixture having a lower temperature. When the detonation initiation mechanism is of concern, the above studies show that the deflagration-to-detonation mechanism is responsible for detonation initiation for a linear temperature distribution. In contrast, due to the simultaneous auto-explosion in the high temperature region, detonation can be directly initiated with a stepwise temperature distribution.

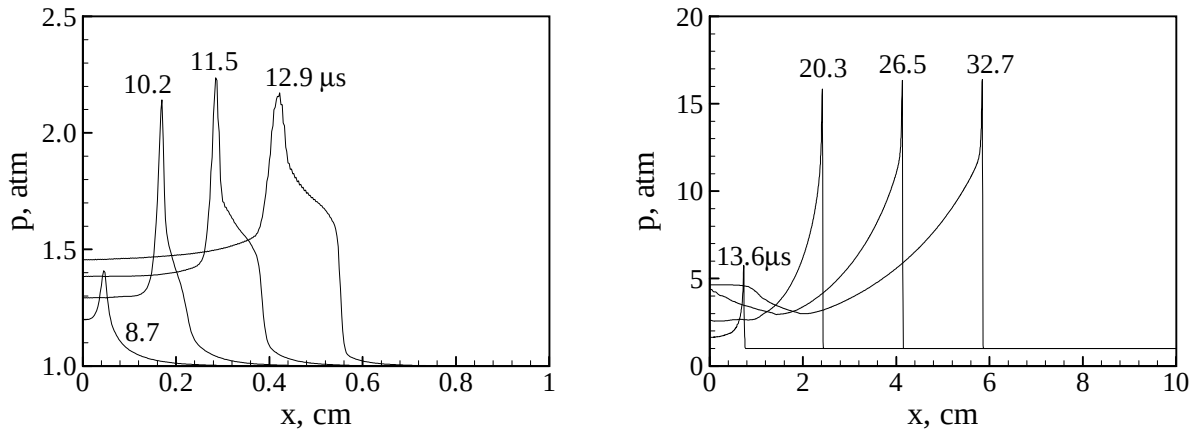

Fig. 4.13. Time evolution of pressure for hotspot initiation case with linear temperature distribution; L_I = 1.65 cm, L_0 = 20 cm, T_{I0} = 1350 K, and T_0 = 450 K, and p=1 atm.

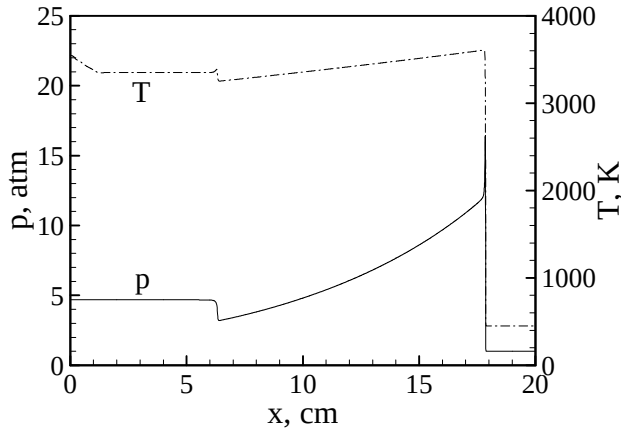

Fig. 4.14. Snapshot of pressure and temperature at 76.0 μs for hotspot initiation case with linear temperature distribution; L_I = 1.65 cm, L_0 = 20 cm, T_{I0} = 1350 K, T_0 = 450 K, and p = 1 atm.

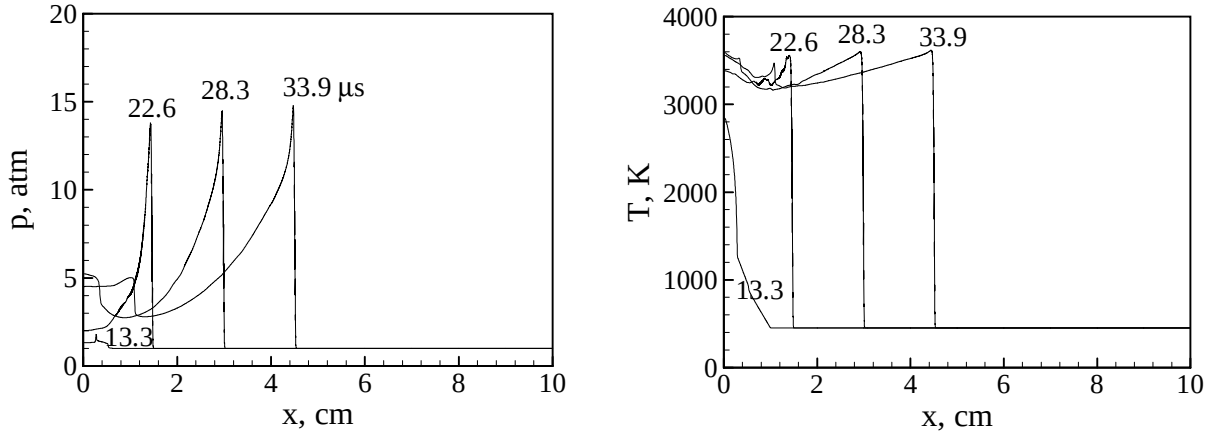

Fig. 4.15. Time evolution of pressure and temperature for hotspot initiation case with linear temperature distribution; L_I = 1.0 cm, L_0 = 20 cm, T_{I0} = 1350 K, T_0 = 450 K, and p = 1 atm.

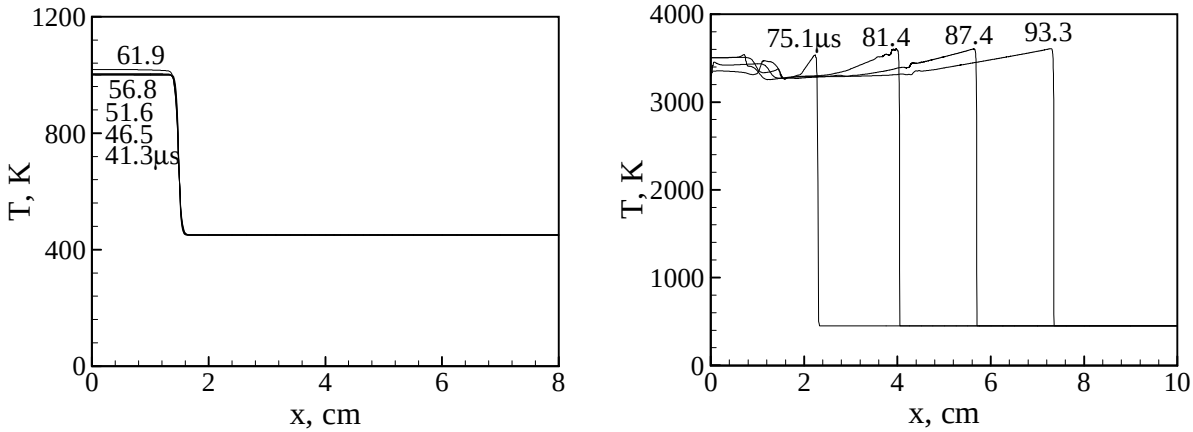

Fig. 4.16. Time evolution of temperature for hotspot initiation case with stepwise temperature distribution; L_I = 1.5 cm, L_0 = 20 cm, T_{I0} = 1350 K, T_0 = 450 K, and p=1 atm.

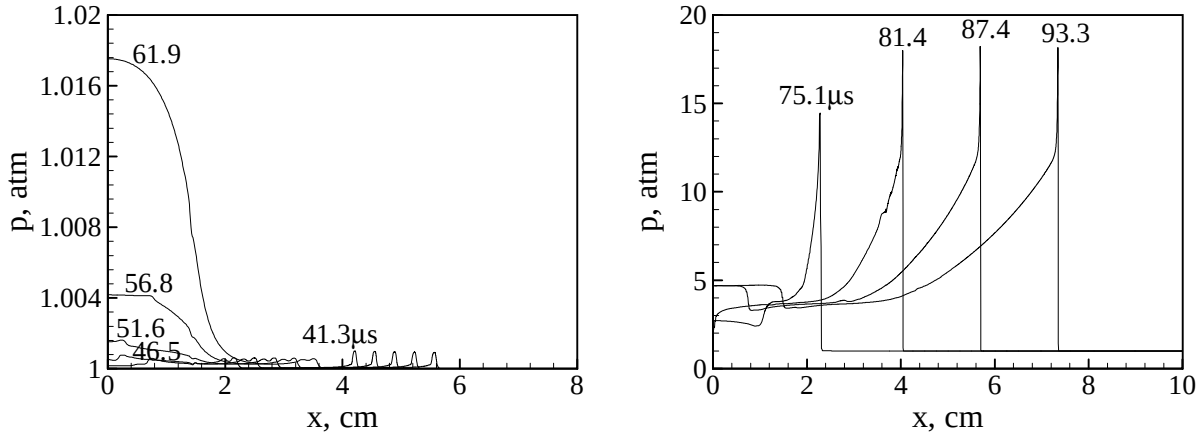

Fig. 4.17. Time evolution of pressure for hotspot initiation case with stepwise temperature distribution; L_I = 1.5 cm, L_0 = 20 cm, T_{I0} = 1350 K, T_0 = 450 K, and p=1 atm.

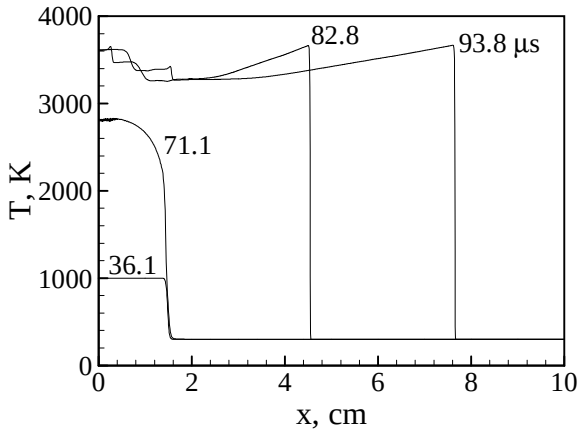

Fig. 4.18. Time evolution of temperature for hotspot initiation case with stepwise temperature distribution; L_I = 1.5 cm, L_0 = 20 cm, T_{I0} = 1350 K, T_0 =300 K, and p=1 atm.

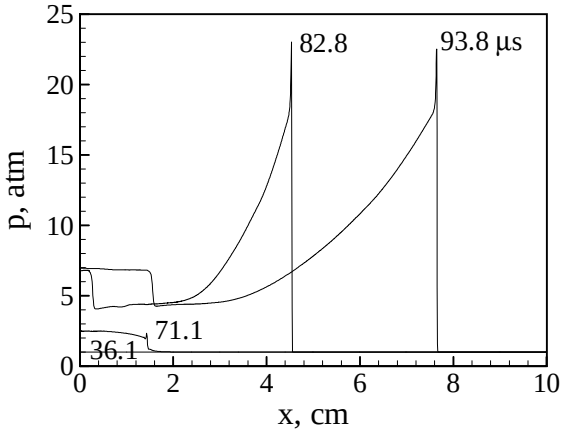

Fig. 4.19. Time evolution of pressure for hotspot initiation case with stepwise temperature distribution; L_I = 1.5 cm, L_0 = 20 cm, T_{I0} = 1350 K, T_0 = 300 K, and p=1 atm.

V Coal Derived Fuel Combustion Studies of an Advanced Gas Turbine Engine Fuel System (Task 4)

This task (Task 4) was subcontracted to Innovative Scientific Solutions Incorporated (ISSI). Their final report **TITLED COAL-DERIVED-FUEL COMBUSTION STUDIES OF AN ADVANCED-GAS-TURBINE FUEL SYSTEM** under subcontract USAF-TPSU-ISSI-2802-1482 is included in this report as an appendix.

VI References

[1] Yu, J. and Eser, S., "Determination of Critical Properties (T_c, P_c) of Some Jet Fuels," *Ind. Eng. Chem. Res.*, Vol. 34, 1995, pp. 404-409.

[2] Lefebvre, A. H., *ASME J. Eng. Gas Turbines Power,* Vol. 11, 1995, pp. 617-654.

[3] Broda, J. C., Seo, S., Santoro, R. J., Shirhattikar, G., and Yang, V., "An Experimental Study of Combustion Dynamics of a Premixed Swirl Injector," *Twenty-Seventh Symposium (International) on Combustion*, The Combustion Institute, Pittsburgh, PA 1998, pp. 1849-1856.

[4] Seo, S., "Parametric Study of Lean Premixed Combustion Instability in Pressurized Model Gas Turbine Combustor", PhD. Thesis, May 1999.

[5] Straub, D. L. and Richards, G. A., "Effect of Nozzle Configuration on Premix Combustion Dynamics," ASME Paper 98-GT-492, 1998.

[6] Lieuwen, T. and Zinn, B. T., "The Role of Equivalence Ratio Oscillations in Driving Combustion Instabilities in Low NO_x Gas Turbines," *Twenty-Seventh Symposium (International) on Combustion*, The Combustion Institute, Pittsburgh, PA 1998, pp. 1809-1816.

[7] Shih, W-P., Lee, J. G. and Santavicca, D. A., " Stability and Emissions Characteristics of a Lean Premixed Gas Turbine Combustor," *Twenty-Sixth Symposium (International) on Combustion*, The Combustion Institute, Pittsburgh, PA, 1996, pp. 2771-2778.

[8] Janus, M. C., Richards, G. A., and Yip, M. J., "Effects of Ambient Conditions and Fuel Composition Stability," ASME Paper 97-GT-266, 1997.

[9] Germano, M. Piomelli, U., Moin, P., and Cabot, W., "A Dynamic Subgrid-Scale Eddy Viscosity Model," *Phys. Fluids* A, Vol. 3, No. 7, 1991, pp. 1760-1765.

[10] Moin, P., Squires, W., Cabot, W., and Lee, S., "A Dynamic Subgrid-Scale Model for Compressible Turbulence and Scalar Transport," *Phys. Fluids* A, Vol. 3, No. 11, 1991, pp. 2746-2757.

[11] Zong, X., "Additive Semi-Implicit Runge-Kutta Method for Computing High-Speed Nonequilibrium Reactive Flows," *Journal of Computational Physics*, Vol. 128, 1996, pp. 19-31.

[12] Nejad, A., Favaloro, S. C., Vanka, S. P., Samimy, M., and Langenfeld, C., "Application of Laser Velocimetry for Characterization of Confined Swirling Flow," *Journal of Engineering for Gas Turbines and Power,* Vol. III, No. 1, 1989, pp. 36-45.

[13] Rayleigh, J. W. S., *The Theory of Sound*, Vol. II, Dover, New York, 1945.

[14] Pratt, D. T, Humphrey, J. W. and Glenn, D. E., "Morphology of Standing Oblique Detonation Waves", *Journal of Propulsion and Power*, Vol. 7, 1991, pp. 837-845.

[15] Bratkovich, T. E. and Bussing, T. R. A., "A Pulse Detonation Engine Performance Model", AIAA Paper 95-3155, 1995.

[16] Kailasanath, K., "Applications of Detonations to Propulsion: a Review", AIAA Paper 99-1067, 1999.

[17] Helman, D., Shreeve, R. P. and Eidelman, S., "Detonation Pulse Engine", AIAA Paper 86-1683, 1986.

[18] Bussing, T. R. A., Hinkey, J. B. and Kaye, L., "Pulse Detonation Engine Preliminary Design Considerations", AIAA Paper 94-3220, 1994.

[19] Lee, J.H.S., "On the Transition from Deflagration to Detonation", *Prog. Astro. and Aero.*, Vol. 106, 1986, pp. 3-18.

[20] Dupre, G., Knystautas, R. and Lee, J. H., "Near-Limit Propagation of Detonation in Tubes", *AIAA Journal*, 1986, pp. 244-259.

[21] Knystautas, R., Guirao, C., Lee, J. H. and Sulmistras, A., “Measurements of Cell Size in Hydrocarbon-Air Mixtures and Predictions of Critical Tube Diameter, Critical Initiation Energy, and Detonability Limits”, *AIAA Journal*, 1984, pp. 23-37.

[22] Tieszen, S. R., Stamps, D. W., Westbrook, C. K. and Pitz, W. J., “Gaseous Hydrocarbon-Air Detonations”, *Combustion and Flame*, Vol. 84, 1991, pp. 1376-390

[23] Benedick, W. B., Guirao, C. M., Knystautas, R and Lee, J. H., “Critical Charge for the Direct Initiation of Detonation in Gaseous Fuel-Air Mixtures”, *Prog. Astro. and Aero.*, Vol. 106, 1986, pp. 181-202.

[24] Bull, D. C., Elsworth, J. E. and Shuff, P. J., “Detonation Cell Structures in Fuel/Air Mixtures”, *Combustion and Flame*, Vol. 45, 1982, pp. 7-22.

[25] Westbrook, C. K. and Urtiew, P. A., “Chemical Kinetic Prediction of Critical Parameters in Gaseous Detonations”, *Nineteenth Symposium (Int’l) on Combustion*, The Combustion Institute, Pittsburgh, PA, 1982, pp. 615-623.

[26] Urtiew, P. A. and Oppenheim, A. K., “Experimental Observations of the Transition to Detonation in an Explosive Gas”, *Proc. of the Roy. Soc. London*, Vol. A295, 1966, pp. 13-28.

[27] Lee, J. H. S. and Moen, I. O., “The Mechanism of Transition From Deflagration to Detonation in Vapor Cloud Explosions”, *Prog. Energy Combust. Sci.*, Vol. 6, 1980, pp. 359-389.

[28] Chang, S.C., "The Method of Space-Time Conservation Element and Solution Element — A New Approach for Solving the Navier-Stokes and Euler Equations," *J. Comput. Phys*., Vol. 119, 1995, pp. 295-324.

[29] Chang, S.C., Wang, X.Y., and Chow, C.Y., "The Space-Time Conservation Element and Solution Element: A New High Resolution and Genuinely Multidimensional Paradigm for Solving Conservation Laws," *J. Comput. Phys*., Vol. 156, 1999, pp. 89-136.

[30] Wu. Y., Yang, V., and Hsieh, K.C., "Simulation of Unsteady Premixed Flames with Detailed Chemical Kinetics Using the Space-Time Method," AIAA 99-1010.

[31] Chang, S.C., Wu, Y., Wang, X.Y., and Yang, V., "Local Mesh Refinement in the Space-Time Conservation Element and Solution Element Method," *the First International Conference on Computational Fluid Dynamics (ICCFD),* Kyoto, Japan, July 10-14, 2000.

[32] Wu. Y., Yang, V., and Chang, S.C., "Numerical Simulation of Detonation with Detailed Chemical Kinetics Using the Space-Time Method," AIAA 2000-0317.

[33] Wu. Y., Yang, V., and Chang, S.C., " Numerical Simulation of Chemically Reacting Flows with Detailed Chemical Kinetics Using the Space-Time Method," *the First International Conference on Computational Fluid Dynamics (ICCFD),* Kyoto, Japan, July 10-14, 2000.

[34] LeVeque, R.J., and Yee, H.C., "A Study of Numerical Methods for Hyperbolic Conservation Laws with Stiff Source Terms," *J. Comput. Phys.*, Vol. 86, 1990, pp. 187-210.

[35] Berger, M.J., "Local Adaptive Mesh Refinement for Shock Hydrodynamics," *J. Comput. Phys.,* Vol. 82, 1989, pp. 64-84.

[36] Berger, M.J., and LeVeque R.J., "Adaptive Mesh Refinement using Wave-Propagation Algorithms for Hyperbolic Systems," *SIAM J. Numer. Anal.,* Vol. 35, 1998, pp. 2298-2316.

[37] McBride, B.J. and Gordon, S., "Computer Program for Calculation of Complex Chemical Equilibrium Compositions and Applications", NASA Reference Publication 1311, June 1996.

Appendix

ISSI Report on Coal-derived-fuel Combustion Studies

ISSI Innovative Scientific Solutions, Incorporated
2766 Indian Ripple Rd. • Dayton, OH 45440-3638
937• 252 • 2706

COAL-DERIVED-FUEL COMBUSTION STUDIES OF AN ADVANCED-GAS-TURBINE FUEL SYSTEM

FINAL REPORT
SUBCONTRACT USAF-TPSU-ISSI-2802-1482

22 MAY 1998 - 31 JANUARY 1999

Coal-Derived-Fuel Combustion Studies of an Advanced-Gas-Turbine Fuel System

Final Report
Subcontract No. USAF-TPSU-ISSI-2802-1482
22 May 1998 – 31 January 1999

Prepared for:

Harold H. Schobert, Ph.D.
Project Director
The Pennsylvania State University
209 Academic Project Buiding
University Park, PA 16802-7000

1 March 1999

Prepared by:

Geoffrey J. Sturgess, Ph.D.
Innovative Scientific Solutions, Inc.
2766 Indian Ripple Road
Dayton, OH 45440-3638

Table of Contents

List of Illustrations

TASK 1: DESIGN OF ADVANCED-TURBINE-ENGINE FUEL SYSTEM

Introduction

Fuel systems in advanced-aircraft gas-turbine engines for military (fighter/bomber) applications are subject to a considerable heat load on the fuel from the aircraft systems. A further heat load may result from the use of endothermic fuels or turbo-cooling to reduce turbine-cooling airflow requirements through lowered cooling-air temperatures. Therefore, for realistic evaluation of the combustion characteristics of a coal-derived fuel, it is essential that the fuel be delivered to a test combustor in a state that is representative of the intended service use. For this reason the combustion test facility to be used must include an adequate simulation of such an advanced gas-turbine-engine fuel system.

Simulated Fuel System

The major elements of the simulated fuel system are represented schematically in Figure 1. The fuel pumps increase the fuel temperature as they raise its pressure. The liquid-fuel pressure entering the fuel heater is either subcritical or supercritical, depending upon the desired operating conditions. The fuel heater adds heat to the fuel stream to simulate heat rejection from the aircraft electronic and environmental systems to the fuel. The heated fuel enters the fuel/air heat exchanger that simulates heat rejected to the fuel from the air to be used in turbine cooling. Alternatively, the fuel/air heat exchanger may also have catalytically reactive passages in the fuel side for producing an endothermically cracked fuel, thereby enhancing the cooling-air temperature reduction.

The conditions of the fuel in the fuel lines of the simulated system shown in Figure 1 are such that spontaneous fires in the event of fuel leaks are a major concern. These concerns are exacerbated by the presence in the test cell of hot-surface ignition sources provided by the combustor rig and exhaust system, together with potential bluff-body flameholders presented by the many air, fuel, instrumentation, and service lines present in the facility.

Safety Hazards

In the test cell of Room 20, Building 18, of the Air Force Research Laboratory (AFRL), the proposed use of a high-pressure fuel-system simulation with a coal-derived JP-900 fuel for an advanced gas-turbine engine that employs supercritical and endothermic fuel conditions, therefore, posed serious concerns related to potential safety issues--particularly, open fires and explosion hazards. Two specific issues were of concern: 1) provision of adequate facility ventilation to avoid accumulation of jet-fuel vapors in concentrations sufficient to pose an explosion hazard, and 2) auto-ignition/open-flame potential of a fuel/air plume formed from a leak.

For the present purposes a "leak" is defined as a small hole or crack in a fuel line or system component that results in a significant leak mass flow rate compared to the total fuel flow rate supplied to the combustion rig. A leak of this kind is encountered during operation of the facility. Weeping of fuel from seals, fittings, and flanges is not

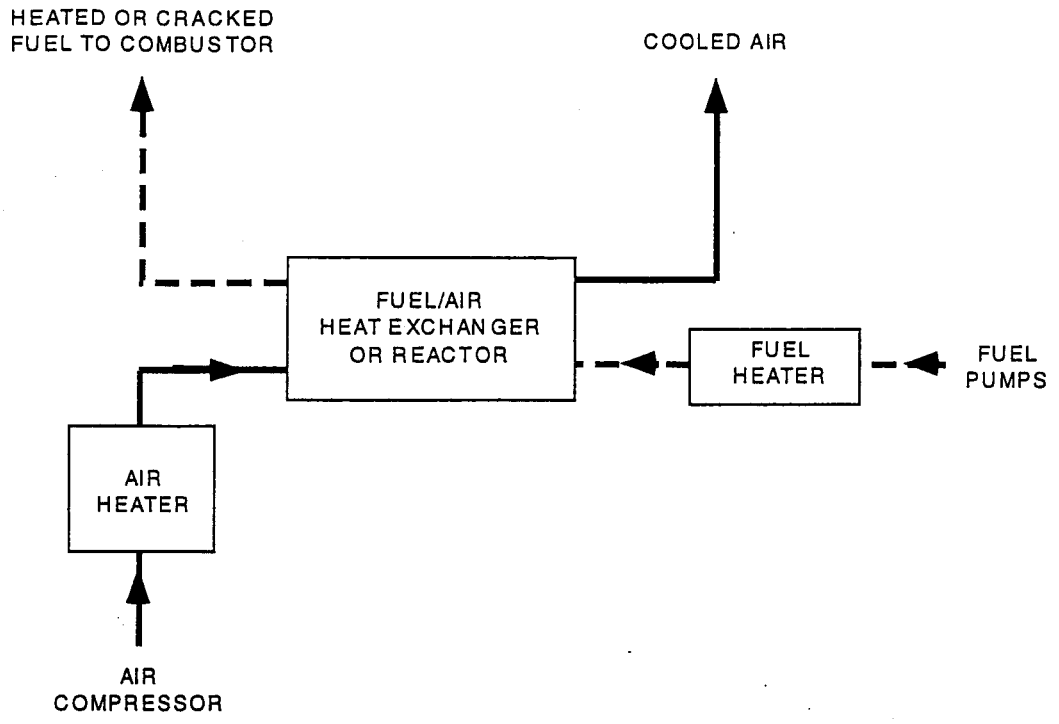

Figure 1. Schematic of Simulated-Fuel-System Major Elements.

considered since a sustained and significant leak mass flow rate does not normally result from such causes. Weeping can be present at all times and is considered to be a normal maintenance item.

The two issues mentioned above are strongly influenced by the location of the hypothetical fuel leaks in the simulated fuel system. First, consider the explosion hazard. If a leak forms downstream of the fuel pump and fuel heater but upstream of the catalytic reactor (endothermic system) or the turbo-cooler in the fuel system (with reference to Fig. 1), the fuel temperature in the line will be high in relation to the fuel flash point but will be well below the fuel critical temperature. The leaking-fuel temperature will fall as expansion takes place through the leak-source under the pressure drop across the fuel-line wall. Depending on the size of the leak, this pressure drop may be substantial. A substantial pressure drop would result in the creation of a spray of liquid drops. Secondary atomization may also occur from any solid objects on which the spray, or fuel stream, might impinge. Droplet evaporation will take place within the spray; pool evaporation will subsequently take place from solid objects that are impinged upon. Local concentrations of fuel vapor in the facility air will, therefore, be controlled by the net evaporation process and by spreading of the resulting vapor cloud.

If this leak occurs at or above the fuel critical pressure and critical temperature, i.e., downstream of the fuel/air turbo-heat exchanger, immediate flash evaporation of the leaked fuel will take place. Some subsequent cooling due to expansion could result in minor condensation of liquid fuel in the vapor plume. However, condensed fuel will exist as extremely small droplets that can be reasonably considered as a vapor. Therefore, local concentrations of fuel vapor in the facility air will be controlled by the leak rate and by spreading of the resulting fuel-vapor cloud.

The leak, if it occurs downstream of the catalytic reactor (endothermic-fuel case), will consist of gaseous-phase lower hydrocarbons and hydrogen. Local compositions and concentrations of cracked-fuel components in the facility air will be controlled by the leak rate and vapor-species mass transport.

Despite its origin, a spreading fuel-vapor cloud will eventually produce fuel vapor/air concentrations in the range of the lower explosive limit. If such a vapor cloud then envelopes a suitable hot-surface ignition source, an explosion will probably result.

For the second case--a plume fire originating at or near the leak source--despite the position of the leak and the leaking-fuel thermodynamic state, stoichiometric fuel vapor/air mixtures will form at some position in the unignited plume. Ignition delay times for premixed fuel/air mixtures are known to reach a minimum for such stoichiometric mixtures. If the stoichiometric condition is attained before the plume has cooled sufficiently, autoignition can occur. This is particularly likely for cracked-fuel products containing a few percent of hydrogen. Alternatively, if the position in the plume at which the stoichiometric mixture is reached is exposed to an adequate ignition source (a sufficiently hot surface), flame will result. If the local plume velocity in the neighborhood of flame initiation is at or below the turbulent burning velocity for the fuel/air mixture, a flame will be stabilized and sustained. This usually occurs if the ignited plume is also subject to a bluff-body wake flow of some kind as a result of the plume traversing a solid-object obstruction.

A stabilized open-jet flame may do local damage (which may then lead to cumulative failures), but it will reduce or eliminate the explosion hazard by consuming most of the fuel vapor being produced.

Estimation of Ventilation Requirements

The explosion hazard is addressed by providing sufficient space ventilation with diluent fresh air to prevent local concentrations of fuel vapor from reaching the explosion limit. The lower explosive limit (LEL) for jet-fuel vapor/air mixtures at room temperature is 0.6% by volume of vapor in air,[1] which is slightly below the lower flammability limit of vaporized kerosene in air at room temperature--0.7% by volume.[2] Several procedures are available for calculating the necessary ventilation; unfortunately, different procedures can result in large differences in ventilation airflow. Coupled with the ASTM allowable ranges in jet-fuel physical properties and the range of leak assumptions possible, the uncertainties can become very large. Therefore, it is common practice to use average fuel properties with worst-case leak assumptions and then apply generous safety factors to the calculations. Finally, the procedure that yields answers nearest to known safe experience is selected. This is clearly not a particularly satisfactory way of proceeding since it can lead to one of two possibilities: 1) excessive ventilation air, or 2) marginal ventilation air for circumstances peculiar to the particular installation. The former can be prohibitively expensive and the latter, inherently dangerous.

The first approach considered is one based on known safe experience. In this case, one based on an earlier installation at AFRL is used. Room 22, Building 18E, of AFRL was designed by the Osborn Engineering Company to accommodate a hydrogen combustion

facility. For normal operations the requirement of five complete room volume changes per hour was established, with an emergency condition of 20 changes per hour. Since hydrogen is lighter than air and has a high diffusion coefficient, use of the total room volume is appropriate.

Room 20 has an approximate total volume of 45,037 ft^3. Therefore, application of the Osborn emergency condition (i.e., development of a sudden leak) would apparently require a ventilation airflow of 15,012 cfm. However, jet-fuel vapor is heavier than air and has a relatively low diffusion coefficient. This would result in a vapor layer concentrated near the room floor. Therefore, the total room volume is not appropriate. This is clearly an example of the second error possibility described above.

To prevent concentrations in the floor-hugging vapor layer from approaching the LEL, the number of total room-air changes would have to be substantially increased over that for hydrogen. For example, if the jet-fuel vapor layer were to be concentrated in the lower 15% of the room height, the number of total room-air changes required to prevent the LEL being reached near the floor would be 133 per hour for a ventilation airflow of 100,080 cfm. For normal operation, the requirements would be 33.3 room changes per hour, or 25,021 cfm.

Alternatively, a classical analysis may be conducted to ascertain the likely ventilation requirements, for example, for a 50% fuel leak occurring upstream of the turbo-cooler or catalytic reactor when the combustor rig is operating at a pressure of 10 atm.

At atmospheric pressure the enthalpy-temperature diagram for nominal JP-5 (for which JP-8 is taken as equivalent) indicates[3] that only liquid-phase fuel exists for fuel temperatures below 390°F. The fuel temperature will be below this value prior to reaching the turbo-cooler/reactor heat exchanger. Therefore, a leak will produce a stream of liquid fuel. If the leak were equal to 50% of the maximum rig flow rate of 12 gpm, the fuel liberated into the facility would be 40.5403 lbm/min.

For the combustor to operate at 10 atm, the pressure in the fuel line must be on the order of 12 atm, assuming that the fuel pump can maintain this pressure in the presence of such a significant leak. The initial velocity of the fuel jet leaving the leak hole is given by

$$U_{init} = C_d \, (2 \, \Delta P_f / \rho_f)^{1/2}$$

where the discharge coefficient may be taken as 0.61 for a sharp-edged hole. Under the conditions described above and assuming that the fuel cools to 200°F upon expansion, the stream initial velocity is 107.72 ft/s. This velocity is more than sufficient to result in atomization of the leak fuel stream. It is difficult to estimate the atomization achieved from the leak hole. Using formulae of Simmonds,[4] a value of ~ 184 μm can be estimated. Since actual values are likely to be higher, this is a conservative number for droplet evaporation.

The evaporation time for a polydisperse spray of droplets is given by[5]

$$\tau_{evap} = (C_3)^3 \rho_f c_{p,g} (D_{32})^2 / [8C_t k_g \ln (1+B)]$$

where constants C_t and C_3 are equal to 0.46 and 0.31, respectively, and D_{32} is the spray Sauter Mean Diameter (SMD). The Transfer Number B for jet fuel may be taken as 3.7.[6] A range of SMD's can be assumed to produce Figure 2, which provides the evaporation times. The figure shows that evaporation times from 1.0 to 4.5 sec are probably necessary for 100% evaporation of the leak.

A simple droplet equation of motion can be written as

$$du_{d,i} / dt = F_i (u_{g,i} - u_{d,i})$$

where

$$F_i = 3/8\ C_D (\rho_g / \rho_d r_d) | (u_{g,i} - u_{d,i}) |$$

and subscripts d and g denote droplet and gas, respectively, i denotes initial values, and r_d denotes the droplet radius. At atomization, or extremely close thereto, the droplet initial velocities will range from the fuel-jet initial velocity of 107.7 ft/s for 200-μm droplets down to the ambient-air velocity (near zero) for 10-μm droplets.[7] The drag coefficients for small droplets can be very high--ranging from 0.5 to 30, depending on the droplet Reynolds number--with the higher values applying to the smaller droplets. Therefore, 10-μm droplets in the spray are subject to initial decelerations due to air drag on the order of 35,000 g's, while 200-μm droplets experience initial decelerations around 330 g's. These large droplet decelerations result in limited spray penetrations in times appropriate to the evaporation times. Thus, if the spray does not encounter a solid obstacle within ~ 5 ft of its origin, complete evaporation of the leaked fuel will take place.

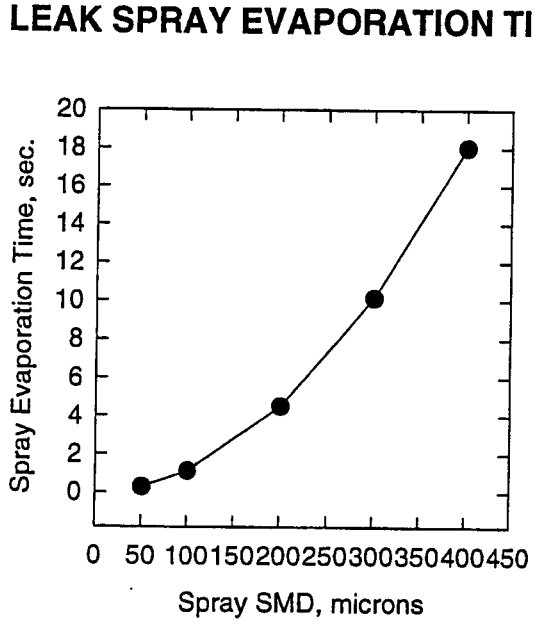

Figure 2. Effect of Leak Atomization on Evaporation Time.

Since the leaked fuel in the spray is likely to evaporate completely, the potential volume of fuel vapor produced is 102.8 ft^3/min, under the assumption that during the evaporation process the fuel vapor is cooled to 120 °F. For a uniform distribution throughout Room 20 in quiescent air, the volume of fuel vapor required to reach the LEL concentration of 0.6 % is 270.2 $ft.^3$ Hence, the time needed to reach this critical uniform concentration is the required volume divided by the volumetric rate of vapor production--2.63 min in this instance. Hence, the room-ventilation rate required to avoid reaching the critical concentration is the room volume divided by the time needed to reach the critical value of leaked fuel vapor, 17,124.3 cfm or greater.

However, the fuel vapor produced from the leak will **not** be uniformly distributed throughout the room. As described above, because of its high molecular weight, the fuel vapor will become concentrated near the room floor. A wide variety of parameters affect the dispersion of the leaked fuel vapor in this case:

1) Local convective air velocities in the facility generated by buoyancy effects from the hot combustor rig and exhaust ducting
2) Height of the leak above floor level
3) Momentum of the initial fluid leaked
4) Presence of solid obstructions in the test cell
5) Existence of any natural or forced cell ventilation
6) Density ratio of vapor to air

Modeling of fuel-vapor dispersion can be addressed through the Pasquill-Gifford plume and puff model[8] that employs dispersion coefficients that empirically specify the rates of spread of the dispersing vapor; alternatively, CFD approaches that employ appropriate physical modeling might be used.

Since modeling of vapor dispersion is usually quite difficult for enclosed or partially enclosed buildings, a pragmatic approach is frequently used to account for dispersion effects in a global fashion. This is effectively a safety-factor approach that is applied to the uniform-dispersion calculation. Such a safety factor of 4 or 5 might be applied to the uniform-dispersion ventilation rate. This approach would increase the required ventilation rate for Room 20 to 68,497–85,622 cfm, i.e., 91.25–114.07 room air changes per hour. The higher figures are consistent with the scaled Osborn Engineering Company emergency design for Room 22 given above.

For a leak downstream of the turbo-cooler/reactor heat exchanger, the fuel temperature would be ~ 400°F during rig start-up and ~ 1,000°F under maximum operating conditions. Under the start-up condition, the fuel-enthalpy chart indicates that 15% of the leak is flash-vaporized and that under the maximum condition 100%, is flash-vaporized. Compared to the upstream-leak case, therefore, atomization and evaporation are clearly not issues with this leak. However, compared to the upstream leak, the fuel-vapor temperature now becomes a serious issue. Clearly, the more hazardous case is that for such a leak under maximum operation.

For a leak from downstream of the turbo/cooler catalytic reactor, the 100% flash evaporation at 1,000 °F of the total fuel leak results in a vapor temperature of ~ 800°F and a

vapor density of 0.1815 lbm/ft^3. The volume of fuel vapor produced from the leak is 223.3 ft^3/min. at atmospheric pressure. The LEL for the fuel vapor is calculated by Zabetakis' formula

$$LEL_{Tvap} = [LEL_{25} / (1300 - 25)] (T_{vap} - 25)$$

[where LEL_{25} is the lower explosion limit for vapor at 25°C and T_{vap} is the vapor temperature (in °C)] to be 0.411% by volume. The volume of fuel vapor necessary to reach the LEL with complete dispersion through the room is 185.033 ft^3, and the time required to reach this quantity is 0.829 min. The room ventilation required to (just) prevent the LEL from being reached is, therefore, 54,355.9 cfm. With safety factors of 4 and 5 to allow for non-dispersion and concentration of the vapor, the ventilation requirements are 217,423.8 - 271,779.7 cfm, or 289.7 - 362.1 room changes per hour.

These values assume no further cooling of the vapor cloud as it mixes with the ambient air. When the fuel vapor is fully mixed with ambient air to the LEL concentration, the mixture temperature is ~ 87°F. If the ventilation air could mix instantaneously with the vapor to achieve this temperature, the ventilation requirements would revert essentially to the values calculated for the upstream leak case. Therefore, an intermediate level of ventilation might be sufficient, i.e., 141,176.4 cfm or 188.1 room changes per hour for the safety factor of 4 and 176470.5 cfm or 235.1 room changes per hour for the safety factor of 5.

Table I contains a comparison summary of room-air ventilation rates required to prevent a fuel-vapor explosion, as calculated by different approaches. The Scaled Osborn and Classical Analysis approaches have been described in detail above. NFPA Approach 3 is based on the National Fire Protection Association (NFPA) general requirements for continuous process ovens in which solvents are being evaporated; Approach 3 is founded in the NFPA requirement that *"in a continuous process the rate of safety ventilation shall not be less than 10,000 ft^3 of air, referenced to 70 °F, per gallon of solvent evaporated."* In this instance it was applied to a leak of supercritical fuel from downstream of the catalytic-reactor heat exchanger. An appropriate temperature correction was applied for the elevated temperatures associated with the supercritical fuel. An independent calculation was also carried out by SAFETY (Andrew M. Petty), but it appeared to have a units problem. Therefore, a corrected calculation using the same approach was made and is listed under Corrected Petty.

Table I. Summary of Ventilation Requirements for Preventing a Vapor Explosion

Approach	Air-Ventilation Rate	
	CFM	Rm. Change/hr
Scaled Osborn	**100,080**	**133**
Classical Analysis	**85,622**	**114**
NFPA Approach 3	**104,400**	**139**
Corrected Petty	**81,463**	**109**

It can be seen from the table that the approaches used and their different assumptions result in broadly similar findings, with the requirement being for between 115 and 140 room changes of air per hour. This represents a significant air-plant requirement and high installation and operating costs. A further concern is that fuel vapor is heavier than air, which is significant since the compressor room is located below Room 20 and is open to it via exhauster ducting, etc. Although much larger in volume than Room 20 and, thereby, offering further favorable dilution of any fuel-vapor ingress, the compressor room might also require ventilation. This aspect has not been considered here.

No information is available in the literature concerning plume fires of supercritical jet-fuel leaks; therefore, the problem was explored preliminarily via an experimental approach. The experimental study involved representation of two types of leaks that form a plume. The first leak simulation was by means of a pressure-atomizing fuel nozzle that produces a well-atomized, conical spray of liquid fuel which can be adequately characterized. This represented a fairly substantial leak but not near the worst-case scenario for vapor production considered above. However, the good atomization offered by the fuel injector does represent a worst-case scenario in terms of presentation of fuel for mixing with air that results in droplet evaporation and subsequent combustion of the vapor produced. The second leak simulation was to be of a pinhole leak. For this purpose fuel was discharged as a plain jet through a fine capillary tube.

A simple experimental arrangement was constructed that relied on the existing AFRL PHOENIX hot fuel rig to deliver JP-8 fuel at supercritical temperatures and pressures to a simulated leak. Hot pressurized fuel was delivered to a length of fuel line; immersing this line section in a flow of hot nitrogen gas minimized heat losses. The leak simulation was contained in the end of the length of fuel line. Two types of leak simulation were attempted from this line--a relatively large hole and a pinhole. The large leak was represented by a small pressure-swirl Simplex atomizer having a flow number, FN, of 0.3 $(lbm/hr)/(psi)^{1/2}$. With a flow of conventional (liquid) fuel, this atomizer at 770 psig would result in a flow of 79 ml/min with a liquid spray having a SMD of ~ 33 μm. The fuel mass flow rate from this injector is equivalent to about 1.3 US gal/hr. (Note that, as stated, this is far below the fuel-spillage rates for the vapor-explosion studies described above.) The smaller leak was represented by a 0.005-in.-internal-diameter ceramic capillary tube. Because of manufacturing difficulties encountered with blockage-free cutting of this small-size tube, the internal diameter was increased to 0.009 in. Unfortunately, the mass flow rates obtained with this increased-diameter tube were too great to be considered representative of the pinhole leak. The length of the capillary tube was 0.625 in. The discharges from the simulated leaks were collected in a 3.5 x 3.5 in. section quartz spray chamber that led to the rig fuel-collection tank and removal ducting to external ventilation. The spray chamber was ventilated with ambient air; the air velocity and mass flow rate were unknown initially. The rig is illustrated in Figure 3. For the initial tests the fuel bulk temperature was 1,000°F near the simulated leak, and the metal temperature was measured to be 730°F.

It was of interest to examine the spray pattern from the pressure atomizer as the fuel temperature was increased. For Tests 1 and 2, the fuel pressure drop across the atomizer was maintained at a constant 770 psig. For Test 1 the bulk-fuel temperature at a station 7.25 in. upstream of the atomizer reached a peak just over 1,000°F, while for Test 2 the bulk-

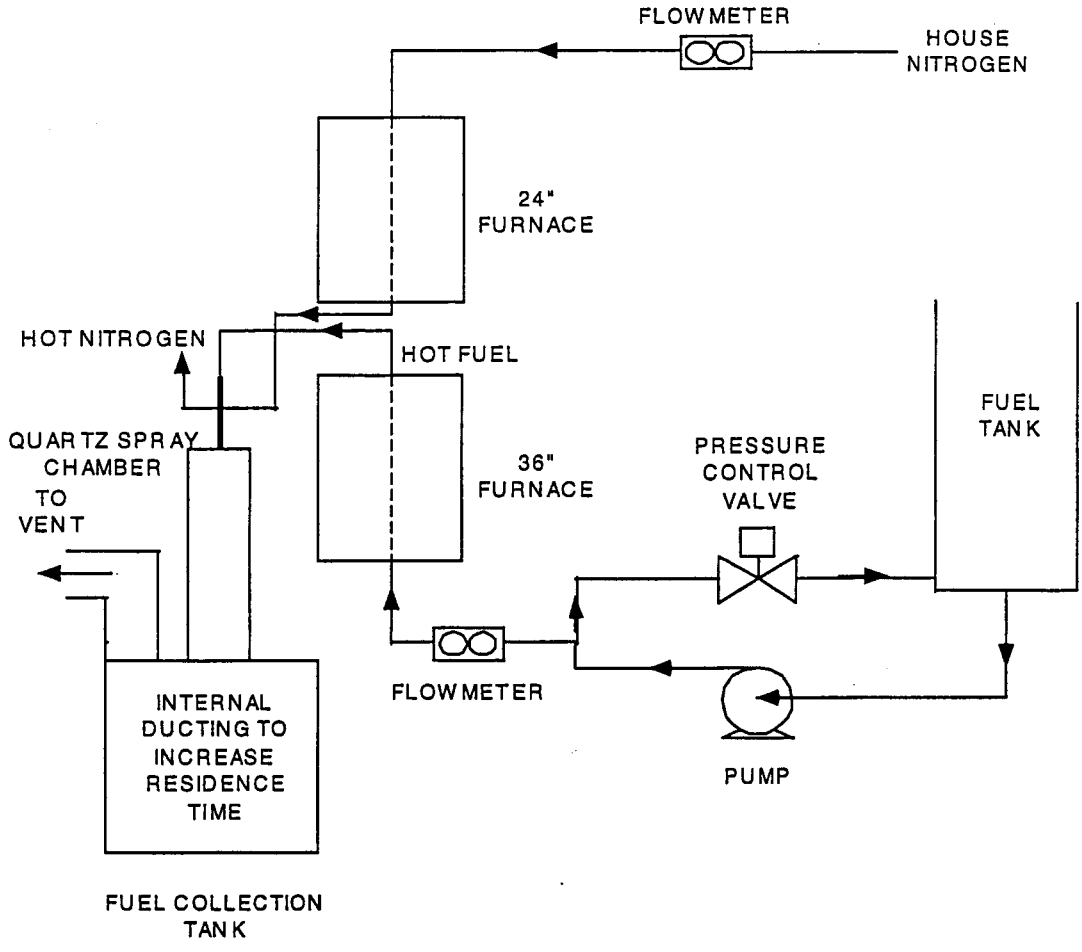

Figure 3. Schematic Diagram of the Phoenix Rig.

fuel temperature peak at the same location was just over 1200°F. These conditions are above the critical point for JP-8 fuel and were reached for Test 1 after 25 min and maintained 49 min into the test. The wall temperature of the atomizer **just** reached the critical level after 39 min, and fell below it 43 min into the test. Together, these liquid and metal temperature measurements suggest that fuel leaving the atomizer was under critical conditions after ~ 30 min and probably fell below critical conditions after ~ 45 min from the test start. Figure 4 shows the temperature-time histories for Test 1 as well as the fuel flow rate as a function of time.

Low-quality scanned images of photographs of the fuel spray at five time intervals during the test are given in Figure 5. Although the quartz spray chamber is too small, causing collection of recirculated fuel droplets on its interior surface, the photographs reveal the existence of a defined spray plume of liquid-fuel droplets up to 23 min into the test. After 31 min, no visible plume exists. A visible plume appears again after 45 min as the fuel temperature falls below critical. This series of photographs clearly indicates the flash vaporization of fuel occurring under critical conditions.

Figure 4 shows that the liquid mass flow rate reaches a minimum 31 min into the test and then recovers as the fuel temperature is reduced again. The mass flow rate of fuel under

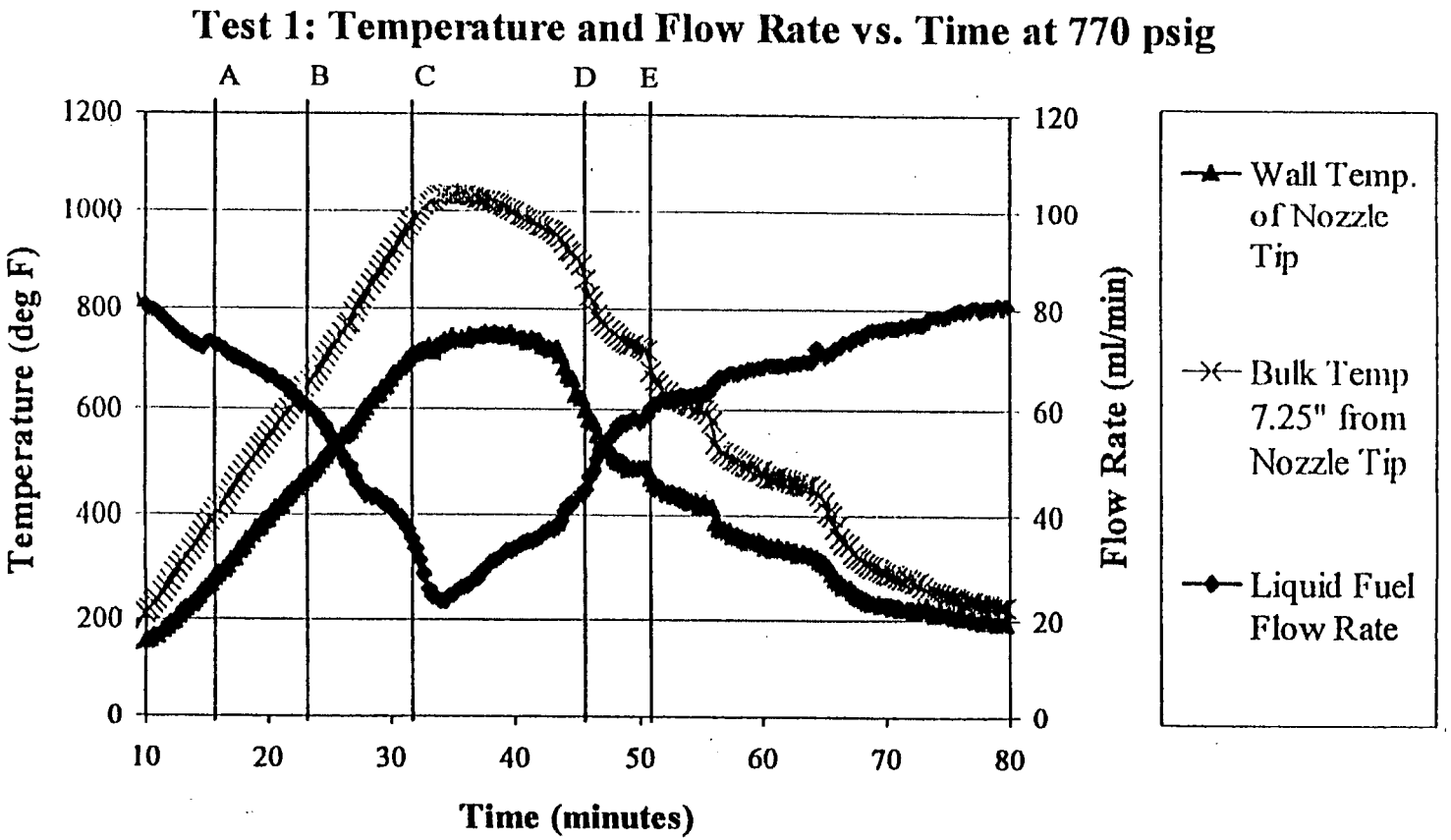

Figure 4. Test-1 Recorded Data.

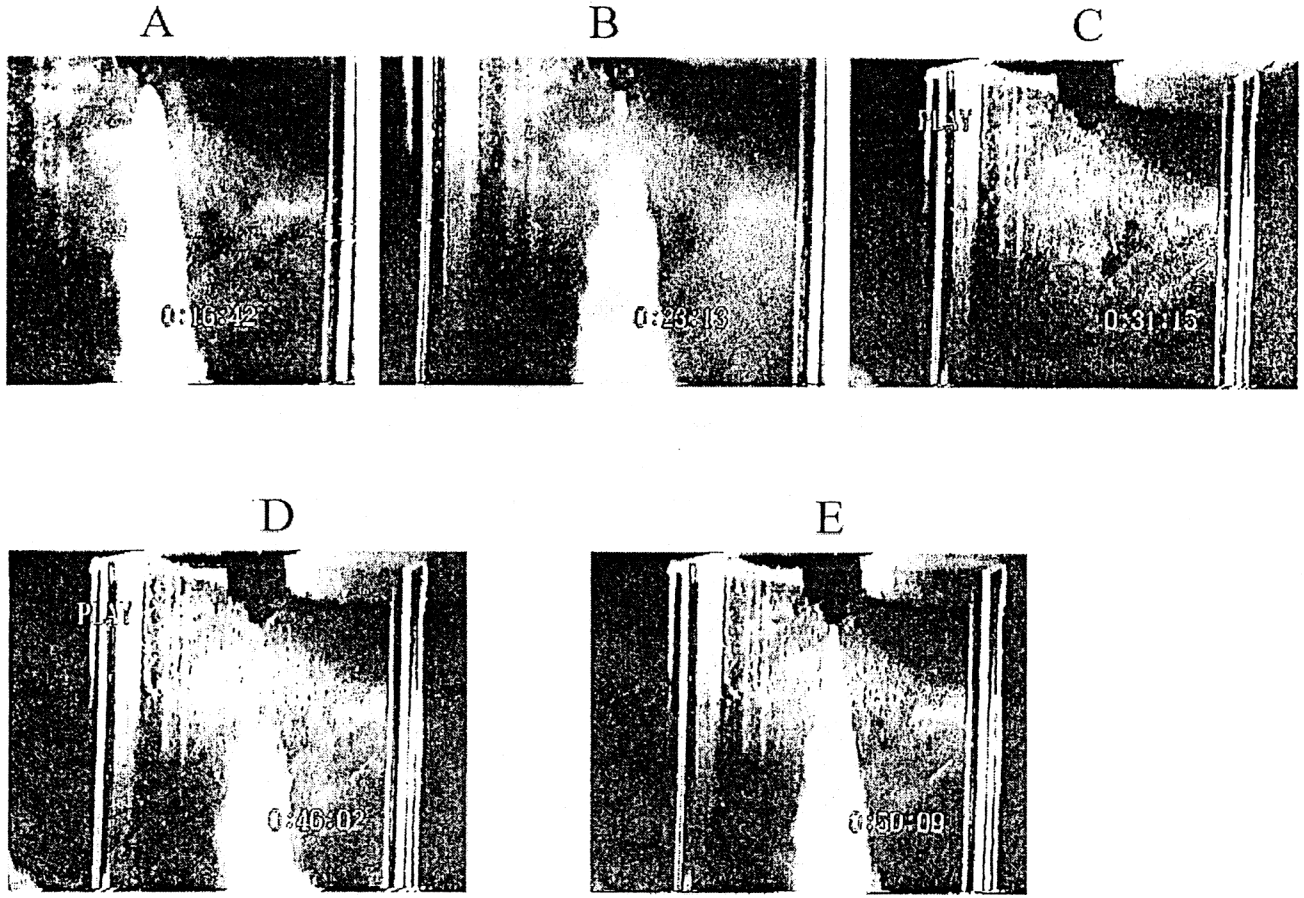

Figure 5. Test-1 Spray Photographs at Various Time Intervals.

normal fuel operating temperatures, at the beginning and end of the test, is 80 ml/min. This value is very near the value (79 ml/min) calculated from the atomizer flow number with the 770-psi fuel pressure drop of the test. The density of a fuel at fixed pressure is known to decrease dramatically as the fuel temperature is increased toward its critical value; therefore, the measured mass-flow-rate behavior is entirely expected.

For Test 2 the fuel pressure at the atomizer was held at 770 psig, and the maximum fuel bulk temperature at 7.25 in. upstream was increased to 1,200°F, a condition that was reached ~ 45 min into the test. The atomizer-tip temperature reached a maximum value of ~ 760°F about 43 min into the test. Critical temperature for the fuel was surpassed after ~ 22 min. The temperature histories for this test are shown in Figure 6. As observed in Test 1, the liquid-fuel mass flow rate decreased as the fuel temperature was increased.

The spray photographs for Test 2 (not reproduced here) indicated the presence of a liquid spray up to at least 20 min into the test. However, the visible spray at 20 min appeared to form a little distance downstream from the atomizer tip and was initially asymmetric; noticeable intermittence was present in the spray at its apparent origin. The temperature history for the second test (Figure 6) suggests that at the 20-min time, the fuel could have been **just** at its critical temperature leaving the atomizer tip and, therefore, was present as a vapor. Subsequent cooling due to expansion and entrainment of lower temperature ambient gas could have made the fuel vapor subcritical again. This would result in liquid-fuel condensation in the plume, producing a visible spray originating at a slightly downstream position. At 30 min into the test, no visible spray was recorded by the camera, indicating true critical conditions in the plume.

For Test 2 a thermocouple was placed in the downstream plume region to provide a general indication of the approximate temperatures in the plume. The temperatures recorded are shown in Figure 6. The maximum temperature in the "spray" was ~ 450°F, and this was attained after ~ 35 min while fuel in the plume was in the non-liquid phase. The "spray" temperature after 20 min (see above) was about 300°F. The spontaneous-ignition temperature for JP-5 (to which JP-8 may be considered equivalent) is 470°F.[1] Therefore, it is not surprising that no ignition incidents were observed in the spray chamber.

In Test 3 the same procedure was followed as that for Tests 1 and 2, except that the capillary tube replaced the pressure atomizer. The fuel pressure at the tube was maintained at 430 psig. The fuel bulk temperature was measured 8.5 in. upstream from the tube tip (rather than the previous 7.25 in. for the pressure atomizer). The fuel peak bulk temperature was just under 900°F and was achieved ~ 27 min into the test. Figure 7 shows the recorded temperature and fuel-flow-rate histories with time.

The fuel pressure for this test was considerably below the critical value for JP-8, while the fuel bulk temperature at its peak was above the critical level. The wall peak temperature for the capillary tube of just above 500°F was reached after 25 min of testing. Images of the spray photographs show a defined spray of droplets up to 20 min into the test; at 24:34 min, no spray was visible. Both atomization and spray angle increased with fuel temperature. This behavior was to be expected for a plain jet atomizer at a fixed pressure drop. The "spray" temperature, measured ~ 1 in. downstream from the capillary tip, exhibited complex behavior, as Figure 7 reveals. A particularly large decrease in

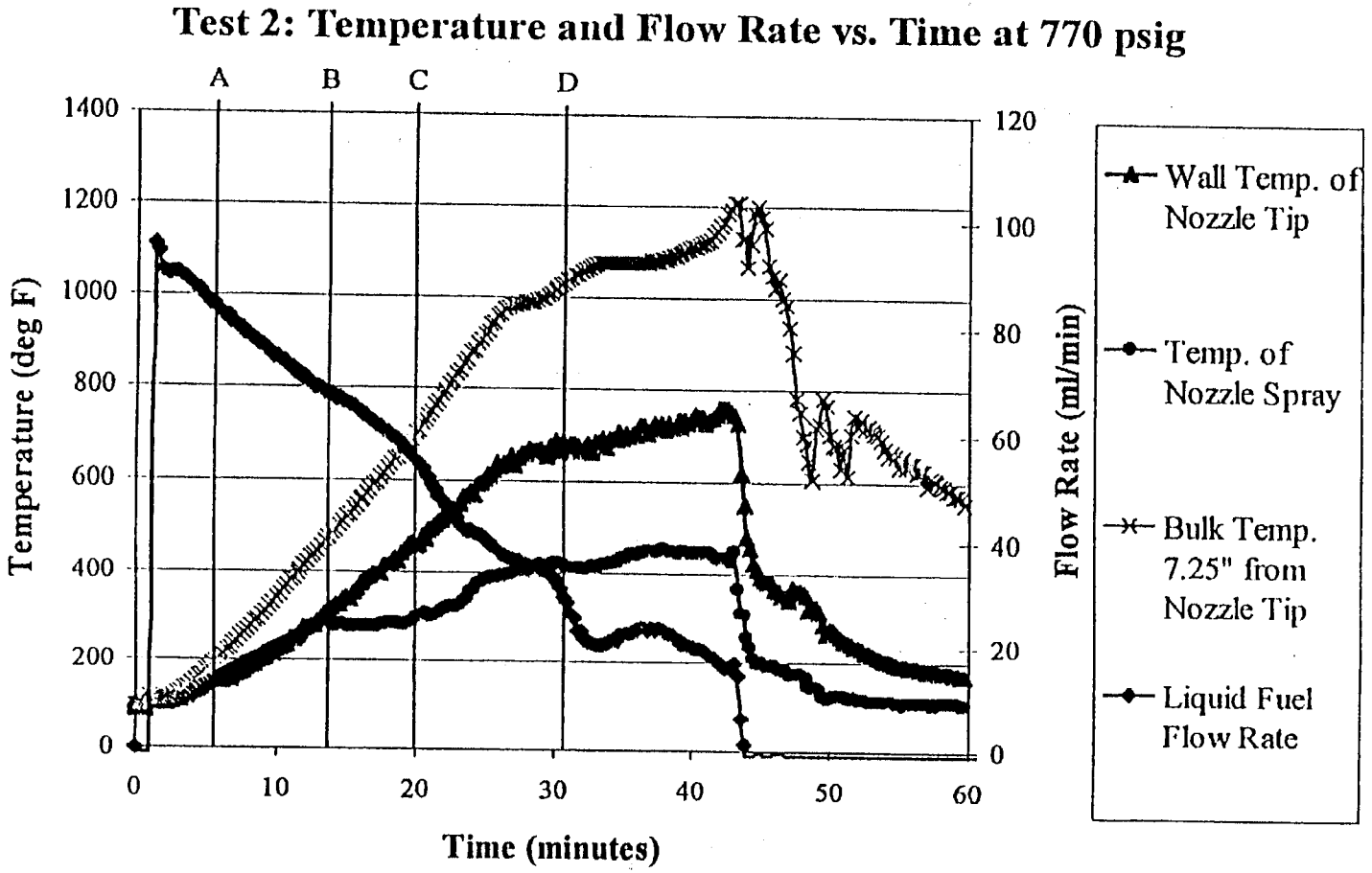

Figure 6. Test-2 Recorded Data.

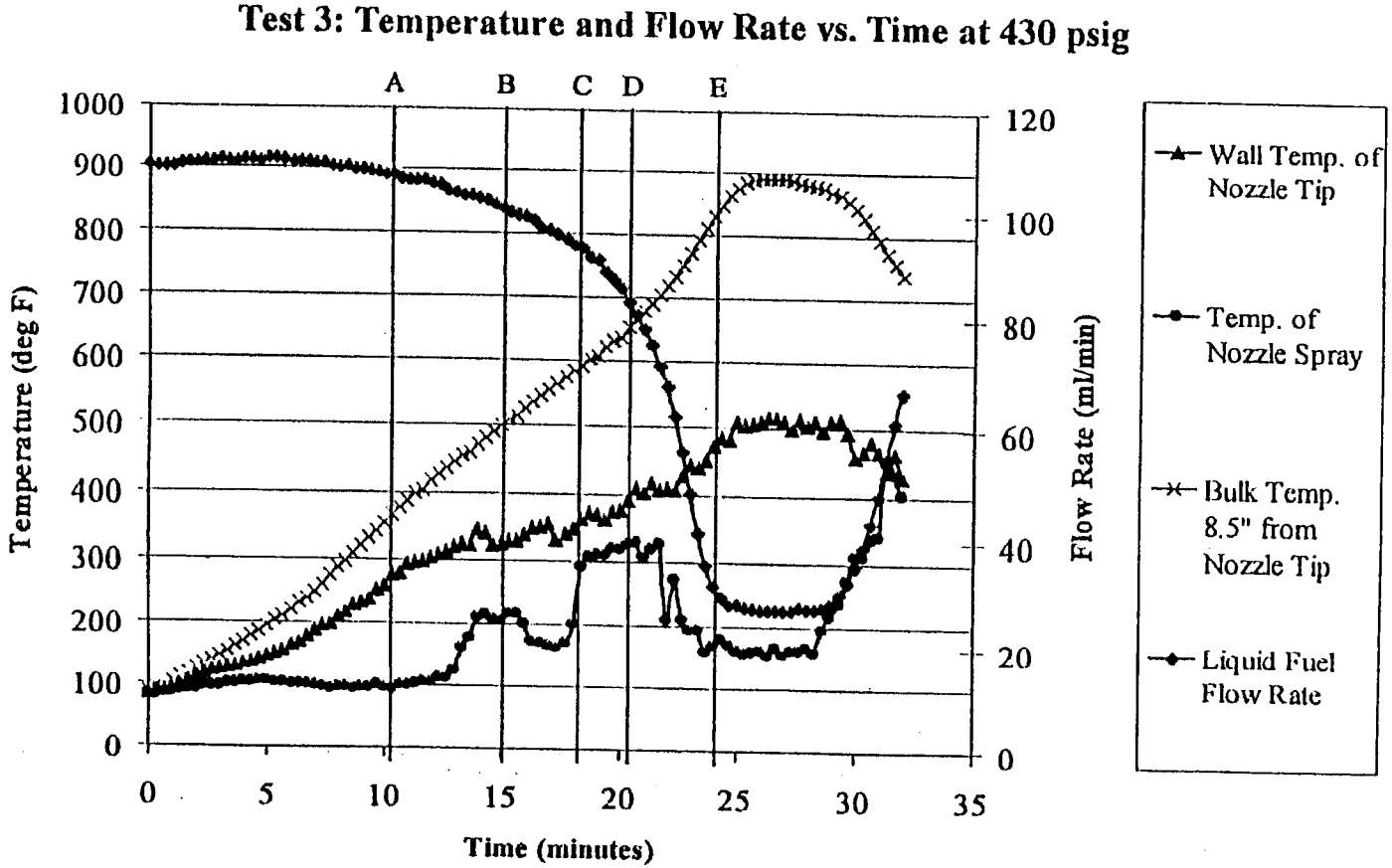

Figure 7. Test-3 Recorded Data.

spray temperature after 330°F occurred between 22 and 30 min. This can be associated with evaporation cooling since most of the fuel boils (the initial boiling point for JP-8 is ~ 420°F); the subsequent temperature increase can be associated with the vapor phase alone. The peak spray temperature of 440°F was reached 32 min into the test and occurred as the fuel bulk temperature was being reduced. This value is below the ignition temperature for JP-8, and no ignition was observed in the spray chamber.

The flow rate of fuel at normal liquid-fuel temperatures is much higher than that for the pressure atomizer at the same fuel pressure drop. The volumetric fuel-flow-rate behavior for the three tests is compared in Figure 8. Data from the two tests, with the pressure atomizer at a common pressure drop of 790 psig but with different fuel maximum bulk temperatures, form a common curve when plotted as a function of fuel bulk temperature. The flow rate decreases with increasing temperature in approximately linear fashion. Since the volumetric flow rate may be expressed as

$$V = \rho_f FN \sqrt{\Delta P_f}$$

where ΔP_f is fixed while FN is established by the atomizer internal (spin-chamber) geometry for which Reynolds-Number effects are small for low-viscosity fuels, the inverse direct proportionality of flow rate with fuel temperature is as expected. With the capillary tube acting as a plain jet atomizer, at a fixed fuel pressure drop, the volumetric flow rate decreases with increasing temperature in a non-linear fashion. The discharge coefficient for the fixed-geometry capillary tube depends strongly on the Reynolds Number in the tube, which itself depends on fuel temperature and, thus, is not fixed. Non-linear flow relationships with fuel temperature are, therefore, to be expected for the capillary tube. However, the effects of compressibility complicate the relationships for both types of injectors. Liquid fuel is incompressible, while fuel vapor is compressible.

For the 790-psig tests, the effects of compressibility would be expected to become significant at some time after the fuel (already above its critical pressure) reaches its critical temperature and no longer behaves as a liquid. Careful consideration of Figure 8 suggests that the combined data for Tests 1 and 2 can actually be represented by **two** straight lines--one between fuel bulk temperatures of 100 and 670°F and the other of slightly increased slope between 800 and 1200°F. The break point between these two lines at 770°F is in satisfactory agreement with the critical-temperature value. This implies that one line is appropriate for the liquid phase, and the other is appropriate for the vapor phase. Since the vapor phase for supercritical fuel is of high density, it is less susceptible to the effects of compressibility. For the capillary tube, the volumetric flow rate with compressibility depends on functions of fuel density, Reynolds Number (via discharge coefficient), and the compressibility factor. The compressibility factor, which is always less than unity, includes the ratio of specific heats for the fuel vapor and the pressure ratio across the capillary. The dependencies on Reynolds Number and compressibility factor are non-linear. In this case, simple boiling of the fuel produces the vapor phase; and the vapor, therefore, is less dense and more susceptible to compressibility.

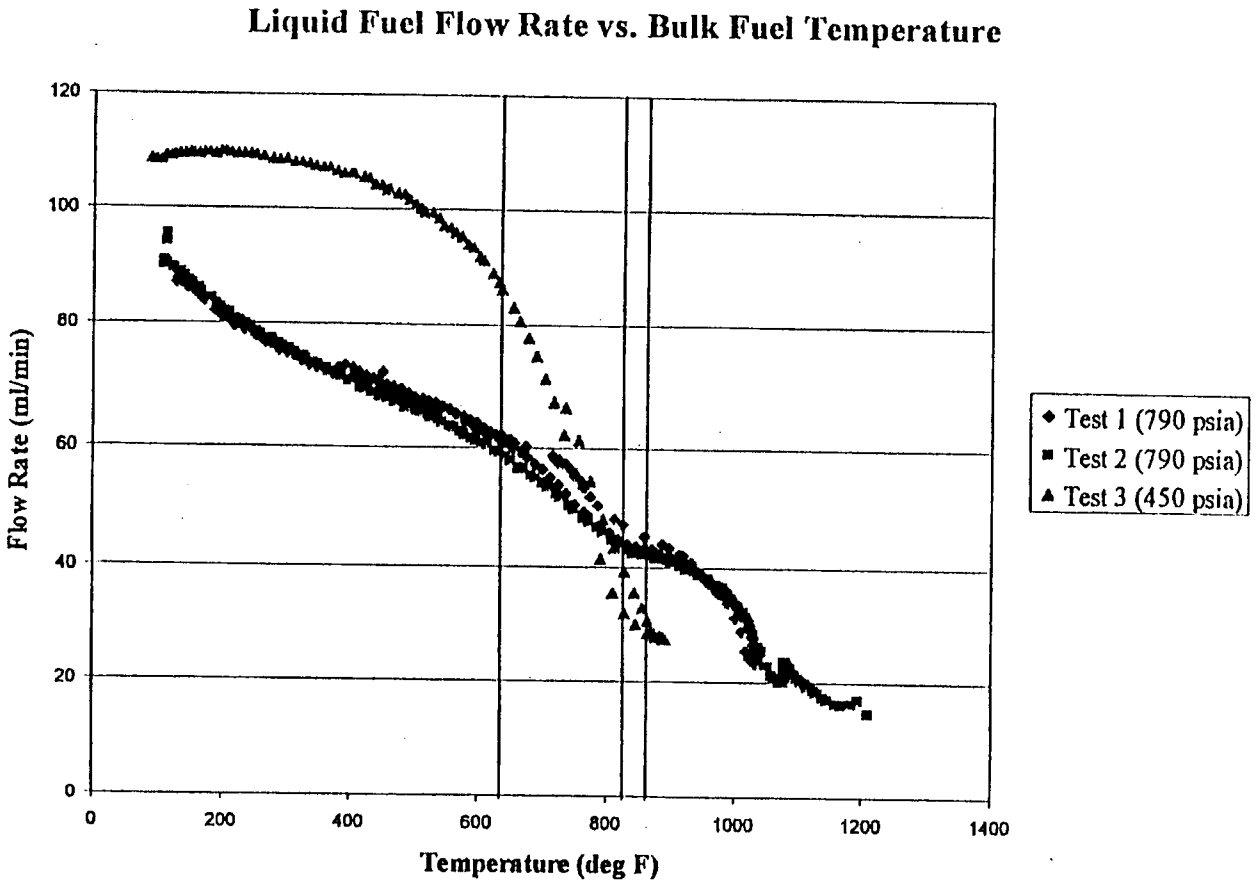

Figure 8. Volumetric-Flow-Rate Data for All Tests.

Also of relevance to the plume fire risk is the spray angle of atomized fuel formed by the leak. For a swirl pressure atomizer, the spray angle is largely determined by the spin-chamber geometry. For liquid fuels as the temperature is increased, internal friction is reduced and the tangential velocity in the atomizer spin chamber is increased; this tends to improve atomization and to widen the spray angle. The observed spray angle is determined by the outer sheath of fine droplets (the "overspray") surrounding the greatest radial concentration of larger droplets. Aerodynamic-drag forces quickly reduce to zero the relative velocity between the finest droplets in the overspray and the surrounding air entrained into the spray by its forward momentum. These fine droplets are, therefore, carried **into** the spray interior by the entrained air; hence, the **spray angle is reduced**. Therefore, it should be expected that the atomizer spray cone angle in Tests 1 and 2 will be reduced slightly in angle as the fuel bulk temperature in the liquid phase is increased. Such behavior was observed.

For a plain jet atomizer such as the capillary tube, no direct mechanism similar to a spin chamber exists for developing a spray angle. The formation of a spray angle depends entirely on wave motion developed in the liquid jet leaving the capillary tube. The wave motion is determined by the flow characteristics within the capillary and the relative velocity of the fuel exiting the capillary to the ambient air. Fuel temperature changes will alter both the interior Reynolds number and the relative velocity and, hence, the spray angle. With the volumetric-flow-rate characteristic for Test 3 given in Figure 7, the essentially constant flow rate for approximately the first 15 min of the test while fuel temperature was increasing would result in a spray angle that increased over this time period. Thereafter, the spray angle would tend to be reduced as a result of decreasing flow rate and spray entrainment effects. Such behavior was observed.

The plume tests, with the fuel under supercritical conditions and at temperatures sufficiently high to result in complete subcritical boiling of the fuel, revealed interesting behavior and valuable preliminary information. These tests produced no instances of plume fires and were conducted with the "spray" at temperatures below the spontaneous ignition temperature for the fuel. Here, as in investigations of engine-compartment fires due to loss of engine integrity, it is extremely difficult to calculate or demonstrate the direct existence of plume fires. Conditions of local equivalence ratio in the spray, spray temperatures, and plume velocities are generally not conducive to the initiation and establishment of sustained plume fires. However, engine-compartment fires from plumes of this type do occur. For such fires it is usually necessary for the plume to impinge on a secondary surface that results in a different flow field and provides a hot ignition source. Minimum surface temperatures necessary to provide an ignition source vary with hydrocarbon type and surface geometry but are typically in the range 900 - 1,000°F for stoichiometric mixtures, with significant ignition delays that depend on the mixture initial temperature.

"Plume-type" fires are best addressed through flame-detection and fire-extinguishing systems rather than room-ventilation systems.

Summary

For "plume-type" fires involving high-pressure leaks of supercritical JP-8 fuel or leaks of high-temperature vaporized JP-8 fuel (such as those occurring downstream of a turbo-cooler/catalytic reactor), the current fire-extinguishing system in Room 20 should be adequate. It would be advantageous to install additional flame detectors on the rig itself, especially in the neighborhood of the turbo-cooler/catalytic reactor heat exchanger.

For elimination of the explosion risk due to fuel vapor from a large, continuous liquid-fuel leak, the current ventilation system used for Room 20 is inadequate. Provision of a suitable emergency ventilation system involving between 115 and 140 whole room changes of air per hour probably would be prohibitively expensive. Ventilation of the downstairs compressor room should also be considered, but this would add considerably to the overall system cost. The safety features of the Room-20 control system, which involve provision of vapor detectors and an automatic fuel-system total shut-down before a maximum of 5 gal of fuel has leaked, make a positive contribution. Another positive feature is the facility design that excludes all possible ignition sources in the layer up to 24 in. from the floor.

TASK 2: CONSTRUCTION OF ADVANCED-TURBINE-ENGINE FUEL SYSTEM

Considerable construction work related to the necessary plumbing for the advanced fuel system was accomplished in the Room-20 high-pressure combustion facility in preparation for the planned test program.

TASK 4: COMBUSTION STUDIES WITH COAL-DERIVED FUELS

Introduction

To support the study of combustion of coal-derived fuels, initial tests at atmospheric pressure would offer many advantages, including low cost, ease of change, and largely unfettered optical access. For this purpose it would be necessary to design a new combustion rig for Room 151. The design would be based on the trapped-vortex-combustor concept but would be free from the proprietary restrictions associated with the current rigs. This design would then serve as the prototype for a combustor rig for subsequent high-pressure testing in the Room 20 test cell. For the new combustors, therefore, open publication of the results of testing with coal-derived fuels would be allowed.

Design Studies

The technical goals of the new trapped-vortex-combustor design were to 1) investigate the effects on the vortex structure of mass extraction from the main vortex cavities by struts connected to mainstream bluff-body flameholders, and 2) explore the interactions with the mainstream of the reacting wakes from the struts and flameholders. The intent was to establish the maximum mainstream Mach Number for which an acceptable overall

combustion efficiency could be maintained. Use of single and double cavities was to be explored. In addition, the flameholder blockage level was to be extended to duct-burner levels.

The decision was made that the combustor-rig arrangement would be planar and the form of the mainstream flameholders would be a vee gutter. The vee-gutter form was also adopted for the struts; the arrangement of flameholders and struts was orthogonal.

Many design restraints were imposed. Within the facility air and fuel-flow limits, the goal was to achieve as high an approach Mach Number as possible in a reasonable duct height without producing local shock formation in the mainstream flameholder. For the flameholder, the goal was to achieve adequate geometric blockage with a reasonable vee-gutter base dimension. Several forms of distribution of the total blockage were investigated, including uniform and non-uniform. Non-uniform distributions represented two and three passage feeds to the flameholder in an engine situation. For the lower levels of blockage, an additional constraint was imposed--that the blockage not be so disperse that reacting wakes would not always be able to communicate within a reasonable distance downstream of the flameholder. Limitations on the preheated air temperature and operating equivalence ratio were established such that the maximum adiabatic flame temperature would always be less than the annealing temperature of the proposed quartz windows.

With a minimum duct height of 4 in., the air supply limited the maximum duct aspect ratio to 2.0 and the approach velocities at 500°F to only 100 ft/sec. At this preheat temperature, the uncooled quartz windows limited the mainstream equivalence ratio to a maximum of 0.5. Even if additional airflow could be provided, the facility exhauster and its duct would limit the mainstream velocity to a maximum of 165 ft/sec at an equivalence ratio of 0.5.

In the blockage configurations examined for this duct, the vee-gutter base dimensions were too small to allow sheet-metal fabrication. To cover the desired range of blockages, the gutters would have to be solid in cross section because of manufacturing costs. Distributed blockages below 20% could not be considered for manufacturing reasons. Whether uniformly distributed or center-concentrated, blockages greater than 60% should be used for simulation of the three-passage feed to the duct. For single-cavity studies, the total blockage should be cavity-centered in distribution.

Summary

To meet the design requirements of the new combustor rig, extensive and expensive modifications would be required to the Room 151 test facility. The cost of these modifications could not be justified. Relaxation of design requirements such as elimination of the high-speed duct-burner part of the study was not considered.

REFERENCES

1. H. C. Barnett and R. R. Hibbard (Eds.), "Borsic Considerations in the Combustion of Hydrocarbon Fuels with Air," NACA Report 1300, NACA, Lewis Flight Propulsion Laboratory, Cleveland, OH, 1959.

2. H. F. Coward and G. W. Jones, "Limits of Flammability of Gases and Vapors," Bulletin 503, U. S. Bureau of Mines, 1952.

3. P. W. Pillsbury, "Enthalpy-Temperature Diagram for Average JP-5 Fuel," Pratt & Whitney Curve No. 165384, 1962.

4. H. C. Simmons, "Empirical Formulae for Prediction of Spray Drop Sizes," Report No. EDR 6660084, Parker-Hannifin Corporation, November 1966.

5. D. R. Ballal and A. H. Lefebvre, "Flame Propagation in Heterogeneous Mixtures of Fuel Droplets, Fuel Vapor and Air," *Proceedings of the 18th Symposium (International) on Combustion*, The Combustion Institute, Pittsburgh, PA, 1981, pp. 321-328.

6. D. B. Spalding, *Some Fundamentals of Combustion*, Butterworths Scientific Publications, London, 1955.

7. G. J. Sturgess, K. R. McManus, and S. A. Syed, "Calculation of a Hollow-Core Liquid Spray in a Uniform Air Stream," *J. Propul. Power*, 1(5), 360-369 (November-December 1985).

8. D. G. Lilley, "Fuel Release and Ignition Calculations," AIAA Paper No. 98-0262, 36th Aerospace Sciences Meeting and Exhibit, Reno, NV, January 12-15, 1998.